The Dissertation Committee for Robert James Bondi Certifies that this is the approved version of the following dissertation:

First-Principles Atomistic Modeling for Property Prediction in Silicon-based Materials

Committee:

Gyeong S. Hwang, Supervisor

C. Buddie Mullins

John G. Ekerdt

James R. Chelikowsky

Sanjay K. Banerjee

First-Principles Atomistic Modeling for Property Prediction in Silicon-based Materials

by

Robert James Bondi, B.S.Ch.E.; M.S.E.E.

Dissertation

Presented to the Faculty of the Graduate School of

The University of Texas at Austin

in Partial Fulfillment

of the Requirements

for the Degree of

Doctor of Philosophy

The University of Texas at Austin

December 2010

Dedication

To the memory of my mother, Judith, and my father, James

Acknowledgements

I acknowledge Professor Gyeong S. Hwang for his advice on the theoretical aspects of materials modeling and during the publication processes. I also thank Professor C. Buddie Mullins for his long-time advice dating back to my undergraduate transport phenomena and reactor design classes and helping recruit me back to the Department of Chemical Engineering for a second academic term to work on the Ph.D. degree.

I acknowledge fellow graduate student, Sangheon Lee, for his willingness to share ideas and software utilities. In addition, Sangheon is also credited with generation of most structural models used in this work. Other Hwang group members are acknowledged for a mixture of technical and entertaining discussions.

Furthermore, I thank my parents, James and Judith, for both inspiration and encouragement. Finally, my wife, Susan, is especially appreciated for continuous support and enduring the extremely long and late hours I spent on campus, especially during the later stages of degree work.

First-Principles Atomistic Modeling for Property Prediction in Silicon-based Materials

Publication No._____

Robert James Bondi, Ph.D.

The University of Texas at Austin, 2010

Supervisor: Gyeong S. Hwang

The power of parallel supercomputing resources has progressed to the point where first-principles calculations involving systems up to 10^3 atoms are feasible, allowing *ab initio* exploration of increasingly complex systems such as amorphous networks, nanostructures, and large defect clusters. Expansion of our fundamental understanding of modified Si-based materials is paramount, as these materials will likely flourish in the foreseeable cost-driven future in diverse micro- and nanotechnologies. Here, density-functional theory calculations within the generalized gradient approximation are applied to refine configurations of Si-based materials generated from Metropolis Monte Carlo simulations and study their resultant structural properties. Particular emphasis is given to the contributions of strain and disorder on the mechanical, optical, and electronic properties of modified Si-based materials in which aspects of compositional variation, phase, strain scheme, morphology, native defect incorporation, and quantum confinement are considered. The simulation strategies discussed are easily extendable to other semiconductor systems.

Table of Contents

List of Tables

List of Figures

Chapter 1

Introduction

A simple benchmark of crystalline Si (*c*-Si) against other common semiconductors [1] in Table 1.1 indicates that Si is an average semiconductor, at best, in terms of the carrier mobilities that limit device operation frequency. In addition, the indirect nature of the Si band gap (E_g) precludes any first-order optical emission processes for photonic devices. However, the immense proliferation of Si-based devices since the 1950s [2] is not driven by performance, but by the following factors: (1) low-cost and abundance, (2) large and defect-free substrates, (3) process technology, and (4) amorphous SiO_2 (*a*-SiO_2). The ease of integration, reproducibility, and remarkably low defect densities (typically between 10^{10} and 10^{12} cm^{-2}) [3,4] of the *c*-Si/*a*-SiO_2 interface are arguably the primary reasons for the domination of Si-based electronics.

Table 1.1: Electrical comparison of common semiconductors [1].

	μ_n (cm^2/V-s)	μ_p (cm^2/V-s)	E_g (eV)
Si	1350	480	1.11
Ge	3900	1900	0.67
GaAs	8500	400	1.43
InSb	1×10^5	1700	0.18
InP	4000	100	1.35

Given the immense inertia driving implementation of Si-based devices, a thorough understanding of methods that might be applied to improve Si performance metrics is of great technological significance. An improved fundamental understanding of the relationship between structural properties and the characteristic mechanical,

electronic, and optical properties of Si-based materials is the motivation behind the present work. Basic factors of both cost and practicality should continue to drive creative applications of modified Si materials to compete with better semiconductors in virtually every device application space.

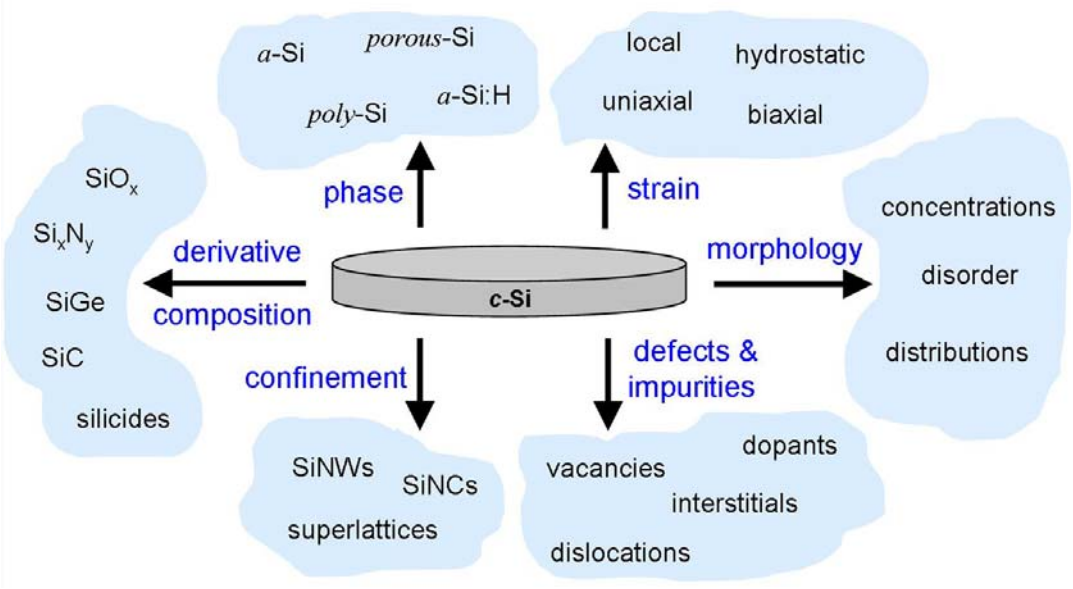

Figure 1.1: (Color available) Conceptual illustration of various techniques available to alter crystalline Si properties.

In the following chapters, all six categories of material manipulation represented by the clouds in Fig. 1.1 will be addressed. Key theoretical and computational concepts used throughout this work are developed in Chapter 2. In Chapters 3 and 4, the influence of various strain fields on the structure and stability of Si self-interstitial clusters (I_n) is expounded. Chapter 5 extends the same concepts to review the structure and stability of Si vacancy clusters (V_n) in strained environments. In Chapter 6, property predictions (mechanical and optical) are introduced for both amorphous hydrogenated Si (*a*-Si:H) and Si-rich silicon oxides (*a*-SiO_x, $0 \leq x \leq 2$). In Chapter 7, the role of structural disorder in optical absorption in Si is explored using the same V_n of Chapter 5 to incrementally introduce nanoscale disorder. A multiscale perspective is also applied to compare the

relative effects of disorder, density, and V_n concentration on optical absorption. Chapter 8 extends the findings of Chapter 7 by introducing applied strain to further distort local native defect structural properties to modulate Si absorption. Furthermore, Chapter 9 discusses the structural, electronic, and optical properties of Si nanowires (SiNWs) with realistic amorphous oxide surface passivation layers. Finally, Chapter 10 provides conclusions based on the presented simulation results.

Chapter 2

Theoretical and Computational Background

2.1 Quantum Mechanical Foundation

The most fundamental relationship in quantum mechanics is the Schrödinger equation. For most investigations involving the electronic structure of solids, the Born-Oppenheimer approximation applied to the time-independent form of the Schrödinger equation provides an adequate system description:

$$\hat{H}\Psi = E\Psi, \tag{2.1}$$

where $\hat{H}$ is the Hamiltonian, Ψ is the wavefunction, and E is the electronic energy [5]. The Born-Oppenheimer approximation is justified in non-relativistic calculations in which the much heavier and slower ions can be treated separately from much lighter and faster electrons. With the ionic contribution modeled as a stationary network of charged nuclei, the ionic structure calculations are often neglected and most computational effort falls to calculation of the ground-state electronic structure.

For an N-electron system, the Hamiltonian operator (in atomic units) is given by

$$\hat{H} = \sum_{i=1}^{N}\left(-\frac{1}{2}\nabla_i^2\right) + \sum_{i=1}^{N} v(\mathbf{r}_i) + \sum_{i<j}^{N}\frac{1}{r_{ij}}, \tag{2.2}$$

where the first, second, and third terms represent the kinetic energy operator, the external potential of electron-nucleus attraction, and the electron-electron repulsion term, respectively.

2.2 Density-Functional Theory

The formalism of density-functional theory (DFT) provides, in principle, an exact solution to the Schrödinger equation. A major step in the evolution of DFT occurred in 1964 when Hohenberg and Kohn [6] proved the validity of electron density distribution, $\rho(r)$, as a basic variable. Their theorem showed that determination of the ground-state $\rho(r)$ uniquely determines the ground-state wavefunction, Ψ, and effectively all other electronic properties. From this theorem, the electronic energy can be expressed (similar to the form of Eqn. 2.2) as

$$E[\rho(r)] = T[\rho(r)] + V_{ne}[\rho(r)] + V_{ee}[\rho(r)] , \qquad (2.3)$$

where $T[\rho(r)]$ is the kinetic energy of the interacting electron system, $V_{ne}[\rho(r)]$ is the potential energy of interaction between ionic nuclei and electrons, and $V_{ee}[\rho(r)]$ is the potential energy of electron-electron interaction. Ultimately, $V_{ee}[\rho(r)]$ is perhaps the most challenging term which consists of both a classical repulsion term and a non-classical contribution commonly known as the exchange-correlation energy [5]. In this form, minimization of $E[\rho(r)]$ with respect to $\rho(r)$ determines the ground-state energy of the system. Note that $E[\rho(r)]$ is a function of a function, which is the basis for the "functional" aspect of DFT.

While Eqn. 2.3 is exact, the primary limitation of the Hohenberg-Kohn theorem is that the analytical forms of $T[\rho(r)]$ and $V_{ee}[\rho]$ for the interacting electron system are generally unknown. As a result, DFT calculations have an inherent approximation embedded in the elusive exchange-correlation energy term, $E_{xc}[\rho(r)]$. The Hartree-Fock model comprehends electron exchange interaction, which accounts for interaction between electrons of parallel spin [7]. The exchange energy contribution ($E_x[\rho(r)]$) tends to lower the system energy by partially compensating for direct Coulomb interaction. The Pauli exclusion principle requires electrons occupying the same energy level to

possess opposite spins; this additional constraint based on electron spin is conceptualized as two electron density distributions [ρ^{α}(r) and ρ^{β}(r) for spin-up and spin-down] [5,8]. Electrons of parallel spin are farther apart, on average, than electrons of antiparallel spin as a result of the Pauli exclusion principle. Therefore, the energy of Coulomb interaction is smaller for electrons of parallel spin relative to those of antiparallel spin because the Coulomb interaction is a function of spatial separation [7]. The correlation contribution ($E_c[\rho(\mathrm{r})]$) in $E_{\mathrm{xc}}[\rho(\mathrm{r})]$ stems from the inaccuracy in the assumption that electrons are independent; in reality, the motions of electrons of parallel spin are correlated. The Hartree-Fock approximation is based on solution of many single electron equations [7]; in consequence, electron correlation is absent and the residual difference between the exact energy and the Hartree-Fock approximation is $E_c[\rho(\mathrm{r})]$ [5,8]. A significant amount of effort and progress has been made toward improved $E_c[\rho(\mathrm{r})]$ descriptions even though $E_c[\rho(\mathrm{r})]$ is typically an order of magnitude or more smaller than the exchange energy [5].

The next major development in modern DFT formalism was introduced by Kohn and Sham [9] in 1965. The significance of their work is the substitution of the intractable many-electron problem with a problem of N independent electrons moving in an effective potential. In the new non-interacting system, the many-body interactions are absorbed into the exchange-correlation energy functional, $E_{\mathrm{xc}}[\rho(\mathrm{r})]$. Consequently, the accuracy of DFT calculations depends on the success of $E_{\mathrm{xc}}[\rho(\mathrm{r})]$ in describing the system of interest. Fortunately, relatively simple approximations to $E_{\mathrm{xc}}[\rho(\mathrm{r})]$ often yield satisfactory results [8]. Throughout this work, the Vienna *ab initio* simulation package (VASP) [10] is employed for DFT implementation.

2.2.1 Functionals

The simplest approximation of the exchange-correlation energy assumes that $E_{\mathrm{xc}}[\rho(\mathrm{r})]$ only depends on the charge density at each point in space and is independent of

the charge density at other locations. This approach is known as the local density approximation (LDA) and is adequate for slowly varying $\rho(r)$ [8]. Since LDA provides insufficient descriptions of some systems, the generalized gradient approximation (GGA) is more commonly used. The semilocal GGA approach additionally depends on the gradient of $\rho(r)$ at each point and is therefore better equipped to describe sharper changes in $\rho(r)$. Widely used GGA schemes include the functionals developed by Perdew and Wang (PW91) [11] and Perdew, Burke, and Ernzerhof (PBE) [12].

2.2.2 Pseudopotential Approximation

The physical and chemical properties of most materials in the solid state are a much stronger function of valence electrons than the tighter-bound core electrons. As a result, significant reduction in computational requirements is possible if atomic potentials can be reduced to functionally comprehend only the essential valence electrons. In the pseudopotential approximation [8], the true system is decomposed into a valence electron contribution and a combined contribution from the nucleus and core electrons. An ideal atomic pseudopotential reproduces the same wavefunction shape outside the core region as the fully-represented atom, while reducing the number of nodes and singularities inside the core region, which reduces both planewave and computational requirements. Harder pseudopotentials demand more planewaves, while softer pseudopotentials reduce planewave and cut-off energy requirements. Two common pseudopotentials, Vanderbilt-type ultrasoft pseudopotentials (US-PPs) [13] and projector-augmented wave (PAW) pseudopotentials [14], are used throughout this work.

2.3 Structure Generation Methods

Atomistic construction of pure, crystalline, solid-state structures is relatively straight-forward in a supercell context in which mathematical relationships can be

exercised to expand the crystal from the base unit cell in real-space or the equivalent primitive cell in reciprocal space. In crystallography, symmetry considerations in three dimensions provide seven distinct crystal lattice systems and fourteen Bravais lattices which provide a systematic foundation to categorize crystals [8]. Examination of pure, crystalline semiconductors provides an important foundation for understanding the relationship between physical and electronic structure, which ultimately governs observable material properties.

Generation of more complex atomic-scale configurations requires considerably more effort, yet is essential to first-principles exploration of material defects, amorphous networks, and intricate nanostructures. Atomistic structure generation is commonly accomplished via two methods, molecular dynamics (MD) or Monte Carlo (MC) simulations, coupled to various interatomic potentials [15].

Two popular MD methods are *ab initio* and classical MD simulations. *Ab initio* MD permits accurate description of atomic configurations, but its utility is constrained to small systems and short time scales because of steep computational requirements. Classical MD facilitates relatively large system simulations, but the same time scale limitations can compromise complete structural relaxation and the availability of reliable force fields for bond formation/scission is also a concern.

Classical MC based on a continuous random network (CRN) model [16] is a proven approach for the construction of various fully-relaxed, fourfold-coordinated (FC) structures [15,17-23]. Within the CRN framework, both amorphous systems and embedded defect clusters can be relaxed via a large number of bond transpositions [24] using Metropolis Monte Carlo (MMC) sampling with a reliable force field to capture structural energetics. Since MC sampling obviates the need for reliable bond formation/scission descriptions, computationally less expensive valence force field

models, such as three-body, harmonic Keating-like potentials [25], can be used to construct relatively large systems. These techniques are collectively identified as a CRN-MMC simulation procedure, which constitutes the primary methodology used to construct the atomistic configurations studied herein.

2.4 Fundamentals of Elasticity

For isotropic materials, a scalar form of Hooke's Law is sufficient to describe the linear elastic relationship between stress (σ) and strain (ε) in a solid as

$$\sigma = Y\varepsilon, \tag{2.4}$$

where Y is the elastic or Young's modulus. However, crystals are inherently anisotropic, so many properties are orientation-dependent. Consequently, Y depends on the crystal direction in which stress is applied and strain deformation occurs. In their most general forms, stresses and strains are second-rank tensors related by fourth-rank tensors. Eqns. 2.5 and 2.6 are tensor representations of Hooke's Law:

$$\boldsymbol{\varepsilon}_{ij} = \mathbf{S}_{ijkl}\boldsymbol{\sigma}_{kl}\,, \tag{2.5}$$

$$\boldsymbol{\sigma}_{ij} = \mathbf{C}_{ijkl}\boldsymbol{\varepsilon}_{kl}\,, \tag{2.6}$$

where $\mathbf{S}_{ijkl}$ is a fourth-rank tensor of $3^4 = 81$ elastic compliances and $\mathbf{C}_{ijkl}$ is a fourth-rank tensor of 81 elastic stiffness constants [26]. Fortunately, physical arguments of symmetry and mechanical equilibrium in a solid quickly simplify the number of independent stiffness constants to 21, which becomes tractable in matrix form [27]. Additional symmetry constraints in the cubic crystal system (Si) in which all three independent lattice constants are equal and all three crystal axes are orthogonal reduce the number of independent $\mathbf{C}_{ij}$ to merely three. In matrix form, anisotropic elasticity in cubic *c*-Si reduces to the following form [27,28]:

$$\begin{bmatrix} \sigma_{xx} \\ \sigma_{yy} \\ \sigma_{zz} \\ \tau_{yz} \\ \tau_{zx} \\ \tau_{xy} \end{bmatrix} = \begin{bmatrix} C_{11} & C_{12} & C_{12} & 0 & 0 & 0 \\ C_{12} & C_{11} & C_{12} & 0 & 0 & 0 \\ C_{12} & C_{12} & C_{11} & 0 & 0 & 0 \\ 0 & 0 & 0 & C_{44} & 0 & 0 \\ 0 & 0 & 0 & 0 & C_{44} & 0 \\ 0 & 0 & 0 & 0 & 0 & C_{44} \end{bmatrix} \cdot \begin{bmatrix} \varepsilon_{xx} \\ \varepsilon_{yy} \\ \varepsilon_{zz} \\ \gamma_{yz} \\ \gamma_{zx} \\ \gamma_{xy} \end{bmatrix}. \quad (2.7)$$

An epitaxial Si film is a special case with additional constraints that allows further simplification of Eqn. 2.7. In this case, the in-plane (||) directions in the epitaxial film are chosen as x and y and film growth occurs in the out-of-plane (⊥) z direction. For strained epitaxial growth, the x and y normal stress components are equal ($\sigma_{xx} = \sigma_{yy} = \sigma_{||}$) and result in equal strain in the x and y directions ($\varepsilon_{xx} = \varepsilon_{yy} = \varepsilon_{||}$). Although no stress ($\sigma_{zz}$) is imparted on the epitaxial layer in the z direction, the strain in the z direction, ε_{zz}, is still non-zero. Coherent strain in the epitaxial film only results in normal strain producing tetragonal deformation, so all shear strain components in Eqn. 2.7 fall out. Application of epitaxial film growth constraints to the cubic system in Eqn. 2.7 produces the relationship in Eqn. 2.8 [29]:

$$\begin{bmatrix} \sigma_{||} \\ \sigma_{||} \\ 0 \end{bmatrix} = \begin{bmatrix} C_{11} & C_{12} & C_{12} \\ C_{12} & C_{11} & C_{12} \\ C_{12} & C_{12} & C_{11} \end{bmatrix} \cdot \begin{bmatrix} \varepsilon_{||} \\ \varepsilon_{||} \\ \varepsilon_{\perp} \end{bmatrix}, \quad (2.8)$$

where the first and second rows are dependent and the third row of the matrix equation produces a simple relationship in terms of the strains of interest in the biaxial strain scheme.

2.5 Applied Strain Schemes

Implementation of applied strain in first-principles atomistic modeling requires meticulous manipulation of the supercell dimensions. In this work, three different types of uniform strain fields will be investigated in bulk Si: hydrostatic, biaxial, and uniaxial.

Custom Perl scripts were widely applied to facilitate and manage repeated VASP simulations to systematically implement strain modulation in each of these three strain schemes.

2.5.1 Hydrostatic Strain

Modeling hydrostatic strain conditions is identical to simulating a uniform pressure field applied to the material system and is consequently the simplest of the uniform strain fields. Since this case is inherently isotropic, generating the modified hydrostatic lattice constants simply requires applying the same percent change to all three independent directions.

2.5.2 Biaxial Strain

2.5.2.1 ELASTIC THEORY

To calculate modified lattice constants for biaxially-strained Si, it is essential to quantify the Poisson effect from the relationships developed in Section 2.4. Based on the geometric scheme depicted in Fig. 2.1, the biaxial Poisson effect can be quantified by introducing a quantity, ν^*, that represents the ratio of in-plane strain ($\varepsilon_{\parallel}$) to out-of-plane strain ($\varepsilon_{\perp}$). In this system, the values of $a_{\parallel}$ in Si under tensile strain conditions are equal to representative values of a_{SiGe}, which is the lattice constant of a binary SiGe system. The in-plane strain is computed as $\varepsilon_{\parallel} = (a_{SiGe}\text{-}a_{Si})/a_{Si}$ and the out-of-plane strain as $\varepsilon_{\perp} = (a_{\perp}\text{-}a_{Si})/a_{Si}$. The experimental value of a_{Si} is 5.4309 Å and a_{Ge} is 5.6461 Å [30], so 4% tensile strain is the limiting case of Si grown over pure Ge. From linear elastic theory [29-32], the relationship between out-of-plane and in-plane strain for a cubic crystal can be expressed in terms of two elastic stiffness constants,

$$\nu^* = -\varepsilon_{\perp}/\varepsilon_{\parallel} = 2(C_{12}/C_{11}), \tag{2.9}$$

which is a simple rearrangement of the third row of Eqn. 2.8. Using tabulated values [33] for C_{11} and C_{12}, the value of ν^* is 0.771. Using ν^* and the expressions for $\varepsilon_{\parallel}$ and $\varepsilon_{\perp}$, values of $a_{\perp}$ can be calculated for each independent value of $a_{\parallel}$ studied. All results presented for biaxially-strained Si are based on $\nu^* = 0.771$. By iterating through a reasonable range of $a_{\perp}$ for each value of $a_{\parallel}$ studied, it was numerically verified that minimum energy supercell dimensions occur as ν^* converges to 0.771.

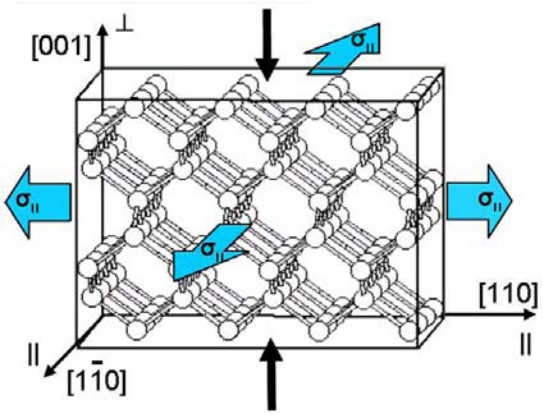

Figure 2.1: (Color available) Tensile biaxial stress/strain interaction in a model Si supercell. In the figure, applied tensile stress, $\sigma_{\parallel}$, in the plane of the substrate acts equally in all directions as shown by block arrows and produces a tensile strain. In response, the lattice contracts in the out-of-plane direction as shown by the solid black arrows. Under compressive strain conditions, the directions of all arrows are inverted.

2.5.2.2 SYMMETRY CONSIDERATIONS

For biaxial strain, there are two significant orientations of interest for compact clusters. The core and strained nearest neighbors in the ground-state, tetra-interstitial configuration (I_4) are presented in Fig. 2.2 as a pedagogical example to convey the significance of cluster symmetry in a biaxial strain scheme [34,35]. Examination of the figure shows the I_4 cluster contains three C_2 symmetry axes. When the I_4 cluster core is embedded in bulk Si, these three C_2 axes map onto the three equivalent <100> directions

in the crystal. The I_4 core and neighbor atoms will experience out-of-plane strain along the C_2^1 axis (coincides with S_4 rotation-reflection axis) and in-plane strain along the C_2^2 and C_2^3 axes under biaxial strain conditions as portrayed in Fig. 2.1. Since biaxial conditions eliminate one degree of freedom in the system, two cluster orientations, rather than three, are potentially unique. This orientation-dependent strain modeling will be extended to other initial cluster orientations ("A") in Chapters 3, 4, and 5 by casting alternative orientations ("B") by transforming the out-of-plane cluster alignment to in-plane alignment.

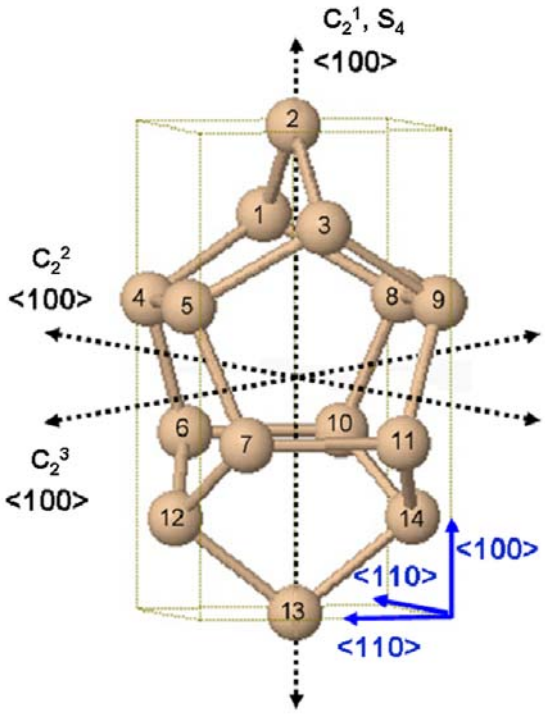

Figure 2.2: (Color available) Cluster core and strained nearest neighbors that comprise the D_{2d} symmetry of the I_4 structure shown isolated from the Si lattice. An S_4 rotation-reflection axis is coincident with the C_2^1 axis. Each C_2 axis is aligned with one of the <100> directions in the Si crystal. The blue axes along the bounding box provide reference to the supercell orientation.

With reference to the crystal, this transformation moves the out-of-plane alignment from the [001] direction to either the [100] or [010] directions. For the model system depicted

in Fig. 2.1, [100] and [010] are equivalent directions with respect to biaxial strain. For completeness, note that other orientations can be generated through pure rotation of the cluster applied to these two important "A" and "B" orientations, but these orientations have the most influence on strain-dependent cluster stability.

2.5.3 Uniaxial Strain

2.5.3.1 ELASTIC THEORY

Calculating modified lattice constants for uniaxially-strained Si is more involved than the biaxial case because it is necessary to determine the Poisson ratios (ν) for two pairs of independent crystal directions. An illustration of a Si supercell experiencing uniaxial strain is provided in Fig. 2.3. In this case, an independent stress, $\sigma_{[110]}$, results in a corresponding strain, $\varepsilon_{[110]}$. In response, the crystal lattice will experience strain deformation of opposite sign along both $[1\bar{1}0]$ and [001], but the magnitude of strain in these directions will be different because of the anisotropic nature of the crystal. To estimate the magnitudes of both dependent strains, $\varepsilon_{[1\bar{1}0]}$ and $\varepsilon_{[001]}$, the ν between [110] and $[1\bar{1}0]$ and the ν between [110] and [001] must be calculated. Brantley [36] derived a generalized expression using tensor mathematics to compute ν between two arbitrary crystallographic directions in a cubic crystal using elastic compliances:

$$\nu = -\frac{s_{12} + (s_{11} - s_{12} - \tfrac{1}{2}s_{44})[l_1^2 m_1^2 + l_2^2 m_2^2 + l_3^2 m_3^2]}{s_{11} - 2(s_{11} - s_{12} - \tfrac{1}{2}s_{44})[l_1^2 m_2^2 + l_2^2 m_3^2 + l_1^2 m_3^2]}, \tag{2.10}$$

where $\mathbf{s}_{ij}$ are the three independent elastic compliances for a cubic system, and $\mathbf{l}_i$ and $\mathbf{m}_i$ are direction cosines for **l** (independent strain direction) and **m** (dependent strain direction), respectively, relative to the <100> directions.

Using Brantley's expression, the desired Poisson ratios are computed as follows:

$$\nu_{[110],[001]} = -\frac{\varepsilon_{[001]}}{\varepsilon_{[110]}} = 0.361\ , \tag{2.11}$$

$$\nu_{[110],[1\bar{1}0]} = -\frac{\varepsilon_{[1\bar{1}0]}}{\varepsilon_{[110]}} = 0.064\ . \tag{2.12}$$

These arithmetically computed values are consistent with graphical results published by Wortman and Evans [37]. With the Poisson ratios known and $\varepsilon_{[110]}$ independently defined as the percent strain imposed on the system, $\varepsilon_{[1\bar{1}0]}$ and $\varepsilon_{[001]}$ are easily determined. With the strain relationships between crystallographic directions identified, it is relatively straight-forward to tabulate uniaxially-modified values of $a_{[1\bar{1}0]}$ and $a_{[001]}$ for each independent value of $a_{[110]}$ studied.

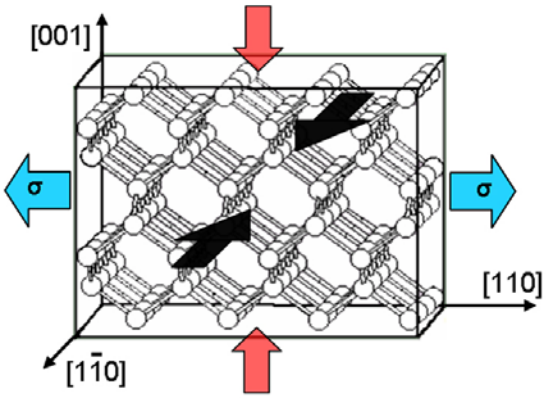

Figure 2.3: (Color available) Tensile uniaxial stress/strain interaction in a model Si supercell. For this case, tensile stress, σ, is independently applied along [110] and results in a corresponding strain along [110]. In response, the lattice dependently contracts along both $[1\bar{1}0]$ (black arrows) and [001] (red arrows), but the magnitude of the contractions will be different as determined by the respective Poisson ratios. Under compressive conditions, the directions of all arrows are inverted.

2.5.3.2 SYMMETRY CONSIDERATIONS

The uniaxial strain scheme is more general than the biaxial case because there is an additional degree of freedom. In general, any initial cluster orientation can be transformed by interchanging alignment among equivalent crystallographic directions.

Using the ground-state, tri-interstitial configuration (I_3^g) as an example, the C_2 axis shown in Fig. 2.4 can be aligned with the [001], [010], or [100] directions. In the model Si substrate orientation, only two orientations are potentially unique under biaxial strain, but all three are potentially unique in the more general case of uniform uniaxial strain. For some configuration symmetries, pure rotation about a symmetry axis may also change the cluster strain response. Orientation changes between equivalent directions will be designated as primary transformations and pure rotation orientation changes will be designated as secondary transformations for the remainder of this work.

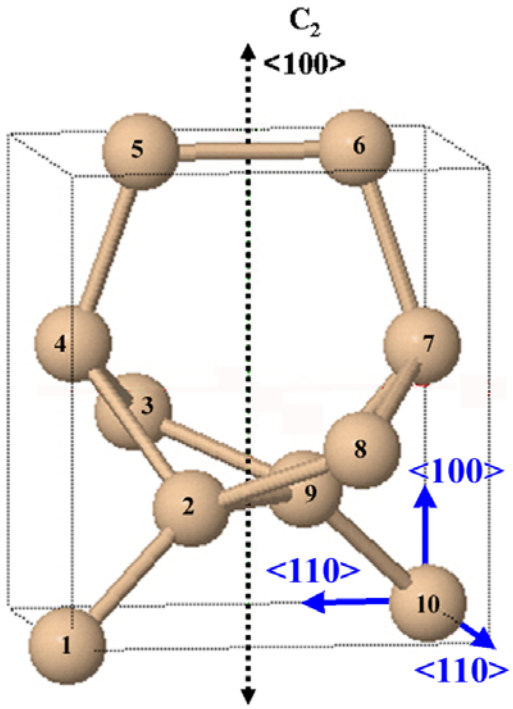

Figure 2.4: (Color available) Cluster core and strained nearest neighbors that comprise the C_2 symmetry of the I_3^g core shown isolated from crystalline Si in the initial "A" orientation. The crystallographic axes (blue) shown provide reference to the supercell orientation. The I_3^g configuration only has a single C_2 symmetry rotation axis shown in black. The atoms are arbitrarily numbered to facilitate discussion.

2.5.4 Orientation Nomenclature

Figure 2.5 defines a simple orientation nomenclature for the various cases reviewed for biaxial and uniaxial strain in this work. Orientation "C" is often degenerate with orientation "A" with respect to uniaxial strain response; however, distinct behavior has been observed among all three orientations "A", "B", and "C" for clusters with significant structural components aligned along <110>. For those cases, "A" and "C" orientations interchange <110> structural alignment between a state that is || with the applied strain and a state that is ⊥ to the applied strain.

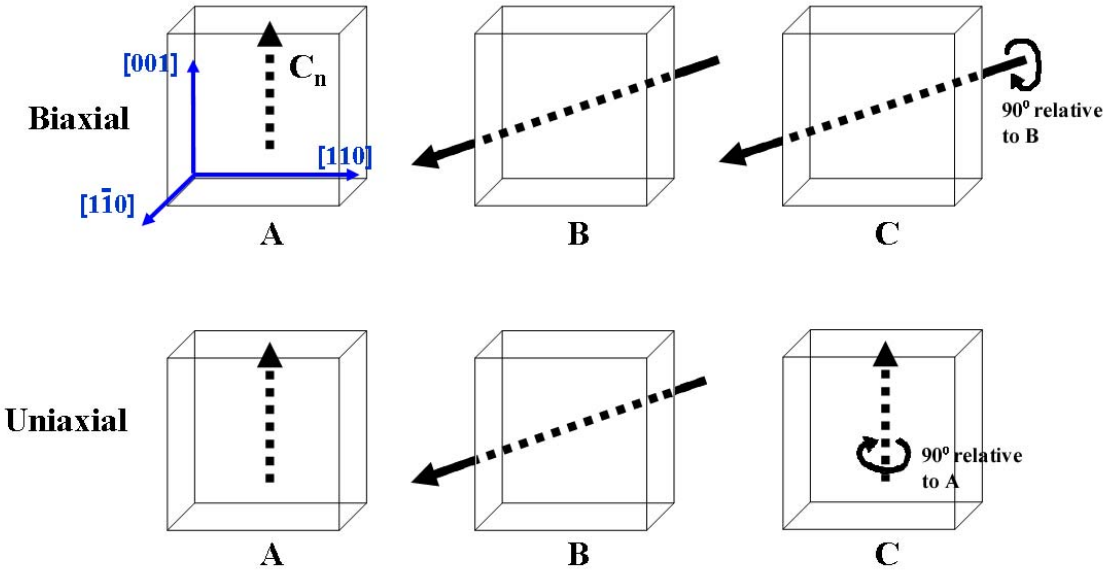

Figure 2.5: Pictorial reference to orientation nomenclature used in this work. An arbitrary C_n axis is assigned to the clusters in the initial orientations labeled "A". A C_1 symmetry designation [38] indicates no non-trivial symmetry operations are present, so, at minimum, a C_1 axis can be applied in an arbitrary fashion to any generic configuration. The "B" orientation is the same for both strain schemes, while the "C" orientations represent pure rotations of the previous orientations, as indicated, that were found to modulate the strain response uniquely relative to either "A" or "B". Biaxial strain is applied throughout this work in the plane containing [110] and [1$\bar{1}$0], while uniaxial strain is applied only along [110].

Note that the orientation-dependent strain behavior reported in this work highlights the most interesting orientations produced both through the integrated atomistic modeling procedure of Lee and Hwang [18-20] and manually-generated orientations produced through mathematical transformations of cluster configurations; therefore, not every conceivable orientation is represented.

2.6 Mechanical Property Calculations

The elastic (or Young's) modulus (Y) was calculated by computing forces and stresses from total energy (E) data using the following relationships:

$$F_x = \left.\frac{\partial E_x}{\partial x}\right|_{x=\varepsilon}, \tag{2.13}$$

$$\sigma_{xx} = \frac{F_x}{A}, \tag{2.14}$$

$$Y = \frac{\sigma_{xx}}{\varepsilon}. \tag{2.15}$$

Forces along a given direction (F_x) were calculated for each strain condition (ε) using second order numerical derivatives in Eqn. 2.13, normal stresses (σ_{xx}) were subsequently evaluated with Eqn. 2.14 (A represents the supercell face area in the x direction), and ultimately Young's modulus is obtained from Eqn. 2.15 as the ratio of stress to strain in the x direction.

The bulk modulus (B), which is the 3-D analog of Y, can be calculated from total energy data as

$$B = V\left.\frac{\partial^2 E}{\partial V^2}\right|_{V=V_i} = \frac{\partial E / \partial V}{\Delta V / V_o} = \frac{\text{volumetric stress}}{\text{volumetric strain}}, \tag{2.16}$$

where V_o is the equilibrium cell volume, $\varepsilon_v=\Delta V/V_o$ is an arbitrary volumetric strain, and V_i is the cell volume at an arbitrary ε_v. The work of Mehl [39] provides a similar

computational approach to calculate B, except $E(V_i)$ data is mathematically fit to an isothermal equation of state described by Birch [40] with subsequent analytic differentiation, whereas the present method substitutes the approximation inherent in fitting with the approximation inherent in a statistical approach.

2.7 Electronic Structure Calculations

Self-consistent solution of the Kohn-Sham equations during DFT simulation produces eigenvalues characterizing the ground-state electronic structure of the system. Extraction of resulting eigenstates can be used to generate both density of states (DOS) and band structure analyses, which are essential in studying semiconductor band gaps (E_g). A DOS analysis is widely applicable and characterizes the electronic structure via a histogram of states on an energy level spectrum. A band structure analysis is only meaningful in systems where long-range periodicity is present. Band structure is conventionally illustrated as energy band variation (or dispersion) as a function of **k** along high-symmetry directions in the Brillouin zone (BZ) [7].

2.8 Optical Property Calculations

The optical properties of a material are directly derived from the fundamental electronic structure. A four-step optical calculation procedure was adopted to compute the complex frequency-dependent dielectric function with VASP following the general theoretical framework described by Adolph *et al.* [41] and cited in other recent computational studies for other material systems [42-45]. This calculation procedure is based on the independent-particle approximation, so quasiparticle self-energy corrections, local-field effects, and excitonic contributions are neglected. The application-specific details of the method will be presented in each relevant chapter.

The essential components of the four-step computational procedure are as follows: (1) structural relaxation of ionic positions, (2) calculation of the charge density distribution, (3) determination of the frequency-dependent dielectric matrix using an adequate number of conduction bands for sampling optical transitions, and (4) computation of the complex dielectric function [$\varepsilon(\omega) = \varepsilon_1(\omega) + i\varepsilon_2(\omega)$]. The OPTICS code of Furthmüller [46] was used throughout this work to obtain both the imaginary (ε" or ε_2) and real (ε' or ε_1) parts of ε(ω). The imaginary part of ε(ω) (in atomic units) is computed by summation over the frequency-dependent dielectric matrix elements in isotropic materials using

$$\mathrm{Im}[\varepsilon(\omega)] = \varepsilon_2(\omega) = \frac{4\pi^2}{\Omega\omega^2} \sum_{i\in VB, j\in CB} \sum_{\mathbf{k}} w_{\mathbf{k}} \left| p_{ij} \right|^2 \delta(\varepsilon_{\mathbf{k}j} - \varepsilon_{\mathbf{k}i} - \omega), \qquad (2.17)$$

where Ω is the unit cell volume, VB represents the valence band, CB represents the conduction band, $w_{\mathbf{k}}$ is a weighting associated with a k-point **k**, and $\varepsilon_{\mathbf{k}n}$ represent energy levels in their respective bands [42]. Transition matrix elements in Eqn. 2.17 are represented by $p_{ij} = \langle \mathbf{k}_i | \hat{p} | \mathbf{k}_j \rangle$, where the $|\mathbf{k}_n\rangle$ are Bloch state wavefunctions with momentum **k**. The longitudinal form [10,42,47] of the dielectric matrix was used in the VASP calculations throughout this work. When the imaginary part of ε(ω) is known for all photon energies, application of the Kramers-Kronig transformation (in atomic units),

$$\mathrm{Re}[\varepsilon(\omega)] = \varepsilon_1(\omega) = 1 + \frac{2}{\pi} \mathbf{P} \int_0^\infty \frac{\omega' \varepsilon_2(\omega')}{\omega'^2 - \omega^2} d\omega', \qquad (2.18)$$

where **P** represents the principal integral value, allows subsequent evaluation of the real component of ε(ω). Calculations of optical transitions up to 20 eV was found sufficient to obtain the key features in the dielectric function spectra. With ε(ω) determined, it is relatively straight-forward to derive other linear optical properties including refractive

index, reflectivity, absorption coefficient, optical conductivity, and electron energy loss spectra [48,49].

2.9 DFT Correction Methods

The DFT-GGA approach employed throughout this work characteristically underestimates E_g and consequently the absorption edge in optical calculations, but the resulting qualitative trends shown are considered reliable. Numerous correction methods have been reported to address the electronic band structure deficiencies of DFT, but each method necessitates additional trade-offs and the most appropriate correction scheme is often dictated by the material system. Hybrid functionals use a mixture of Hartree-Fock (HF) exchange-correlation with local or semilocal density functionals (GGA) to improve semiconductor E_g representations, but HF evaluation in periodic systems can be computationally-expensive and the ratio of HF/DFT representation is an additional variable [50]. The quasiparticle GW method demands significantly more computational expense because the solution of single-particle Kohn-Sham equations in DFT is supplanted by calculation of both the dielectric function and single-particle Green function via rigorous solution of the Dyson equation [51]. Application of either correction method in the current work would generally be cost-prohibitive because of the large supercells required to represent complex atomistic structural models.

Chapter 3

Strain Effects on Si Self-Interstitial Clusters (I_n)

3.1 Introduction

Strain engineering is a useful technique to modify many important material properties and effectively create new, advanced materials. For electronic applications, strain engineering has received intense attention in the semiconductor industry over the last decade as a low-cost, easily-integrated method to extend Si complementary metal oxide semiconductor (CMOS) transistor performance [52]. Consequently, the semiconductor industry began widely incorporating process-induced strain into manufacturing flows with the introduction of the 90 nm node as a cost effective technique to help extend transistor performance improvement consistent with Moore's Law.

Ion implantation creates Si self-interstitial defects that are associated with transient-enhanced diffusion (TED) of dopants during post-implantation annealing, which results in degradation of dopant profiles that are critical in the formation of ultrashallow junctions. Small interstitial clusters are also thought to be involved in the evolution of {311} extended defects [53-56]. Recent experimental work has succeeded in providing further insight into the behavior of small interstitial clusters using techniques such as deep-level transient spectroscopy (DLTS) and photoluminescence (PL) spectroscopy from ion-implanted Si substrates [53,54]. Numerous, recent publications acknowledge the general trend that interstitial clusters become more stable as size increases, as well as the particularly stable local minima structures observed at $n = 4$ and $n = 8$ [53,57,58]. Small clusters (I_n, $n \leq 4$) are of importance as either highly-mobile species (I_n, $n = 1,2$)

during high temperature annealing processes and/or as constituent components of larger clusters.

There are two ways of technological relevance to apply strain to the channel of a metal oxide semiconductor field effect transistor (MOSFET): biaxial strain, which is sometimes called global or bulk strain because it is implemented at the substrate level, and uniaxial strain, which is sometimes referenced as local or process-induced strain [59]. Tensile biaxial strain can be implemented in a transistor channel by building the entire device in strained Si epitaxy over a thick $Si_{1-x}Ge_x$ layer. Uniaxial strain is often implemented at the device level in two ways: (1) selective epitaxial growth of a binary Si alloy ($Si_{1-x}Ge_x$ for channel compression, $Si_{1-x}C_x$ for channel tension) in the source/drain recessed regions to impose strain along the transistor channel direction or (2) deposition of a high-stress silicon nitride cap layer which mechanically couples the local strain of the film into the underlying transistor channel. Hydrostatic strain can be achieved in bulk Si simply by subjecting the material to a uniform pressure field, but this form is technologically less relevant than biaxial or uniaxial strain.

For technological applications, uniaxial strain is likely most prevalent as it is preferred in most CMOS processes for ease of manufacturability and better electrical performance return [52,60]. Major applications for biaxial strain include devices with heterojunctions such as heterojunction bipolar transistors (HBTs) and modulation-doped field effect transistors (MODFETs) for analog microwave circuits [61]. Biaxial strain also appears promising for fabricating fully-depleted CMOS devices using strained silicon-on-insulator (sSOI) substrates [62]. Hydrostatic strain is rarely, if ever, used in device applications, but it is conceivable that localized, non-uniform hydrostatic strain fields could exist inside new material systems such as embedded Si nanocrystals [17,63].

In this chapter, the model case of neutral, small interstitial Si clusters in a uniform strain field is examined, which might occur in the middle of a MOSFET transistor with a <110>-aligned channel. A (100) wafer orientation is used in the atomic models because this substrate is dominant in CMOS manufacturing. The generation of most clusters (I_n, $n \geq 3$) studied was accomplished using the integrated atomistic modeling procedure of Lee and Hwang [18-20] which combines CRN-MMC, tight-binding molecular dynamics (TBMD), and DFT simulations. The majority of the work presented in this chapter was previously published [64,65].

3.2 Computational Details

The optimized atomic structures and energies reported in this chapter were computed using a planewave basis set pseudopotential method within the generalized gradient approximation of Perdew and Wang (GGA-PW91) [11] to DFT [66], as implemented in VASP [10]. Vanderbilt-type ultrasoft pseudopotentials (US-PPs) [13] were used to represent interactions between ion cores and valence electrons. Outer electron wavefunctions were expanded using a planewave basis set with a kinetic energy cut-off of 160 eV. Brillouin zone (BZ) sampling was performed with one k-point (Γ) for geometric optimization. The geometric optimization allowed all atoms to relax until the total energy had converged within 1×10^{-3} eV tolerance. With the optimized ionic positions determined, corresponding total energies were refined using a $2\times2\times2$ Monkhorst Pack grid. For density of states (DOS) near the Si band gap, subsequent VASP simulations were conducted on the optimized ionic configurations with the Monkhorst Pack mesh increased ($4\times4\times4$) and charge smearing modeled with the tetrahedron method [10].

For the strain-free supercell, an optimized Si lattice constant of 5.457 Å along <100> or 3.859 Å along <110> was used. To evaluate uniaxial, biaxial, and hydrostatic

strain conditions, a basis set of lattice vectors associated with a four-atom supercell was computed for each strain condition (-4% ≤ ε ≤ 4%) and then scaled up to each supercell size investigated. Most clusters reported in this chapter were embedded inside 256-atom supercells, while the larger clusters (n > 4) required 480-atom supercells. Care was taken to ensure that each supercell size was large enough to accommodate a given cluster with no significant interaction with its periodic images.

3.3 Relative Stability Size Dependence

To examine how the presence of biaxial strain influences the stability of small interstitial clusters, ground-state configurations were evaluated in the strain-free condition. As recently reported by Lee and Hwang [18,19], compact geometries are favored when the cluster size is smaller than ten self-interstitials. In Fig. 3.1, the ground-state configurations of small interstitial clusters considered here (I_n, n ≤ 10) are presented; their different perspective views can also be found in the work reported by Lee and Hwang [18,19].

Figure 3.2(a) presents a graphical trend of formation energy dependence on cluster size (n) for the selected conditions of -3%, 0%, and 3% uniform biaxial strain. The formation energy in terms of cluster size (n) and strain condition (ε), $E_f(n, \varepsilon)$, is given by:

$$E_f(n,\varepsilon) = E_{tot}(n,\varepsilon) - \frac{n+N}{N} E_{bulk}(\varepsilon), \tag{3.1}$$

where $E_{tot}(n, \varepsilon)$ is the total energy of the I_n cluster in the $n+N$ atom supercell, n is the size of the interstitial cluster, N is the basis number of atoms in the bulk Si supercell, and $E_{bulk}(\varepsilon)$ is the total energy of the N atom supercell of crystalline Si at a given biaxial strain condition. Each data point represents the lowest formation energy per interstitial for a given strain condition among several configurations and orientations that were examined

for a given cluster size. The results shown for the strain-free case are in good agreement with previous studies [18,19,67-69]. Some debate lingers over the ground-state configuration of I_3, but the present work identifies the fourfold-coordinated (FC) structure in Fig. 3.1(c) as the ground-state. Under the range of strain conditions considered ($-3\% \leq \varepsilon \leq 3\%$), no significant deviation was identified in the ground-state cluster configurations from the strain-free case for the small clusters studied (I_n, $n \leq 10$). Exceeding a magnitude of 3% biaxial strain can cause the atomic configuration and bond topology of certain clusters to change, which will be seen later.

The general behavior observed from the family of E_f curves [Fig. 3.2(a)] is for most cluster configurations to stabilize as strain shifts from compressive to tensile and increasing cluster size also generally lowers E_f per interstitial at a given strain condition. The strain response under 3% compressive conditions is nearly the same as the strain response in the strain-free case, but 3% tensile strain shows a strong stabilizing effect on clusters of all sizes. The response of stabilization with increasing tensile strain is largely monotonic for most configurations. For interstitials, the stabilizing influence of tensile strain can be rationalized as the crystal lattice fundamentally becoming more accommodating to extra atoms as interatomic distances increase. It is worth noting that the minimum energy configurations for $n \geq 4$ typically contain the I_4 compact configuration [18,19].

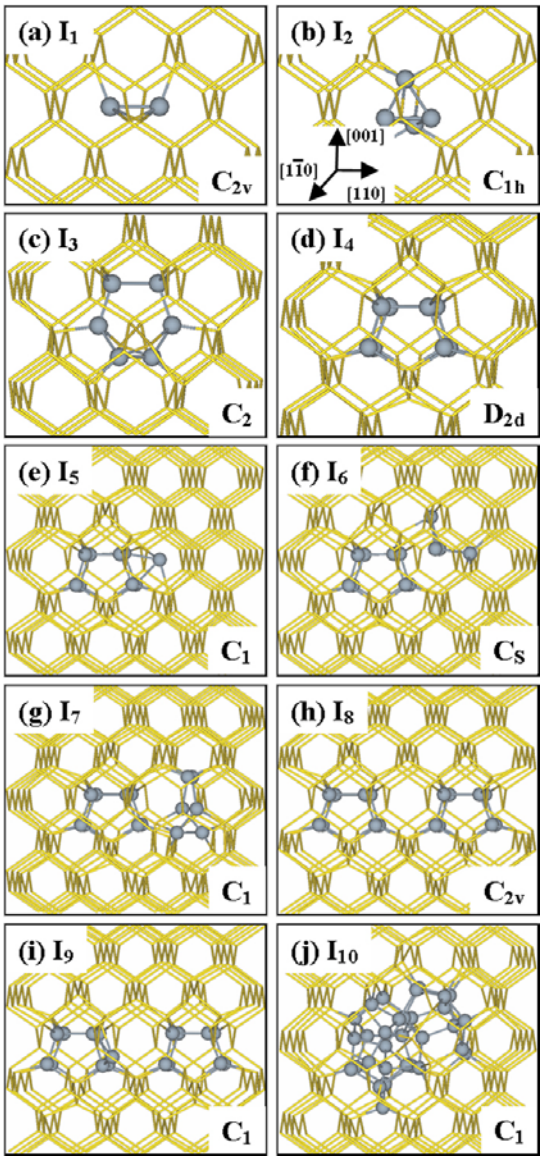

Figure 3.1: (Color available) Ground-state configurations of small self-interstitial clusters (I_n, $n \leq 10$) shown in their initial orientations with corresponding defect symmetries indicated. Light gray (gold) wireframe represents the bulk Si lattice. Dark gray spheres represent interstitial atoms and their highly strained neighbors.

Beyond the general trend of decreasing E_f with increasing cluster size, the local minima at $n = 4$ and $n = 8$ are also interesting. For the strain-free condition, this trend has also been described in a previous study [19] and is consistent with inverse model studies

based on experimental findings [56,57]. Other results in the literature report oscillating behavior in the stability of small interstitial clusters using a variety of computational methods [70,71]. Ortiz *et al.* [57] justify the oscillating behavior in the stability of compact interstitial clusters by claiming that the capture of an extra interstitial by certain cluster sizes can considerably modulate the local stress the cluster imparts on the surrounding lattice. Subsequent lattice relaxation could then lead to a reduction in the system energy. The present simulation results show that the E_f minima at both $n = 4$ and $n = 8$ persist under both compressive and tensile strain conditions. From Fig. 3.2(a), it is also shown that strain of either sign deepens the minima at $n = 4$ and $n = 8$ relative to the E_f of the adjacent cluster sizes.

Annealing of interstitial defects may be preceded by dissociation into smaller clusters; therefore, calculation of cluster binding energies, E_b, with respect to n and ε is also presented. The results are summarized in Fig. 3.2(b). Here, the binding energy, which represents the energy cost for liberation of a single interstitial from a given cluster, is given as follows:

$$E_b(n,\varepsilon) = (n-1)E_f(n-1,\varepsilon) + E_f(1,\varepsilon) - nE_f(n,\varepsilon), \tag{3.2}$$

where all E_f are in units of eV/atom and reference the minimum energy split-<110> configuration of a single interstitial, $E_f(1,\varepsilon)$. The reference $E_f(1,\varepsilon)$ values are computed to be 3.91 eV, 3.76 eV and 3.37 eV under 3% compressive, strain-free, and 3% tensile strain conditions, respectively. The relative stability of I_4 and I_8 is emphasized by local peaks in E_b. Similar to the E_f results, the presence of biaxial strain magnifies the peak E_b at $n = 4$ and $n = 8$. While the I_4 E_b is 2.53 eV in the strain-free case, it increases to 3.83 eV under 3% tensile strain and 3.68 eV under 3% compressive strain. Likewise, the I_8 binding energy increases from 2.90 eV in the strain-free case to 4.37 eV and 4.21 eV

under 3% tensile and 3% compressive strain conditions, respectively. The low E_b of I_5 and I_9 indicate that a single interstitial added to I_4 or I_8, respectively, is not tightly bound to the cluster. The results of the present work suggest that I_4 and I_8 likely play an even larger role in the clustering/dissolution of interstitial defects in strained Si, compared to unstrained Si, because of their increased relative stability over other small, compact clusters.

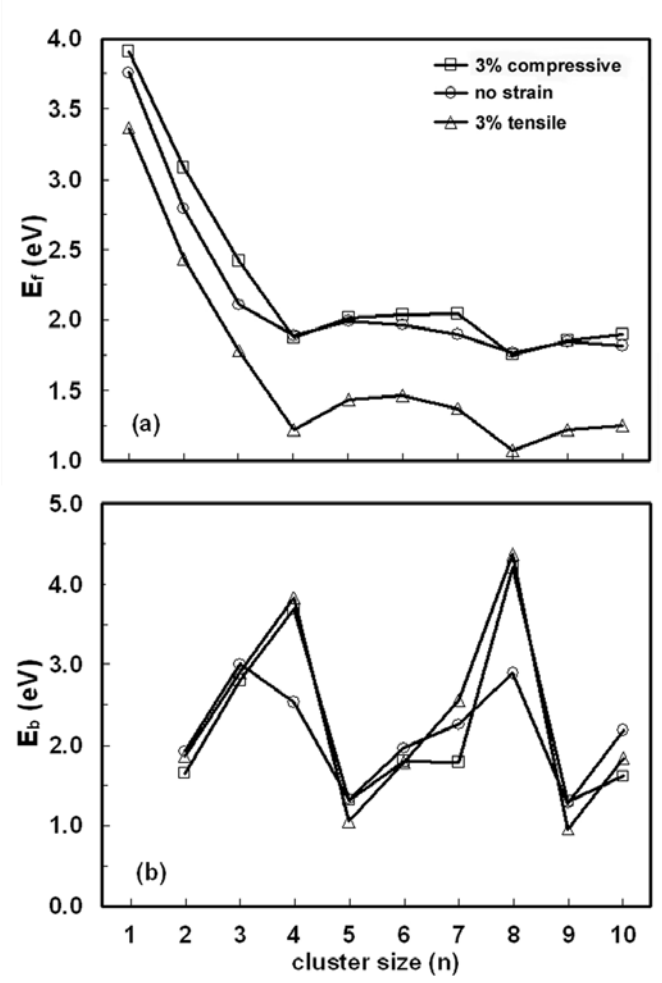

Figure 3.2: Formation energy (a) and binding energy (b) dependence as a function of cluster size for selected strain conditions as indicated. Each data point in (a) represents the most stable of multiple configuration and orientation combinations that were studied for each value of *n*. Binding energies are based on these same minimum formation energies and all reference the split-<110> I_1 configuration.

3.4 Orientation Effect of Cluster Symmetry

The important configurations of the I_4 and I_8 clusters are shown in detail from two different perspectives in Fig. 3.3. A high symmetry perspective is seen along the [001] direction for both clusters. The relative orientation between the two constituent I_4 cores of I_8 within the Si lattice and subsequent effect on the interfacial bond topology was seen to have a non-negligible effect on the formation energy [18,19]. Figure 3.4 shows how E_f varies with biaxial strain for both I_4 and I_8 which highlights the significant impact that cluster orientation within the supercell can produce on cluster E_f. In contrast, the same plots for I_2 and I_3 are included to demonstrate that most clusters, in general, do not exhibit strong orientation-dependent formation energies under strained conditions. I_2 shows no orientation-dependent E_f response, while I_3 shows a weak response. Different cluster orientations often shift the qualification of adequate supercell size to avoid periodic image effects. To avoid excessively large supercell sizes, E_f for all orientations were equated at the strain-free condition to reference the lowest strain-free E_f found. This same E_f reference shift was then applied to all strain conditions. The insets in Fig. 3.4 in all cases show the orientation of the clusters as viewed from out-of-plane with respect to strain. For the I_4 and I_8 structures, the S_4 rotation-reflection axis of the individual I_4 core is shown perpendicular to the plane of strain in the original orientation. In both cases, this represents the highest symmetry perspective of the respective clusters.

The I_4 original orientation, I_4^A, shows nearly invariant response to strain in Fig. 3.4(c) since E_f only varies by 0.01 eV from 3% compressive to 3% tensile strain; however, the alternative orientation, I_4^B, is 1.33 eV more stable at 3% tensile strain than at 3% compressive strain. It is instructive to refer to Eqn. 3.1 and note that the invariant E_f response of the I_4 orientation to strain indicates that the total energy change of the cluster must be nearly identical to the total energy change of *c*-Si in response to strain.

The I_8 cluster exhibits a dual-response strain behavior that is nearly identical to that of I_4. For other cluster configurations with less symmetry [such as I_2 and I_3 as seen in Figs. 3.4(a) and 3.4(b)], the equivalent orientation pair of E_f versus strain curves shows essentially degenerate or weaker orientation-dependence.

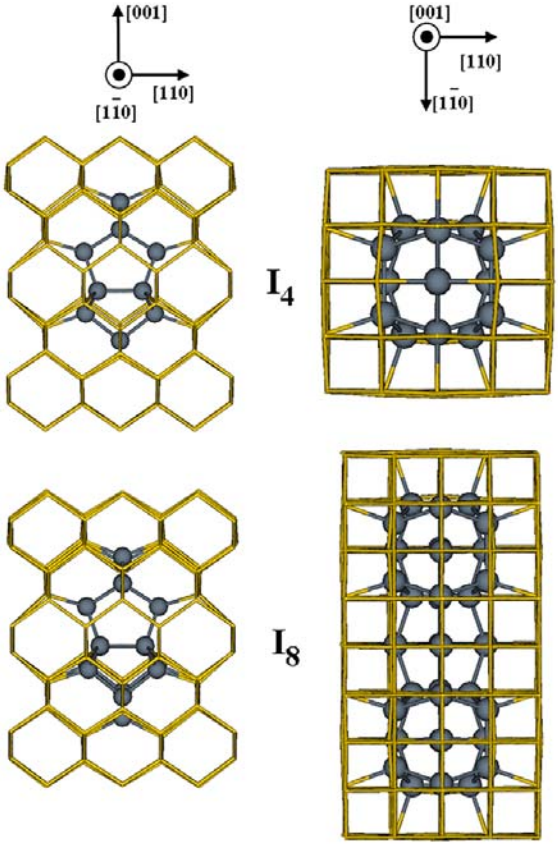

Figure 3.3: (Color available) I_4 and I_8 clusters from two different perspectives embedded inside interior subsections of respective supercells. Light gray (gold) wireframe represents bulk Si atoms in the lattice. Dark gray spheres represent the interstitial atoms and their highly strained neighbors.

Calculations for the present work demonstrate that the particular shape of I_4 with D_{2d} symmetry contributes to its unique behavior. The I_4 core structure was previously introduced in Chapter 2 along with the argument for two relevant orientations in a

biaxially-strained system. Since each C_2 axis is aligned in an equivalent <100> direction in the diamond lattice of Si, it is possible for either orientation to prevail in the same wafer crystal orientation. The sign of strain should determine the prevailing orientation of the I_4 configuration.

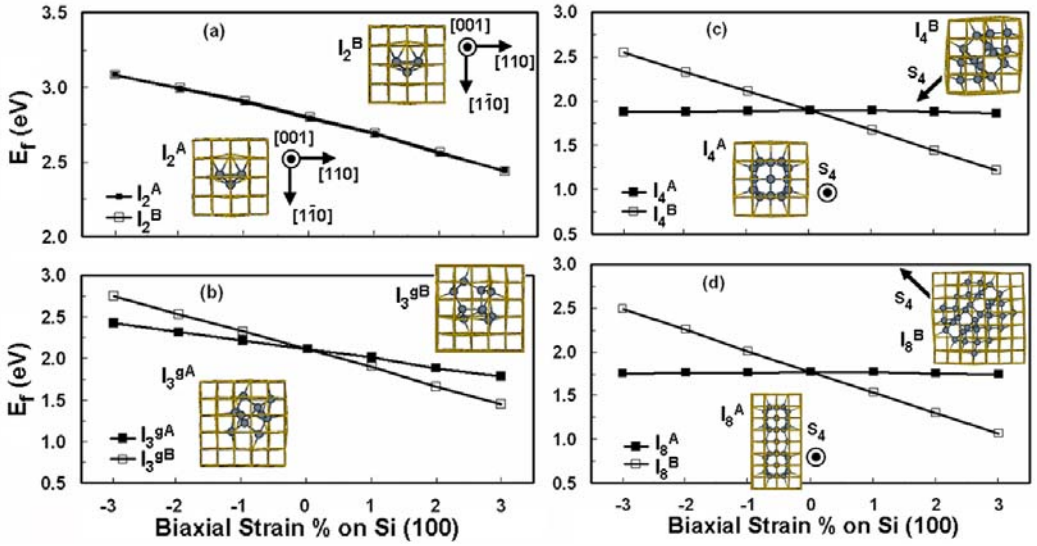

Figure 3.4: (Color available) Formation energy response to biaxial strain for different self-interstitial clusters. Inset graphics illustrate each structure oriented within the supercell. Light gray (gold) wireframe represents the bulk Si lattice. Dark gray spheres denote the highly strained interstitials and neighboring atoms. In all cases, initial orientations are indicated by "A", while alternative orientations are indicated by "B". For (c) and (d), when the S_4 axis is out-of-plane with respect to strain, the structure is in the "A" orientation, while an orientation with this S_4 axis moved into the plane of strain is designated as "B".

3.5 Stability of Small Cluster Configurations

Comprehensive inspection of Fig. 3.1 shows that all ground-state configurations from I_1 through I_9 can be generated using various combinations and orientations of only I_1 through I_4, which motivates further understanding of these structural components. Internally, all interstitial clusters are compressively strained and their disruptive presence to the periodicity of the Si lattice generates localized non-uniform strain fields. External

strain applied to the Si lattice modulates virtually all material properties and the relative stability of intrinsic defects.

3.5.1 Single Interstitial (I_1)

In Fig. 3.5, formation energies are presented for various configurations and orientations of I_1 under both biaxial and uniaxial strain conditions. The split-<110> configuration is well-established as the neutral-state minimum energy configuration in strain-free Si and its strain-free formation energy [$E_f(1,0\%)$] is 3.76 eV. However, these simulation results also suggest that the most favorable configuration changes to the tetrahedral configuration (T) under 4% compressive biaxial strain. At 4% compressive biaxial strain, E_f is 3.83 eV for T and 3.92 eV for the most favorable orientation of the split-<110> configuration. The T configuration of I_1 is actually stabilized by biaxial strain of either sign since a maximum formation energy [$E_f(1,0\%) = 4.10$ eV] is observed in the strain-free case. Similar trends are observed in Fig. 3.5(b) for uniaxial strain, but T exhibits less stabilization under uniaxial strain relative to the biaxial case. In addition, Fig. 3.5(b) shows that uniaxial strain produces three unique $E_f(1,\varepsilon)$ responses for the split-<110> configuration. These results suggest that increased alignment of the split-<110> bond with the direction of applied uniaxial strain ([110]) increases the sensitivity of the $E_f(1,\varepsilon)$ response.

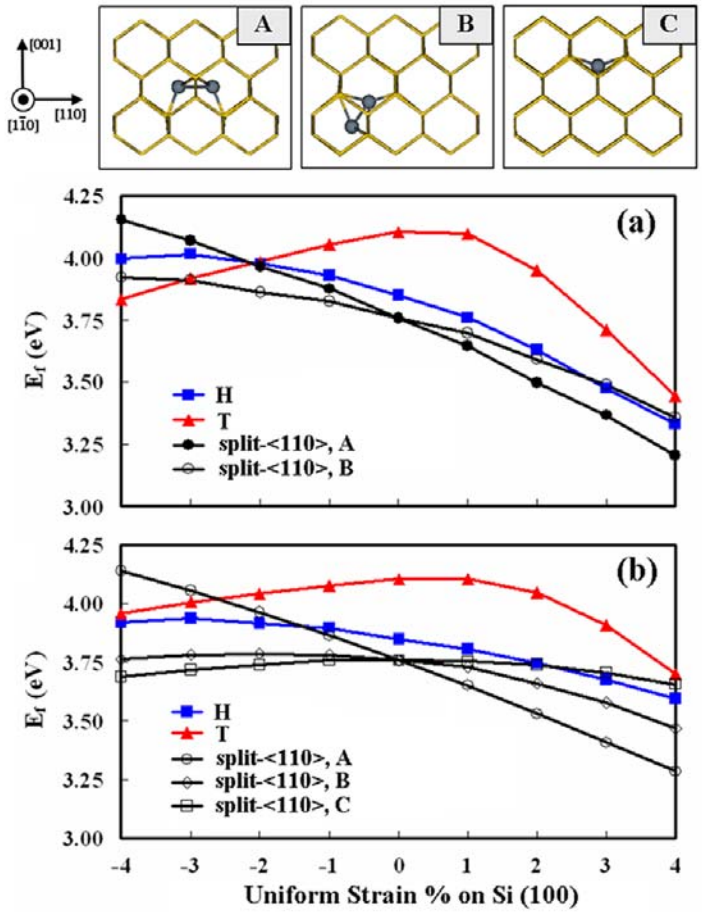

Figure 3.5: (Color available) (a) Formation energy per interstitial for various I_1 configurations/orientations as a function of biaxial strain using 256+*n* supercells. Different configurations are grouped by color. Tensile strain is defined to be positive. The hexagonal configuration is denoted by "H" and the tetrahedral configuration is denoted by "T". (b) Formation energy per interstitial for various I_1 configurations/orientations as a function of uniaxial strain using 256+*n* supercells. (Upper panel) Various reference orientations of split-<110> shown as viewed along [1$\bar{1}$0]. Light gray (gold) wireframe represents bulk Si atoms in the lattice. Dark gray spheres represent interstitial atoms and their highly strained neighbors.

3.5.2 Di-Interstitial (I_2)

In Fig. 3.6, formation energies are presented for various orientations of the I_2 configuration under both biaxial and uniaxial strain. Although initially unique, the "B"

orientation of I_2 is sufficiently similar to "A" such that geometric optimization relaxes "B" back into "A".

Under biaxial strain [Fig. 3.6(a)], the $E_f(2,\varepsilon)$ responses for the two relevant orientations are degenerate, but an interesting distortion of the ground-state configuration is observed at 4% compressive biaxial strain that disrupts the monotonically increasing $E_f(2,\varepsilon)$ trend as strain becomes increasingly compressive. In the strain-free case, the triangle in I_2 formed by atoms 1, 2, and 3 ($\triangle 123$) is isosceles, with the short leg between atoms 1 and 3 measuring 2.29 Å and the long legs measuring 2.45 Å. Under 4% compressive strain, this same group of three atoms shifts up along [001] with respect to the lattice, the 1-3 bond stretches to 2.42 Å, and the remaining legs shrink to 2.43 Å. Under 4% biaxial compression, $\triangle 123$ in I_2 becomes approximately equilateral.

Under uniaxial strain [Fig. 3.6(b)], the $E_f(2,\varepsilon)$ response appears degenerate again for the "A" and "B" orientations, but the "C" orientation shows a more sensitive $E_f(2,\varepsilon)$ response. It is also apparent that uniaxial strain causes less $E_f(2,\varepsilon)$ change per unit change in strain than the biaxial case through comparison of the slopes of the respective $E_f(2,\varepsilon)$ trends for the "A" and "B" orientations of I_2.

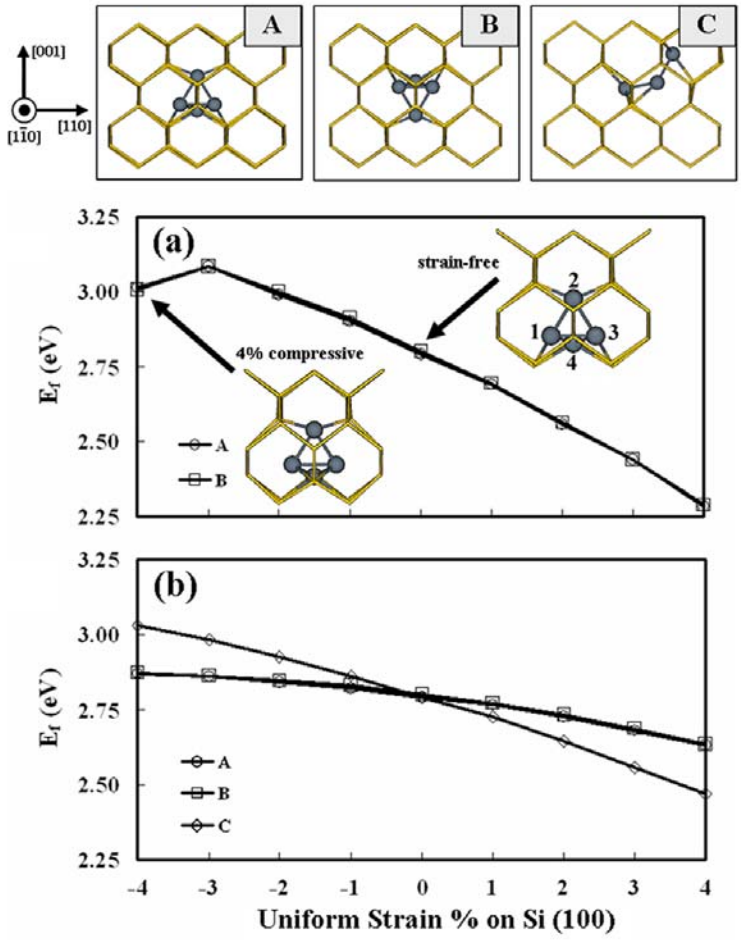

Figure 3.6: (Color available) Formation energy per interstitial for I_2 as a function of (a) biaxial strain and (b) uniaxial strain using 256+*n* supercells. In (a), the insets contrast the two I_2 configurations under 4% compressive and strain-free conditions. Atoms are arbitrarily numbered to facilitate discussion. (Upper panel) Various reference orientations of I_2 shown as viewed along $[1\bar{1}0]$. Light gray (gold) wireframe represents bulk Si atoms in the lattice. Dark gray spheres represent interstitial atoms and their highly strained neighbors.

3.5.3 Tri-Interstitial (I_3)

Using the integrated atomistic modeling procedure of Lee and Hwang [18-20] with biaxial strain conditions, new structures and orientations of Si interstitial clusters were identified, including the previously unreported configuration of I_3 in Fig. 3.7 that

was generated under 4% compressive biaxial strain. The I_3 configuration identified has D_{2d} symmetry, like the I_4 core structure, and also exhibits similar orientation-dependent strain behavior (*vide infra* Fig. 3.10) as previously detailed for I_4. [64]

Figure 3.8 shows how $E_f(3,\varepsilon)$ varies with both biaxial and uniaxial strain for the array of configurations and orientations of I_3 investigated, while Fig. 3.9 shows the corresponding single perspective views along $[1\bar{1}0]$ of each configuration/orientation. These results illuminate the subtle orientation-dependent stability of the ground-state I_3 configuration (I_3^{g}). In addition, Fig. 3.8(a) provides the $E_f(3,\varepsilon)$ response of the compact configuration of I_3 (I_3^{com}) and the new I_3 configuration formed under 4% compressive biaxial strain conditions ($I_3^{4\%c}$). Over the range of biaxial strain conditions investigated ($-4\% \leq \varepsilon \leq 4\%$), Fig. 3.8(a) suggests at least three configurations/orientations of the tri-interstitial could be observed, depending on the strain conditions present: (1) $I_3^{4\%c,A}$ under high compression [$-4\% \leq \varepsilon \leq -2\%$], (2) I_3^{gA} or I_3^{gB} under light compression to strain-free conditions [$-2\% \leq \varepsilon \leq 0\%$], and (3) I_3^{gC} for strain-free to highly tensile conditions [$0\% \leq \varepsilon \leq 4\%$]. The "C" orientation of I_3^{g} was determined as the most energetically stable configuration of I_3 under 4% tensile biaxial strain. It is interesting that the $E_f(3,\varepsilon)$ biaxial response is identical for I_3^{gA} and I_3^{gB}, but different for the secondary transformation of I_3^{gB} into I_3^{gC}. Further examination of each configuration shows that the 9-2 bond of I_3^{g} [Fig. 2.4(a)] is roughly within the plane of strain for both I_3^{gA} and I_3^{gB}, while the 9-2 bond is perpendicular to the plane of strain in I_3^{gC}.

Inspection of Fig. 3.8(a) reveals two important observations about the orientation-dependent strain behavior of $I_3^{4\%c}$. First, $I_3^{4\%c}$ exhibits the largest difference in orientation-dependent biaxial strain response (by quantification of slopes) of any interstitial cluster studied in this work other than I_4. In correlation, $I_3^{4\%c}$ and I_4 are also the only structures studied that have dominant D_{2d} point group symmetry (I_3^{com} is

technically also D_{2d}, but the structure approximately exhibits higher-order T_d symmetry [64]). Second, $I_3^{4\%c,A}$ is the only structure orientation studied in this work that exhibits a positive slope for $E_f(n,\varepsilon)$ as a function of biaxial strain; as a result, $I_3^{4\%c,A}$ is the only structure orientation destabilized by tensile biaxial strain. Most interstitial clusters are stabilized under tensile conditions because the lattice becomes more accommodating to interstitials as it stretches.

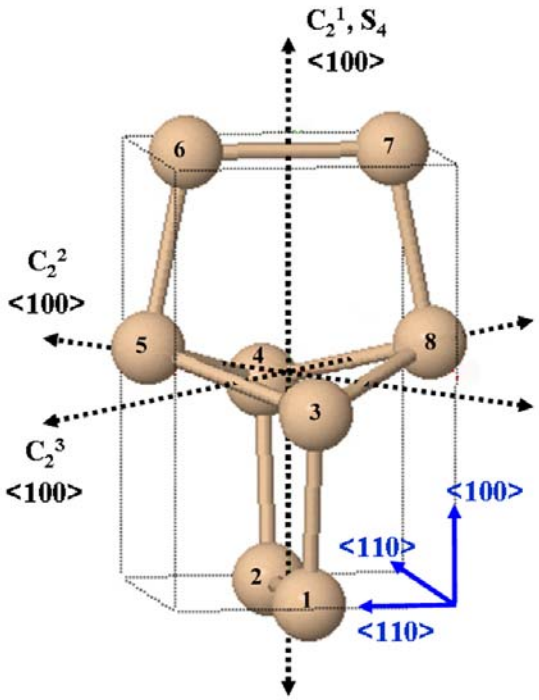

Figure 3.7: (Color available) Cluster core and nearest neighbors that comprise the D_{2d} symmetry of the $I_3^{4\%c}$ structure shown isolated from *c*-Si. The "A" orientation is shown, which is destabilized as strain conditions become more tensile. The axes (blue) shown provide crystallographic reference to the supercell orientation. The atoms shown are arbitrarily numbered to facilitate discussion.

Figure 3.8(b) reveals similar trends for the I_3 structures subjected to uniaxial strain. A notable departure in the uniaxial case includes splitting of the degeneracy in the $E_f(3,\varepsilon)$ responses of I_3^{gA} and I_3^{gB}. Furthermore, the I_3^{g} orientations are energetically more favorable than the $I_3^{4\%c}$ orientations under uniaxial strain of either sign relative to

equivalent magnitudes of biaxial strain. While the $I_3^{4\%c,A}$ structure is favored under 4% biaxial compression, the energetic advantage is gone under 4% uniaxial compression [$E_f(3,-4\%)$=2.28 eV for both I_3^{gB} and $I_3^{4\%c,A}$]. In general, the effect of strain on $E_f(3,\varepsilon)$ responses is diminished for the uniaxial case relative to the biaxial case as evidenced by a reduction in the absolute value of the slope for the uniaxial $E_f(3,\varepsilon)$ response curves; as a result, the difference in strain-free E_f is more dominant in the uniaxial case in evaluation of the relative stability of two structures subjected to the same strain conditions.

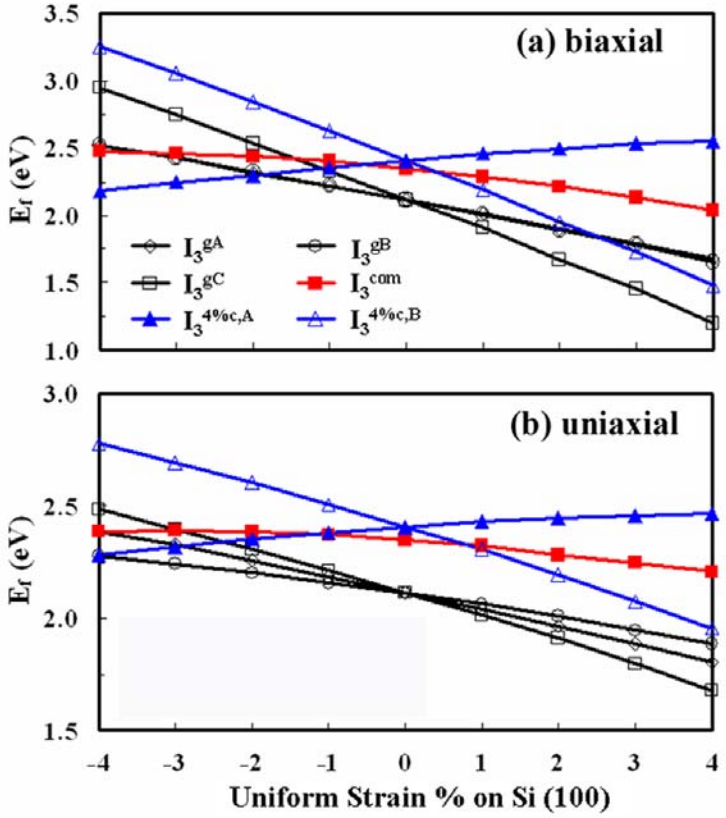

Figure 3.8: (Color available) Formation energy dependence per interstitial as a function of biaxial strain (a) and uniaxial strain (b) for various configurations and orientations of I_3 using 256+n supercells. Different configurations are grouped by color. I_3^g is the most stable configuration under all strain conditions investigated, except for highly compressive biaxial conditions ($\varepsilon \leq -2$) where the $I_3^{4\%c,A}$ structure orientation becomes most favorable.

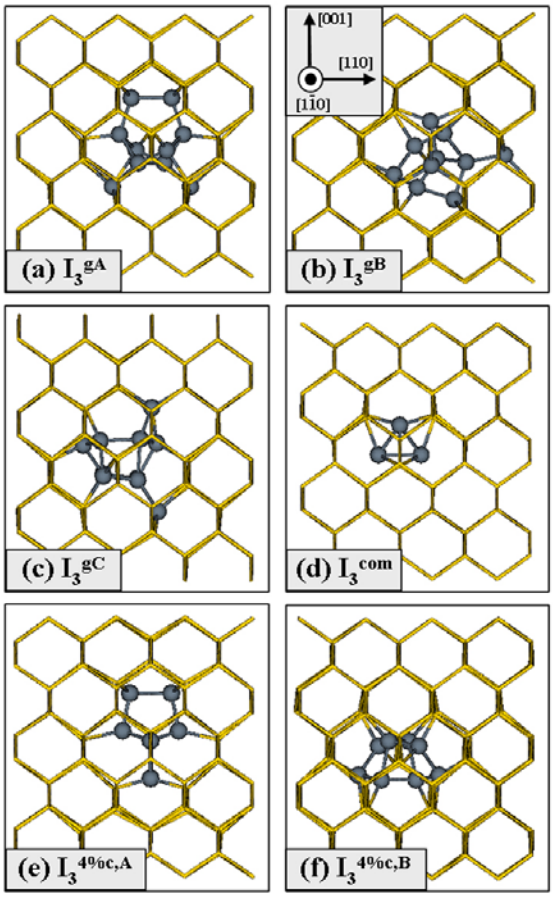

Figure 3.9: (Color available) Various strain-free configurations and orientations of the I_3 cluster embedded inside subsections of their respective 256-atom supercells as viewed along [$1\bar{1}0$]. Symmetries for each configuration are C_2, T_d (approximate), and D_{2d} for I_3^g, I_3^{com}, and $I_3^{4\%c}$, respectively. Light gray (gold) wireframe represents bulk Si atoms in the lattice. Dark gray spheres represent the interstitial atoms and their highly strained neighbors. For each unique configuration, the same number of atoms are represented as spheres to aid comparison across different orientations.

3.5.4 Tetra-Interstitial (I_4)

The previous study [64] of I_4 is extended by examining the $E_f(n,\varepsilon)$ responses under uniaxial, biaxial, and hydrostatic strain for the primary orientations [Fig. 2.5] and these results are provided in Fig. 3.10. $E_f(n,\varepsilon)$ responses are approximately linear for all orientations and strain types studied for I_4. For the strain-free case, $E_f(4,0\%)$ is 1.89 eV.

For I_4^A, the $E_f(4,\varepsilon)$ responses to strain are identical and nearly invariant for both the uniaxial and biaxial conditions. On the other hand, the $E_f(4,\varepsilon)$ curves for I_4^B both show sensitivity to strain, but the uniaxial response to strain is weaker than the biaxial response. The slope of the biaxial $E_f(n,\varepsilon)$ response of orientation "B" is a factor of two greater than the slope of the uniaxial $E_f(n,\varepsilon)$ response. The hydrostatic $E_f(4,\varepsilon)$ response of I_4 is the most sensitive to changes in strain among all strain types and orientations considered. Of most interest is the strong stabilizing effect predicted if hydrostatic tension is present. Overall, a trend is observed for increased strain sensitivity as conditions vary from uniaxial to biaxial to hydrostatic strain. In consequence, the cluster E_f become more sensitive to strain as the degrees of freedom in volumetric relaxation of bulk Si are reduced.

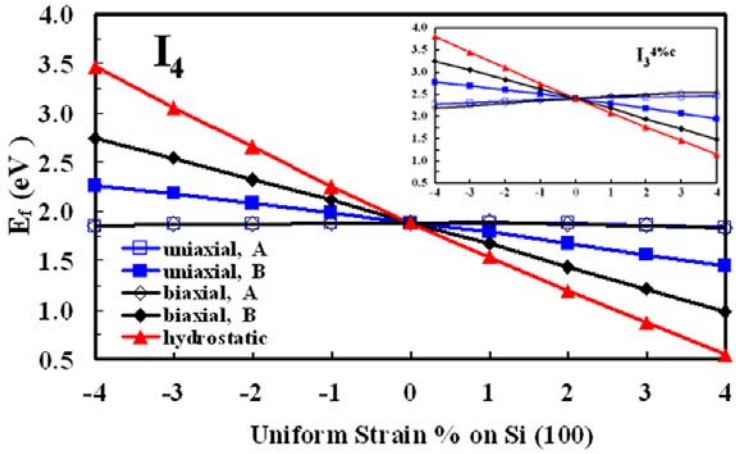

Figure 3.10: (Color available) Formation energy dependence per interstitial of I_4 with D_{2d} symmetry shown for primary orientations and different types of strain conditions using 256+*n* supercells. Strain types are grouped by color. For comparison, the inset shows the same information obtained for the $I_3^{4\%c}$ structure, which also has D_{2d} cluster symmetry. $I_3^{4\%c}$ shows all the same trends in formation energy response behavior to various strain conditions as I_4.

Expecting that the $I_3^{4\%c}$ structure might exhibit analogous behavior in the presence of strain because of its shared D_{2d} symmetry classification with I_4, the same $E_f(n,\varepsilon)$ data is presented in the inset of Fig. 3.10 for comparison. For the strain-free case, $E_f(3,0\%)$ is 2.41 eV for $I_3^{4\%c}$. From Fig. 3.10, $I_3^{4\%c}$ shows all the same $E_f(n,\varepsilon)$ trends as I_4 in correlation with its shared D_{2d} symmetry classification.

3.6 Local Strain Distributions

To further characterize interstitial clusters, atomic-level strain distribution profiles are presented that depict the localized strain fields induced by clusters. In Fig. 3.11, strain distribution profiles are presented based on both strain energy (E_{strain}) and average bond length for I_3^g, $I_3^{4\%c}$, and I_4, all in the "A" orientation. The hybrid ball-and-stick/wireframe images are shown to highlight the cluster configurations [left column Fig. 3.11]. Strain energies from the Keating-like parameterization of the Si system from Lee and Hwang [18,19] were used to gradient-shade the profiles using a color spectrum that shifts from white to yellow to orange to red (WYOR) as E_{strain} increases [middle column Fig. 3.11]. Strain profiles based on average bond length [right column Fig. 3.11] are easy to construct for a FC system. The color spectrum in these profiles shifts from red to white to blue (RWB) as the average bond lengths shift from compressive to strain-free to tensile. The RWB spectrum covers the Si-Si DFT equilibrium bond length of 2.36 ± 0.07 Å. The E_{strain} profiles are useful to identify locations that have the highest magnitude of strain, while the profiles based on average bond length are convenient to assess the sign of strain present (compressive/tensile). To facilitate comparison among clusters, the color spectrums are effectively normalized for E_{strain} and average bond length, respectively, across all three clusters.

In a normalized context, the E_{strain} profiles qualitatively indicate that the most strained atoms among the three clusters are in I_3^g [Fig. 3.11(b)] because two of the atoms

are red. Referring to Fig. 2.4(a), these are atoms labeled "9" and "2" and they both have E_{strain} = 0.66 eV. Recall that the orientation of the I_3^g 9-2 bond with respect to the plane of strain corresponds to the orientation-dependent $E_f(3,\varepsilon)$ response. For comparison, the maximum values of E_{strain} are 0.47 eV and 0.31 eV for the $I_3^{4\%c}$ and I_4 clusters, respectively. The well-known local $E_f(4,0\%)$ minima [57,58] of I_4 relative to other small clusters is likely attributable to the success of the I_4 configuration in E_{strain} minimization. From symmetry, the strain-free maxima of E_{strain} for I_4 are seen at both atom 2 and atom 13. For $I_3^{4\%c}$, the strain-free maxima of E_{strain} are seen simultaneously at these atoms: 3, 4, 5, and 8. Considering the profiles based on average bond length, additional qualitative information can be ascertained about the local environment surrounding each cluster. The interior regions of all I_n are highly compressive (red), but much of the immediate cluster interface with bulk Si is under net tensile strain (blue). These 256+n supercells employed would need to be enlarged significantly in both [110] and $[1\bar{1}0]$ directions to comment further on the anisotropic nature of the localized tensile strain field generated around each interstitial configuration.

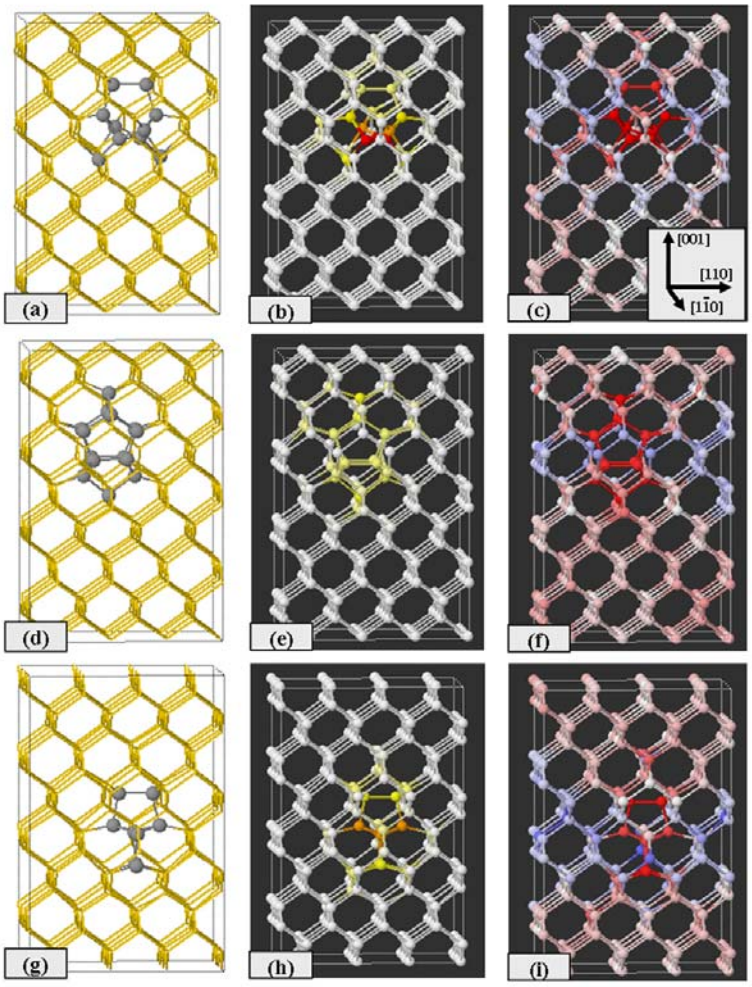

Figure 3.11: (Color available) Atomic-level strain distribution profiles shown for strain-free configurations of I_3^{gA}, I_4^{A}, and $I_3^{4\%c,A}$. The subfigures of the left column highlight each configuration embedded inside 256-atom supercells. Light gray (gold) wireframe represents bulk Si atoms in the lattice. Dark gray spheres represent the interstitial atoms and their highly strained neighbors. The images in the central column are strain profiles based on E_{strain}. Gradient-shading is effectively normalized for all strain profiles shown by calibrating the color spectrum to span all values observed across all structures. For the E_{strain} profiles of the central column, the color spectrum shifts from white to yellow to orange to red (WYOR) as E_{strain} increases from zero to 0.66 eV. The subfigures of the right column are based on average bond length. Each atom is assigned an average bond length based on the four bonds formed with its nearest neighbors and is gradient-shaded accordingly. The color spectrum shifts from red to white to blue (RWB) as the average bond lengths shift from compressive to strain-free to tensile. The RWB spectrum used covers the Si-Si DFT equilibrium bond length of 2.36 ± 0.07 Å.

3.7 Electronic Structure

Electronic structure characterization of small I_n is provided from evaluation of the total DOS (TDOS) of selected clusters under strain-free conditions. In particular, the FC configurations of I_3^g, $I_3^{4\%c}$, and I_4 are expected to be less likely than clusters with dangling bonds to introduce new states in the Si band gap, which is generally detrimental to electrical device performance. Figure 3.12 summarizes the TDOS results obtained. Each subfigure in Fig. 3.12 compares the TDOS for bulk Si relative to various embedded I_n. In Fig. 3.12(a), the presence of the split-<110> configuration introduces a large concentration of states in the band gap near the conduction band minimum (CBM). For I_2, the band gap (E_g) is significantly narrowed relative to bulk Si and the number of states just below the valence band maximum (VBM) is also decreased. For I_3^g, the TDOS closely resembles that of bulk Si and E_g is relatively unchanged as well. The I_3^{com} structure exhibits similar departures from the bulk Si TDOS as seen for I_2, including E_g reduction relative to bulk Si. $I_3^{4\%c}$ shows a modest band gap reduction and an increase in states just below VBM. For I_4, some E_g reduction is observed; otherwise, the TDOS for I_4 in and around the band gap resembles bulk Si. Note that no significant orientation effect was seen for I_4 in terms of TDOS, as expected. The reduction in E_g, even for the FC structure of I_4, is consistent with the introductory proposal of the D_{2d} configuration of I_4 by Arai *et al*. [34] In that work, they generalize that significant distortions in the Si-Si bond length can introduce localized states just inside the bulk E_g, even in the absence of dangling bonds. In summary, these results confirm that FC clusters (I_3^g, $I_3^{4\%c}$, I_4) generally exhibit less departure in TDOS from that of bulk Si relative to clusters that do not contain FC bond topologies (split-<110>, I_2, I_3^{com}).

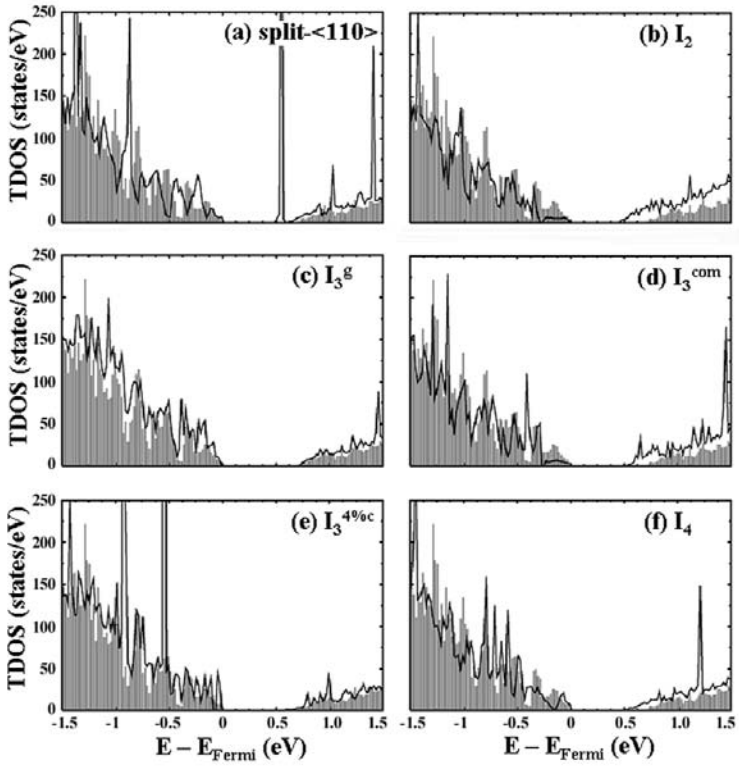

Figure 3.12: TDOS near the Si band gap for various small interstitial clusters (black) using strain-free 256+*n* supercells with reference to a 256-atom bulk Si supercell (gray background). Each different structure references its own calculated Fermi level so that all cases have VBM set to zero.

3.8 Summary

In this chapter, the energetic stability of neutral compact interstitial clusters (I_n, $n \leq 4$) was investigated using first-principles DFT calculations for various orientations and configurations under different uniform strain conditions. Cluster sizes $n \leq 4$ were selected for their expected role in the formation of larger clusters. The results of this biaxial and uniaxial strain condition investigation reveal that the minimum energy orientation and/or configuration is a function of the strain conditions present in the system. While this effort includes results from simulated conditions that are relatively extreme ($|\varepsilon| \geq 1$) for conventional strained CMOS processes, this exploration of

configuration changes and the impact of the orientation effect under strained conditions is of considerable scientific value for improved understanding of strained materials. For I_1, the tetrahedral structure becomes the minimum energy configuration for 4% compressive biaxial strain. The I_2 cluster undergoes a distortion in configuration at 4% compressive biaxial strain that lowers the expected E_f predicted by the ground-state configuration. Application of biaxial strain conditions during the I_n formation modeling process revealed a previously unreported configuration of I_3 ($I_3^{4\%c}$) with D_{2d} symmetry. The D_{2d} symmetry configurations of $I_3^{4\%c}$ and I_4 exhibit analogous E_f response behavior under uniaxial, biaxial, and hydrostatic strain conditions. $I_3^{4\%c}$ also shows a strong dual-response E_f behavior, like I_4, for the two relevant orientations under biaxial strain conditions. The $I_3^{4\%c}$ configuration is the only Si interstitial cluster investigated that is destabilized as strain conditions become more tensile. Cluster energetic dependence on uniaxial strain is often similar, but less sensitive, to that seen under biaxial strain, but uniaxial strain conditions often break orientation-dependent degeneracies observed under biaxial conditions. I_n characterization is extended by providing atomic-level strain distribution profiles in FC systems using both calculated strain energies and strain based on average bond lengths to nearest neighbors. Finally, TDOS results are discussed that qualitatively confirm that I_n with fourfold-coordination generally introduce less changes in and around the Si band gap than clusters without complete FC bond topologies.

Chapter 4

Prediction of Periodic Self-Interstitial Cluster Chains Under Biaxial Strain

4.1 Introduction

In this chapter, the effect that biaxial strain has on the growth behavior of self-interstitial defect clusters is examined using first-principles calculations. In particular, the stable I_4 cluster can aggregate with other I_4 clusters to form conditionally-stable extended chains that are energetically more favorable than known configurations of the same size under sufficient strain conditions. The theoretical framework is intended to model a uniform biaxial strain field that might occur in a MOSFET <110>-aligned channel built on a Si (100) wafer orientation. Unless noted otherwise, "strain" in this chapter refers to biaxial strain on Si (100). Most of the work in this chapter was previously published [72].

4.2 Computational Details

The DFT computational aspects in this chapter are identical to those previously described in Section 3.2. The larger clusters studied in this chapter necessitate larger supercells to inhibit interactions with periodic images (*vide infra* Fig. 4.2 for cluster-specific supercell sizes). Formation energies were evaluated to compute relative stability in the same fashion as discussed in Chapter 3.

4.3 Relevant Orientations of Ground-State and I_4 Chain Configurations

The structural details of the I_4 Si self-interstitial cluster were discussed in detail in Chapters 2 and 3. The $E_f(4,\varepsilon)$ dependence of I_4 on biaxial strain is determined by the

orientation of I_4 with respect to the biaxial strain field as shown in Fig. 3.4(c) [the $E_f(8,\varepsilon)$ response of I_8 is nearly identical in Fig. 3.4(d)]. Motivated by this interesting behavior observed for I_4 core derivative configurations, an effort was made to search for a potential family of extended configurations composed of I_4 core units using the integrated atomistic modeling procedure [18,19] under strained conditions. Starting with the I_8 ground-state configuration [19], four Si interstitials were added in the vicinity and a conditionally-stable I_{12} structure was discovered as depicted in Figs. 4.1(c) and 4.1(d).

In the previous work of Lee and Hwang [19], theoretical support was given to delineate Si self-interstitial clustering into three competing regimes based on approximate size and configuration: (1) compact clusters largely based on I_4 derivatives ($n \leq 10$), (2) extended transition configurations ($10 \leq n \leq 20$), and (3) defects containing {311} structural cores ($n \geq 20$). In addition, this previous work [19] also identified a configuration family based on the ground-state configuration of I_{12} with C_{2h} symmetry that is shown to collectively interrelate the most favorable configurations in the transition regime ($10 \leq n \leq 20$).

Figure 4.1 shows the two relevant orientations [64] ("A" and "B") under biaxial strain of both the I_{12} ground-state and I_4-chain configurations. In this chapter, I_{16} structures are also considered that are extensions of the I_{12} structures of Fig. 4.1. I_{16}^{A} with C_{2h} symmetry is made by extending I_{12}^{A} along [110] with a 4-atom core repeating unit added to the periodic architecture, while $(I_4)_4^{A}$ is made by adding an additional I_4 core to $(I_4)_3^{A}$ along $[1\bar{1}0]$ as seen in Fig. 4.1. While the repeating unit is comprised of four interstitials for both extended transition configurations, note that the repeating unit itself is a different configuration in each case. In order to emphasize the intraconfigurational composition of I_4 cores, the I_4-chain configurations will be designated as $(I_4)_m$, where m represents the number of I_4 cores in the chain. Similarly, the

I_{12} and I_{16} ground-state configurations will be collectively designated as "I_{12}-like" in the following discussion.

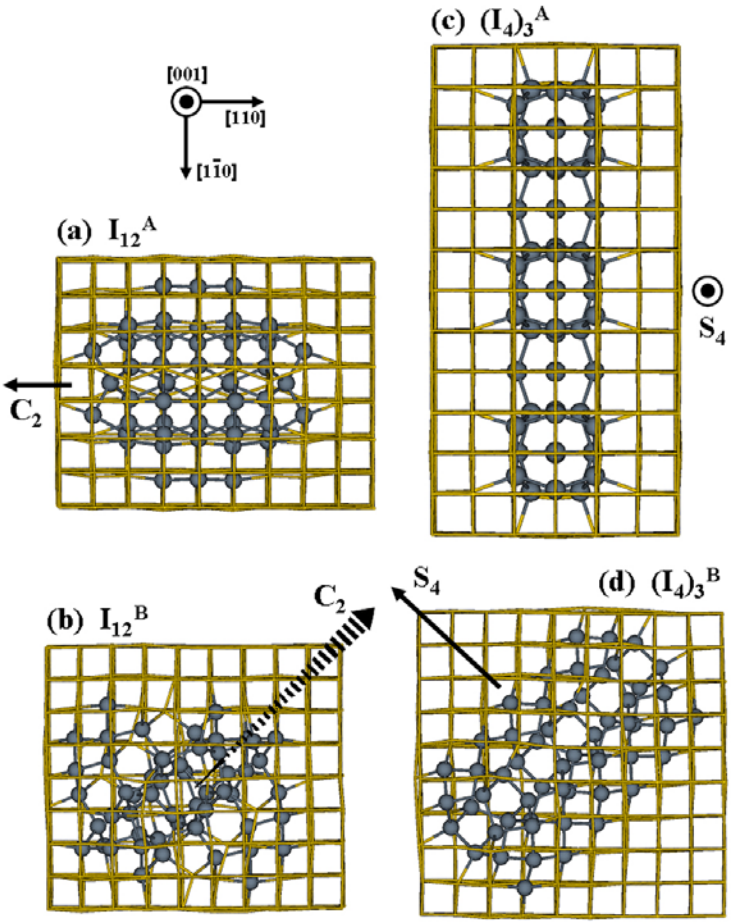

Figure 4.1: (Color available) Various embedded configurations and orientations of I_{12} as viewed along [001]. Light gray (gold) wireframe represents the bulk Si lattice. Dark gray spheres denote interstitials and their highly strained neighbors. For I_{12}^A (a) and I_{12}^B (b), the C_2 axis is shown for each orientation of the ground-state configuration with C_{2h} symmetry. For I_{12}^B, the C_2 axis traces a diagonal path through the supercell interior and emerges from the page at a 45º angle. For $(I_4)_3^A$ (c) and $(I_4)_3^B$ (d), the S_4 axis of an individual I_4 core is shown for each I_4-chain configuration.

4.4 Relative Stability of Ground-State and I_4 Chain Configurations

Figure 4.2 presents DFT-calculated $E_f(n,\varepsilon)$ data as a function of strain for the relevant orientations of the I_{12}-like and $(I_4)_m$ configurations of both I_{12} and I_{16}. The I_{12}-

like configurations exhibit a mild orientation-dependent $E_f(n,\varepsilon)$ response to strain, which is typical behavior for clusters containing significant quantities of split-<110>-like bonds in their interiors. For the "A" orientations of the I_{12}-like configurations, less sensitivity is seen in the $E_f(n,\varepsilon)$ responses to strain relative to the "B" orientations. In analogy with I_4 and I_8, the "A" orientations of the $(I_4)_m$ configurations show nearly invariant $E_f(n,\varepsilon)$ strain responses for both $(I_4)_3$ and $(I_4)_4$, while the corresponding "B" orientations show strong $E_f(n,\varepsilon)$ dependence on strain conditions. The main difference in the I_{12}-like results between the n=12 case [Fig. 4.2(a)] and the n=16 case [Fig. 4.2(b)] is simply the strain-free $E_f(n,\varepsilon)$ values [$E_f(n,0)$=1.63 eV (I_{12}) and $E_f(n,0)$=1.52 eV (I_{16})]; in contrast, the $E_f(n,0)$ values for $(I_4)_3$ and $(I_4)_4$ only differ by 10 meV. For both the I_{12}-like and $(I_4)_m$ configurations, the slopes of the $E_f(n,\varepsilon)$ responses as a function of strain are strictly dependent on their respective orientations, not cluster sizes.

It is apparent in Fig. 4.2 that the $(I_4)_m$ configurations can be energetically favorable in the compact-to-extended transition regime of interstitial cluster growth when strain conditions are present. Using I_{12} as an example [Fig. 4.2(a)], these results suggest that the preferred configuration/orientation for twelve Si interstitials under biaxial strain ($-4\% \le \varepsilon \le 4\%$) could proceed as follows: (1) $(I_4)_3^A$ for high compression ($-4\% \le \varepsilon \le -1\%$), (2) I_{12}^A for low compression ($-1\% \le \varepsilon \le 0\%$), (3) I_{12}^B for low tension ($0\% \le \varepsilon \le 2\%$), and (4) $(I_4)_3^B$ for high tension ($2\% \le \varepsilon \le 4\%$). Most importantly, the $(I_4)_m$ configuration appears to be the most favorable configuration for the n=12 and n=16 cluster sizes when the magnitude of biaxial strain is large. Furthermore, the orientation-dependent strain response associated with the D_{2d} symmetry of the I_4 core makes the $(I_4)_m$ configuration energetically preferable under both highly compressive and highly tensile conditions – the sign of biaxial strain will determine the prevalent orientation of $(I_4)_m$. The energy gain (ΔE) of the $(I_4)_m$ configurations over the I_{12}-like configurations is larger

under compression than for tension. Speculation on the trends observed for n=12 and n=16 suggests that minimum energy configurations for larger clusters (n > 20) may trend toward the stable configurations experimentally observed in {311} extended defects. Nevertheless, these theoretical results suggest that the $(I_4)_m$ configuration can be prevalent in the compact-to-extended transition regime depending on the cluster size (n) and the magnitude of biaxial strain present.

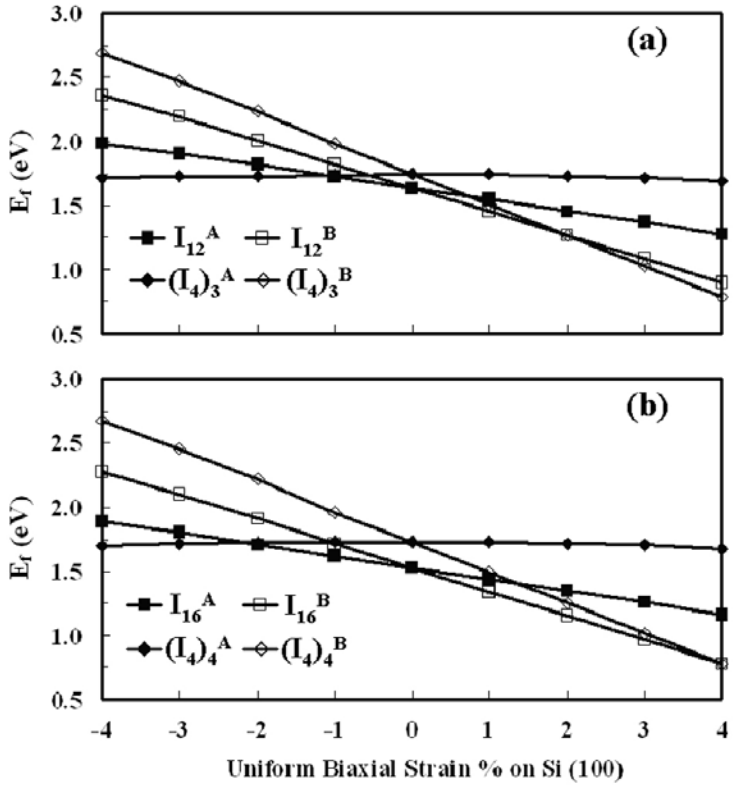

Figure 4.2: Formation energy response per interstitial for various configurations and orientations of I_{12} (a) and I_{16} (b) clusters as a function of strain. The elongated shapes of some clusters prompted employment of specialized supercell sizes as follows: 480+n [I_{12}^A, I_{12}^B], 576+n [$(I_4)_3^B$], 640+n [$(I_4)_3^A$], 672+n [I_{16}^A, I_{16}^B], 800+n [$(I_4)_4^A$], and 840+n [$(I_4)_4^B$].

4.5 Summary

In summary, the discussed results show that the stable I_4 core can aggregate with other I_4 cores along <110> to form short extended defect chains [$(I_4)_m$, m=3,4] that become more favorable than ground-state I_{12}-like configurations under sufficient biaxial strain conditions. The prevalent orientations that both $(I_4)_m$ and I_{12}-like elongated configurations will adopt depend on the nature (tensile/compressive) of biaxial strain present, but the larger difference in orientation-dependent relative stability in the $(I_4)_m$ configurations is the main reason that these configurations are preferable under certain strain conditions. These results suggest that the $(I_4)_m$ configurations may participate in the compact-to-extended transition regime ($10 \leq n \leq 20$) of self-interstitial cluster growth under sufficient strain conditions.

Chapter 5

Strain Effects on Si Vacancy Clusters (V_n)

5.1 Introduction

Like interstitials, vacancies are fundamental native defects that are ubiquitous to all crystalline materials and consequently of technological significance in semiconductor manufacturing because defects and impurities influence the electrical, optical, and mechanical properties of the host crystal. In particular, vacancies can be beneficial when adjacent to active electronic device regions by acting as gettering centers for impurities and through annihilation of self-interstitial defects; in contrast, vacancy clusters pinned inside active regions can be equally detrimental through impurity gettering and highly-strained clusters can create deep-level traps that interfere with charge transport and degrade threshold voltages. During the production of *c*-Si, Czochralski-grown Si pulled from a liquid melt inherently contains grown-in vacancies and small voids [73-75]. High-energy irradiation using electron, neutron, and proton bombardment as well as mechanical plastic deformation can also introduce vacancies into Si [76]. In addition, many semiconductor manufacturing processes introduce vacancies including etching, thermal oxidation, thin film deposition, and especially ion implantation [77]. Postimplantation annealing at elevated temperatures is further responsible for exacerbating vacancy agglomeration.

A variety of experimental techniques have been used to study vacancy clusters in Si, but a thorough understanding of vacancy behavior has thus far remained elusive. Positron annihilation spectroscopy is widely referenced [73,76,78,79], but spectroscopic

techniques, in general, cannot provide the structural configuration of small clusters. Transmission electron microscopy (TEM) was used to substantiate the existence of small voids on the scale of a few nanometers [80], but further resolution is needed to observe small clusters. In addition, FC vacancy clusters are thought to be transparent to electrical methods like deep-level transient spectroscopy (DLTS) and optical techniques like photoluminescence (PL) [78].

A complementary theoretical effort [20,21,74,76-79,81-85] has been made to support the experimental characterization of vacancies in Si. Many computational endeavors have sought to identify the minimum-energy configurations of small vacancy clusters, but most lacked a systematic method to search all complex, fully-coordinated configurations to determine the most favorable structures. Some early studies [77-79,82] focused on the ring hexavacancy (V_6) because of the exceptional stability suggested by its simple and complete FC configuration. Many of these same studies [77-79] concluded that partial hexagonal ring (PHR) configurations, which are formed by sequential removal of constituent Si ring atoms, would also represent the ground-state configurations of small vacancy clusters for $n < 6$, where n is the number of vacancies. Based on DFT calculations, Makhov and Lewis [76] proposed that small vacancy clusters (V_n, $3 \leq n \leq 5$) should favor complete fourfold coordination by nullifying all dangling bonds created by Si lattice atom removal via structural relaxation. The integrated atomistic modeling procedure of Lee and Hwang [18-22] was recently extended to identify much larger, neutral FC configurations (V_n, $3 \leq n \leq 48$) and these studies indicate that FC structures are preferable to PHR-type configurations across this size regime [20,21]. Thus far, virtually all theoretical studies on vacancies in the literature focus on unstrained Si. A recent study [83] using kinetic Monte Carlo (KMC) simulations investigates the anisotropic nature of vacancy behavior in uniaxially-strained Si, but most

conclusions concern vacancy-vacancy interactions, rather than cluster formation and structure.

In this chapter, the effect of uniform strain fields on the stability, structure, and orientation of small, neutral Si vacancy clusters (V_n, $n \leq 12$) on both biaxially- and uniaxially-strained Si (100) is investigated. Such small V_n on the subnanometer scale justify approximation of the applied strain fields to be effectively uniform in the immediate locale of the clusters. The first-principles calculations presented simulate a bulk *c*-Si environment that might occur in the middle of a MOSFET transistor with a <110>-aligned channel. The generation of all FC clusters studied was achieved using the integrated atomistic modeling procedure of Lee and Hwang [18-22]. The results discussed here provide an important step in the elucidation of vacancy behavior under strain, which is also essential to understanding related native defect phenomena including vacancy agglomeration, self-interstitial annihilation, and stability near interfaces. Furthermore, these results highlight the influence of strain on the relative stability of FC and PHR-type clusters, the critical effect of cluster orientation on relative stability in anisotropic environments, and the propensity of strain to augment ground-state configurations. The majority of the work presented in this chapter was previously published [86].

5.2 Computational Details

The optimized atomic structures and energies reported in this chapter were computed using a planewave basis set pseudopotential method within the generalized gradient approximation of Perdew and Wang (GGA-PW91) [11] to DFT [66], as implemented in VASP [10]. Vanderbilt-type US-PPs [13] were used to represent interactions between ion cores and valence electrons. Wavefunctions were expanded using a planewave basis set with a kinetic-energy cut-off of 160 eV. BZ sampling was

performed with one k-point (Γ) for optimization of atomic structures. Geometric optimization allowed all atoms to relax until residual forces between atoms had converged within 5×10^{-2} eV/Å tolerance. With optimized ionic positions determined, corresponding total energies were refined using a 2×2×2 Monkhorst-Pack grid. For the strain-free Si supercell, an optimized lattice constant of 5.457 Å along <100> or 3.859 Å along <110> was employed.

5.3 Comparison of Fixed Cell and Volume Relaxation Approaches

To evaluate biaxial and uniaxial strain conditions, a basis set of lattice vectors associated with a four-atom supercell was computed for each strain condition ($-4\% \leq \varepsilon \leq 4\%$) and scaled up to each supercell size investigated. In this chapter, small vacancy clusters ($n \leq 3$) utilize 256-atom supercells, while all larger vacancy clusters use 480-atom supercells. For both basis supercells, the same cell dimensions are applied to the vacancy-containing supercells as calculated for the bulk Si reference supercells. Using this fixed cell approach instead of a volume relaxation strategy is not only more representative of an isolated vacancy cluster in uniformly-strained bulk Si, but also simplifies the calculations by allowing for a fixed set of dimensions to represent applied strain conditions for all cases of a given supercell size. Preliminary calculations were conducted that justify this fixed cell approach in lieu of cluster-specific volume relaxation as long as the supercell chosen is sufficiently large for each cluster. For the smallest(largest) cluster studied in the 480-atom supercell, $V_4(V_{12})$, volume relaxation is found to decrease the strain-free lattice constant by 0.2(0.6) %, while the strain-free formation energy decreases by 0.002(0.05) eV per vacancy. While the percent change in lattice constant from volume relaxation is non-negligible for the largest clusters in terms of the applied strain conditions ($-4\% \leq \varepsilon \leq 4\%$), this should not change the trends reported nor alter the conclusions of this study. To fully circumvent this size effect issue,

supercells containing many thousands of atoms are required because the local strain fields generated by FC clusters can be spatially extensive.

Since the effect of volume relaxation on strain-free V_n is larger on the lattice constants relative to the formation energies, manifestation of this correction in formation energy as function of strain throughout these reported results is largely a shift (left/right) of the formation energy curve on the order of ~0.1%. Volume relaxation on a vacancy cluster always reduces the supercell volume relative to bulk Si, so the formation energy curves as a function of strain will always shift to the right (slightly tensile), if this correction is applied. Sample calculations suggest that the correction magnitude obtained from volume relaxation tends to increase as the strain conditions become more compressive. Note that the relationship between lattice constant and applied strain is only one-to-one in the simple hydrostatic case; however, the relationship between a correction in lattice constant from volume relaxation and either a biaxial or uniaxial strain scenario is more complex. In fact, computing a formation energy correction for biaxially- or uniaxially-strained vacancy clusters would necessarily depend on the supercell size (N), cluster size (n), and sign/magnitude of strain (ε).

5.4 Ground-State Cluster Stability Under Strain

Lee and Hwang [20] reported configurations of FC vacancy clusters (V_n, $3 \leq n \leq 18$) identified using an integrated atomistic modeling procedure [18-22] combining Metropolis Monte Carlo (MMC), tight-binding molecular dynamics (TBMD), and DFT calculations. Figure 5.1 shows a subset of these same ground-state vacancy clusters (V_n, $3 \leq n \leq 12$) along with the fundamental mono- and divacancy clusters. These structures are the foundation for the strain investigation of vacancy clusters. As a consequence of the complex structure of many FC configurations, clusters are illustrated largely through identification of the highly-strained atoms neighboring the vacant atoms, rather than

representing vacant sites with visual identifiers that are often used to illustrate PHR-type clusters. Unless noted otherwise, a reference to V_n throughout this chapter refers to the specific orientation and configuration of a cluster as shown in Fig. 5.1.

In Chapter 3, the orientation-dependent stability for various interstitial cluster (I_n) configurations was detailed on Si (100) under both uniaxial and biaxial strain conditions. For vacancy clusters in strained Si, cluster formation energies are also highly dependent on the cluster orientations with respect to the strain field. In concert with Chapter 3, a similar orientation nomenclature will be adopted for V_n as defined for I_n to harmonize presentation of simulation results. The clusters shown in Fig. 5.1 represent the "A" orientation of each configuration; unless noted otherwise, a cluster without an explicit orientation label is the "A" orientation in Fig. 5.1. Note that the "A" orientation is essentially an arbitrary designation of the original cluster orientation. In special cases where multiple V_n are compared with identical symmetries, orientation labels have been synchronized within the group to enhance clarity and facilitate discussion. The "B" orientation, which will only be studied under biaxial strain for this vacancy study, is formed by rotating a configuration in Fig. 5.1 so that an abstract axis aligned with [001] (out-of-plane) becomes aligned with either [100] or [010] (in-plane directions). The "C" orientation, which is only relevant for uniaxial strain in this vacancy study, is simply a 90° rotation of a configuration about an axis aligned with [001]. As depicted in Fig. 2.3, uniaxial strain is always applied along [110] throughout this chapter. Further background on the orientation framework for native defect clusters in crystalline Si was previously described in Chapter 2.

To quantify the relative stability of Si vacancy clusters, formation energies dependent on both cluster size (n) and strain condition (ε) are calculated as follows:

$$E_f(n,\varepsilon) = E_{tot}(n,\varepsilon) - \frac{N-n}{N} E_{bulk}(\varepsilon), \tag{5.1}$$

where $E_{tot}(n, \varepsilon)$ is the total energy of the V_n cluster in the N-n atom supercell, n is the size of the vacancy cluster, N is the basis number of atoms in the bulk Si supercell, and $E_{bulk}(\varepsilon)$ is the total energy of the N-atom supercell of c-Si at a given strain condition. Formation energies are frequently reported on a per vacancy basis; to ensure clarity in these results, formation energies will be labeled using $E_f(n,\varepsilon) = n\hat{E}_f(n,\varepsilon)$ in this chapter, where $\hat{E}_f(n,\varepsilon)$ is formation energy on a per vacancy basis.

Figure 5.2 characterizes the general stability trend of the ground-state clusters of Fig. 5.1 under biaxial strain conditions. Unlike the I_n trend previously shown in Chapter 3 and published in Ref. 64, Fig. 5.2 was generated by only evaluating the strain-free, minimum-energy configuration at each n for the orientations shown in Fig. 5.1. To emphasize this distinction, formation energy differences (ΔE_f) are provided relative to the strain-free $E_f(n,\varepsilon)$ at various discrete strain conditions. In general, the formation energies tend to increase with increasing cluster size under increasingly tensile strain conditions, while the formation energies tend to decrease with increasing cluster size under increasingly compressive strain conditions. The variety of different configurations and cluster symmetries [Fig. 5.1] are considered largely responsible for abrupt cluster-to-cluster variations in $\Delta E_f(n,\varepsilon)$ as n increases. This cluster-to-cluster variation is not surprising since Lee and Hwang [20] show a similar non-monotonic trend for $\hat{E}_f(n)$ for FC clusters under strain-free conditions. As expected, compressive strain tends to stabilize V_n, just as tensile strain was shown in Chapter 3 to stabilize I_n. This result is intuitive since compressive strain tends to reduce the large interatomic distances for atoms neighboring voids in the crystal lattice.

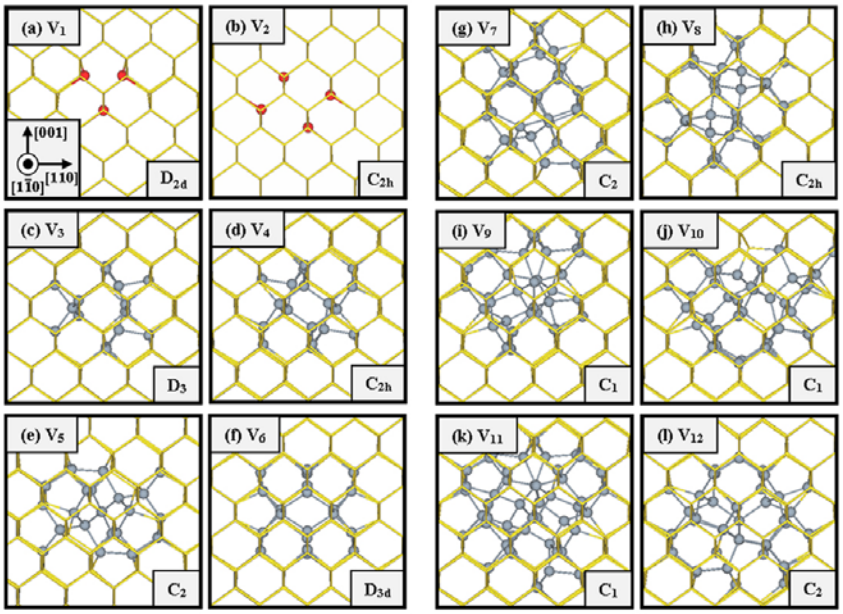

Figure 5.1: (Color available) Strain-free, ground-state configurations of small, neutral vacancy clusters (V_n, $n \leq 12$) with corresponding cluster symmetries annotated. The perspectives shown for all clusters are defined to be the initial "A" orientations to facilitate discussion. Light gray (gold) wireframe represents bulk *c*-Si. Dark gray spheres represent highly strained atoms neighboring the V_n and red spheres represent atoms with dangling bonds. All structures are FC configurations except V_1 and V_2.

To illustrate how application of a formation energy correction based on volume relaxation might adjust the trends in Fig. 5.2, a variable shadow has been drawn adjacent to each line based on sample volume relaxations of strain-free V_4 and V_{12} interpolated to other V_n and extrapolated to other strain conditions. The anticipated correction increases with n within each supercell size ($n \leq 3$, N=256; $n \geq 4$, N=480). The overall effect of the correction tends to shift all data in the tensile direction with respect to the strain-free reference because cluster-specific volume relaxation will compress each strain-free vacancy-containing supercell to some degree.

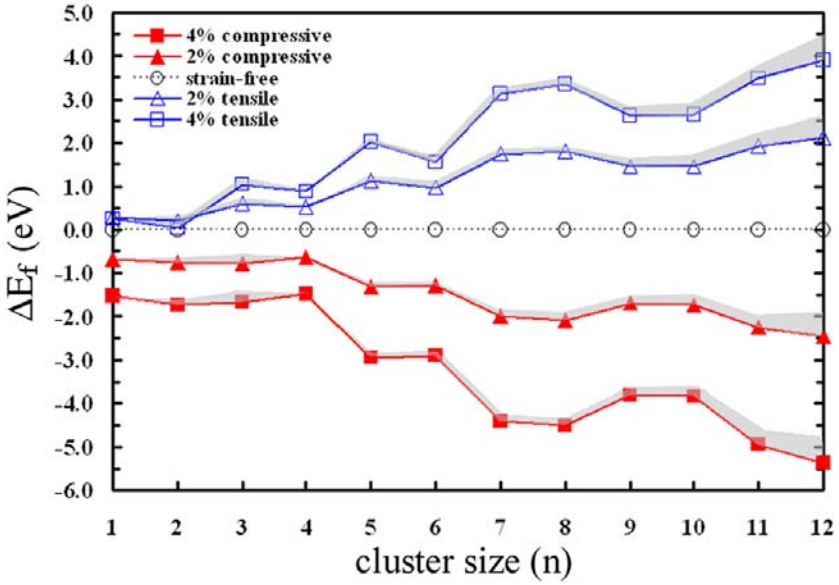

Figure 5.2: (Color available) Formation energy differences at discrete biaxial strain conditions for all ground-state vacancy cluster orientations in Fig. 5.1 relative to their respective strain-free conditions. Compressive conditions are denoted by solid polygons (red). Tensile conditions are denoted by open polygons (blue). Gray shadowing added to each trend provides an approximate magnitude of adjustment that might occur if a correction based on volume relaxation is applied.

Figure 5.3 shows the formation energy response curves as a function of strain for the minimum-energy configurations of V_1 through V_6. Since compression stabilizes V_n, the trends tend to have positive slopes, complementary to the negative slopes exhibited for I_n in Chapter 3. Consistent with previous results on I_n, the $\hat{E}_f(n,\varepsilon)$ response (slope) is generally more sensitive to biaxial strain relative to uniaxial strain. A prominent feature, particularly in the biaxial case [Fig. 5.3(b)], is the flat $\hat{E}_f(n,\varepsilon)$ response under tensile conditions for both the mono- and divacancy. This behavior is similar to the general observation of flatness in the total energy as a function of ionic coordinate [20,84]. The initial observation of the flatness of $\hat{E}_f(2,\varepsilon)$ for V_2^{PHR} [same configuration and orientation as V_2 in Fig. 5.1(b); PHR significance will be emphasized in Section 5.6] under uniaxial strain suggested a possible orientation effect like those previously described for

interstitials. This motivated further study and the inclusion of the "C" orientations for uniaxial strain of both V_2^{PHR} and V_6. Recall that the V_6 hexavacancy is a complete ring of vacancies in the Si lattice; while it exhibits strain-dependent behavior like PHR-type defects, it is also technically an FC structure. From Fig. 5.3(a), it is apparent that the "A" orientations of V_2 and V_6 are essentially insensitive to uniaxial strain, while the "C" orientations show more sensitivity to strain.

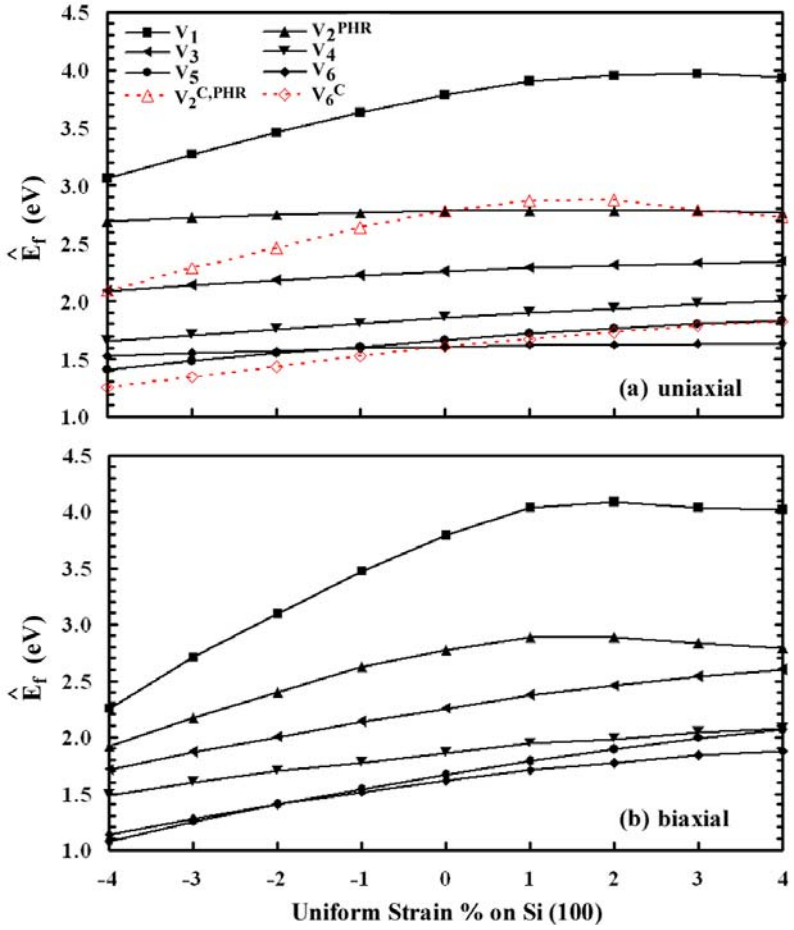

Figure 5.3: (Color available) Formation energy per vacancy for the ground-state vacancy cluster orientations in Fig. 5.1 (V_n, $n \leq 6$) as a function of (a) uniaxial strain and (b) biaxial strain. Tensile strain is defined to be positive. All configurations represented by solid (black) markers are in their initial "A" orientations, while the "C" orientations (only relevant for uniaxial strain) are represented by open (red) markers.

5.5 Orientation Effects Under Biaxial Strain

The phenomenon of orientation-dependent stability of I_n in uniform strain fields was a central feature in the work presented in Chapter 3. As a result of the time-consuming nature of generating and investigating relevant cluster orientations, only selected V_n were investigated based on their group symmetry classifications.

Interstitial clusters with C_{2h} symmetry, like I_{12} (Ref. 72), exhibit orientation-dependent behavior under biaxial strain. As a result, the C_{2h} configurations of V_4 [Fig. 5.1(d)] and V_8 [Fig. 5.1(h)] were likewise evaluated for a possible orientation effect. The "B" orientation counterparts of the Fig. 5.1 "A" orientations were generated. Figure 5.4 shows that V_4 and V_8 indeed exhibit orientation-dependent $\hat{E}_f(n,\varepsilon)$ behavior. As in the interstitial case, an orientation-dependent strain response corresponds to C_2 symmetry axis alignment relative to the plane of strain. Unlike the interstitial case, C_2 axis alignment with the plane of strain does not indicate how the sensitivity of $\hat{E}_f(n,\varepsilon)$ will change. For V_4^B, the slope of $\hat{E}_f(4,\varepsilon)$ increases relative to V_4^A, while the slope of $\hat{E}_f(8,\varepsilon)$ for V_8^B decreases relative to V_8^A.

As previously described for I_n, different V_n orientations also shift the qualifications of adequate supercell size to avoid periodic image effects. To circumvent the use of prohibitively large supercells, $\hat{E}_f(n,\varepsilon)$ are equated for all orientations at the strain-free ($\varepsilon = 0$) condition to reference the lowest strain-free $\hat{E}_f(n,\varepsilon)$ calculated. This same $\hat{E}_f(n,\varepsilon)$ correction was then applied to all strain conditions for a given vacancy configuration. This correction is only relevant where multiple orientations converge to a single $\hat{E}_f(n,\varepsilon)$ at the strain-free condition.

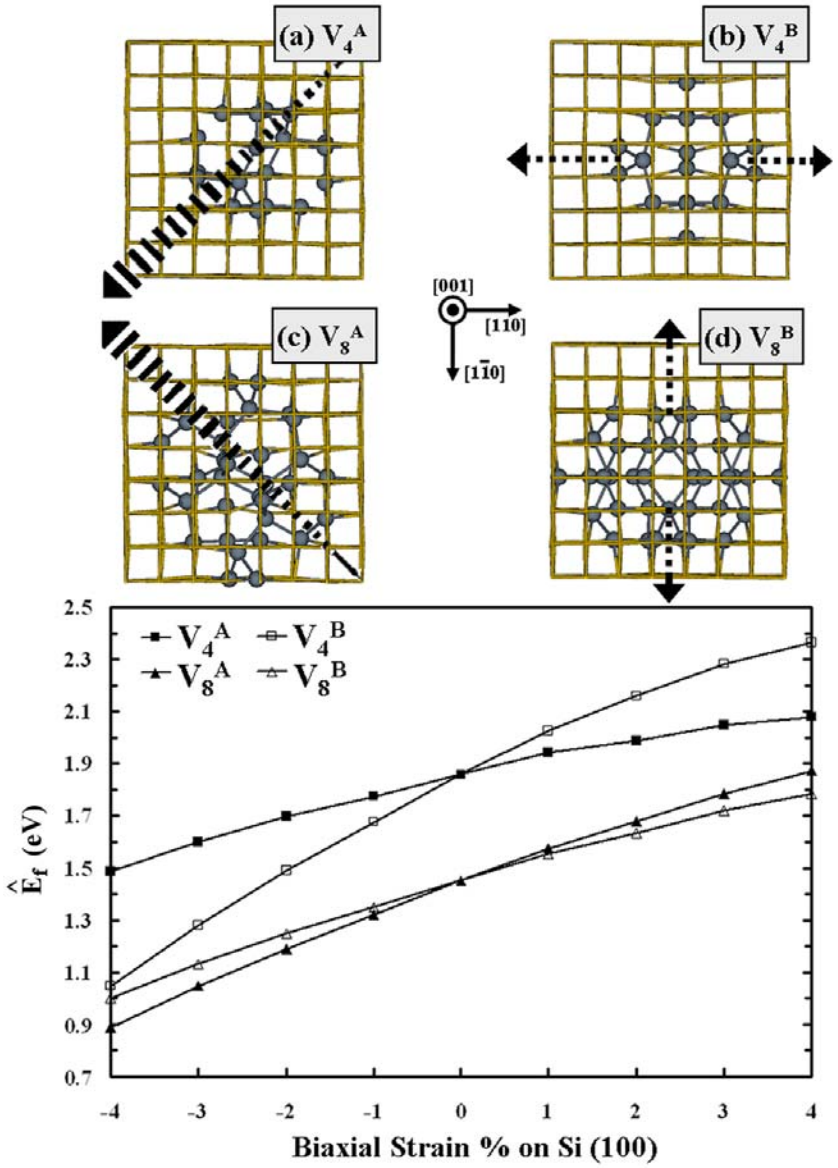

Figure 5.4: (Color available) Formation energy per vacancy as a function of biaxial strain for the two relevant orientations of the C_{2h} symmetry configurations of V_4 and V_8. The "A" orientations are depicted with solid polygons, while the "B" orientations are depicted by open polygons. The upper panel shows each orientation as viewed along [001] with corresponding C_2 symmetry axes indicated by black arrows. Light gray (gold) wireframe represents bulk *c*-Si. Dark gray spheres represent highly strained atoms neighboring the V_n. For the "A" orientations in (a) and (c), the C_2 axes trace a diagonal path through the supercell interior and emerge from the page at 45° angles, while the C_2 axes for (b) and (d) are contained in the plane of the page.

5.6 PHR and FC Relative Stability

An array of literature exists on the structure and stability of small vacancy clusters in Si. In particular, the work of Lee and Hwang [20] showed that FC vacancy clusters are thermodynamically favored over their PHR counterparts over the entire size range n = 3 to 18. While this observation holds in the strain-free case, the present work reveals that various strain conditions (sign, magnitude, and type of strain) and cluster orientations complicate identification of the most favorable configuration for an arbitrary cluster size.

5.6.1 Biaxial Strain

The plot in Fig. 5.5 presents a comparison of FC and PHR-type vacancy cluster ($3 \leq n \leq 5$) formation energy curves under biaxial strain. The FC structures are the ground-state configurations of Fig. 5.1, while the PHR-type configurations are introduced in the upper panel of Fig. 5.5. As previously described [20], V_5^{PHR} is actually an FC configuration proposed by Makhov and Lewis [76], but is 0.33 eV less favorable than the strain-free, ground-state FC V_5 structure. Since V_5^{PHR} is created through geometrical relaxation of a conventional partial ring structure (n = 5), this structure will be designated as V_5^{PHR} throughout the remainder of the chapter.

For each cluster size, it is evident that the ground-state FC structure is energetically more favorable than its corresponding PHR counterpart in the strain-free case. However, for large magnitudes of tensile biaxial strain ($\varepsilon \geq 2$), it is apparent that both V_3^{PHR} and V_5^{PHR} become more favorable than V_3 and V_5, respectively. This same behavior might also occur for the tetravacancy case, but the large difference in strain-free formation energies per vacancy [$\hat{E}_f(4,0\%)$ = 1.86 eV (V_4) and $\hat{E}_f(4,0\%)$ = 2.20 eV (V_4^{PHR})] prohibits V_4^{PHR} favorability in the range of strain investigated. From the formation energy curves in Fig. 5.5, it is apparent that the potential favorability of the PHR configurations in each case is made possible by the prominent flatness in the $\hat{E}_f(n,\varepsilon)$

curves under tensile strain. The flatness is much more apparent for structures with incomplete fourfold coordination, as for V_3^{PHR} and V_4^{PHR}, rather than the mild reduction in slope exhibited for V_5^{PHR} (FC). This observation is further supported upon review of Fig. 5.3(b) which shows a flat response under tensile strain for V_2^{PHR}, but only a subtle reduction in slope for the limiting PHR case of FC V_6.

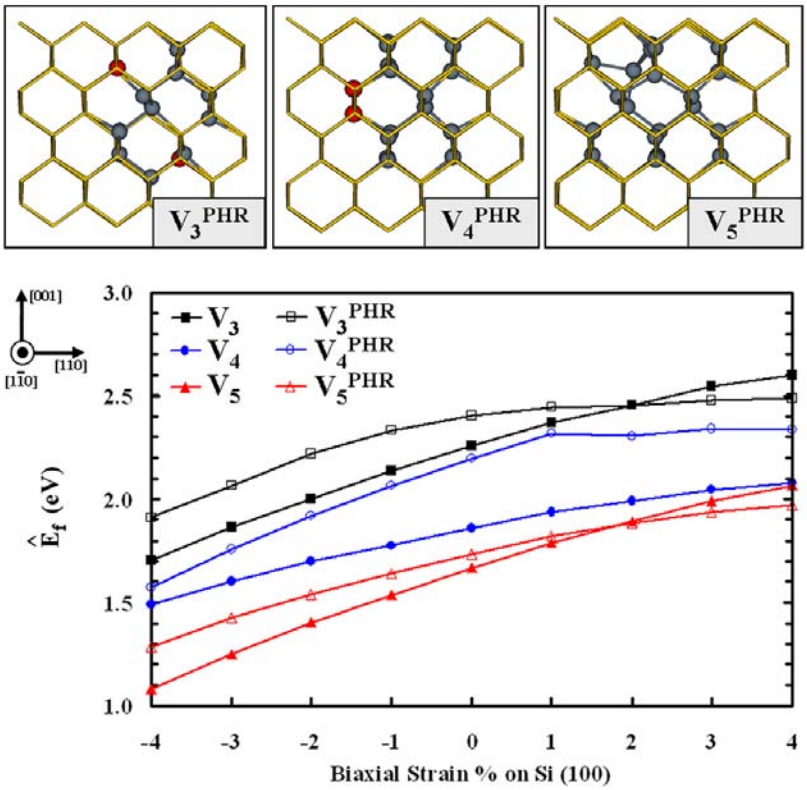

Figure 5.5: (Color available) Formation energy per vacancy as a function of biaxial strain for both ground-state (solid markers) and PHR-type (open markers) configurations for n = 3 to 5. The strain-free, ground-state FC structures are depicted in Fig. 5.1, while the upper panel shows the corresponding PHR-type configurations. Light gray (gold) wireframe represents bulk *c*-Si. Dark gray spheres represent highly strained atoms neighboring the vacancy clusters and red spheres represent atoms with dangling bonds.

5.6.2 Uniaxial Strain

Motivated by the orientation effect observed under uniaxial strain [Fig. 5.3(a)] for both V_2 and V_6, the current study proceeded to investigate other PHR-type clusters to confirm generality of this behavior. Figure 5.6 presents $\hat{E}_f(n,\varepsilon)$ curves as a function of uniaxial strain for both FC and PHR-type vacancy clusters in the size range $n = 2$ to 6. It is evident from these results that the "A" orientation of PHR-type defects is less sensitive to uniaxial strain than the "C" orientation. At first glance, the trivacancy case appears to offer the only exception; however, further inspection of the ring vacancy configuration in the upper left panel of Fig. 5.6 reveals that $V_3^{A,PHR}$ and $V_3^{C,PHR}$ are identical with respect to uniaxial strain. The "C" orientation of the ring structure in Fig. 5.6 shows that there are two unique bonding arrangements with respect to strain: (1) bonds 2-3 and 5-6 and (2) bonds 1-2, 1-6, 3-4, and 4-5. V_3^{PHR} is formed by removal of the atoms delimiting bonds 1-2 and 2-3, so V_3^{PHR} has one bond from each unique bond set. Therefore, conversion of $V_3^{A,PHR}$ to $V_3^{C,PHR}$ is irrelevant with respect to strain because there is still one bond representing each bonding set after reorientation. For all other PHR configurations in Fig. 5.6, the orientation change between "A" and "C" augments the bond count between the two bonding groups and an orientation effect is observed in the $\hat{E}_f(n,\varepsilon)$ data. The behavior of the strain-free, ground-state FC configurations ($3 \leq n \leq 5$) are also provided in both orientations for comparison. $V_5^{A,PHR}$ under high tension provides the only case identified where a PHR structure is predicted to be more stable ($\varepsilon \geq 3\%$) than the corresponding strain-free, ground-state FC structure.

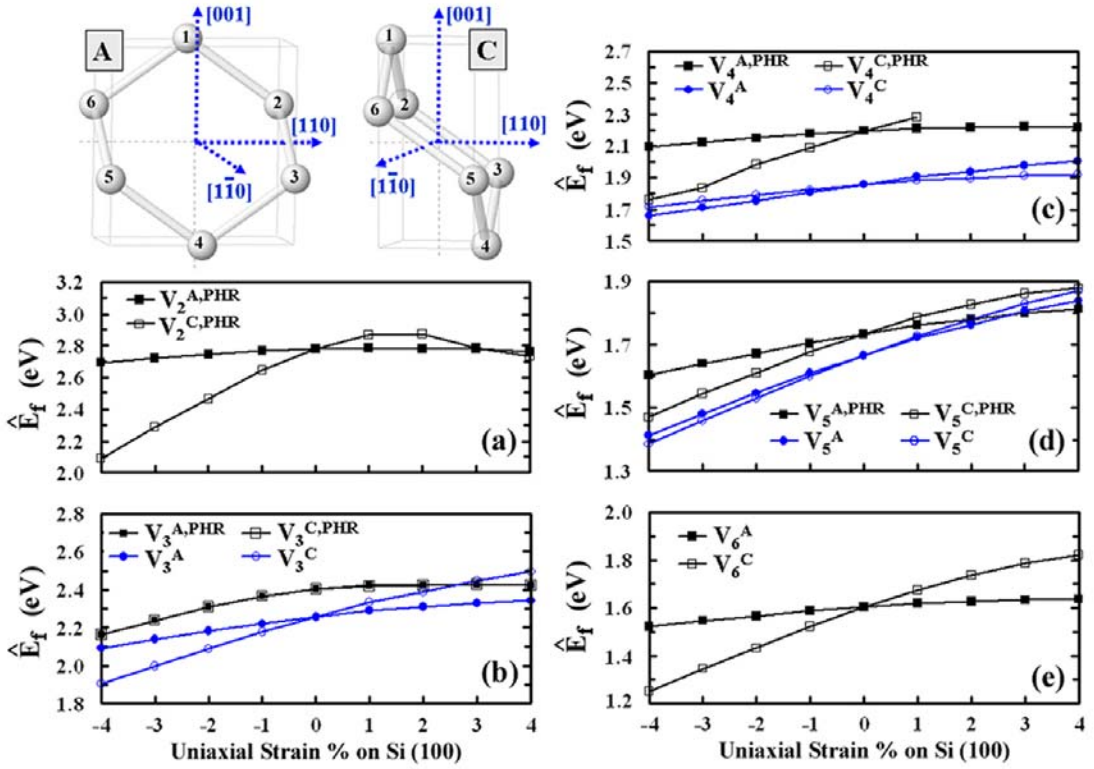

Figure 5.6: (Color available) Formation energy per vacancy as a function of uniaxial strain applied along [110] for each cluster size ($2 \leq n \leq 6$) for both FC and PHR configurations in both "A" and "C" orientations, as applicable. Square markers (black) represent PHR-type configurations, while circular markers (blue) represent FC configurations, where applicable. Solid markers represent "A" orientations, while open markers represent "C" orientations. The upper left panel is a visual aid for orientation of the general six-membered ring with respect to the Si lattice. The vacancy sites are numbered to facilitate discussion in the order in which atoms were removed to form PHR-type ring defects. In orientation "A", applied strain along [110] is parallel to an imaginary surface formed by the missing constituents of the ring. In orientation "C", the applied strain direction is rotated 90° about [001] and is orthogonal to these missing bonds: 1-2, 1-6, 3-4, and 4-5.

Another important aspect of these results is the data omitted in Fig. 5.6(c) for the $V_4^{C,PHR}$ $\hat{E}_f(4,\varepsilon)$ curve. In this case, sufficient tensile strain ($\varepsilon > 1\%$) was found to initiate configuration changes, so this data is not shown for the sake of clarity. Application of both 2% and 3% uniaxial strain to the strain-free configuration of $V_4^{C,PHR}$ generated an

unoptimized configuration with the same bond topology as the strain-free, ground-state FC V_4^C structure. This observation is significant since it suggests that strain can enable interconversion between PHR-type and FC vacancy structures. Finally, application of 4% uniaxial strain to the strain-free configuration of $V_4^{C,PHR}$ generated a different configuration deficient of complete fourfold coordination that is distinct from either the V_4 or V_4^{PHR} configurations.

5.7 Configuration Changes

As previously described, strain can initiate configuration changes in vacancy clusters, just as previous work [65,72] described both structural distortions and configuration changes for interstitial clusters in strained Si. To further this study, the integrated atomistic modeling procedure [18-22] was used to generate V_n configurations under both 3% compressive and 3% tensile biaxial strain conditions for cluster sizes up to $n = 12$. For the sake of brevity, only some highlights will be described from comparison of clusters formed strain-free to those formed under strain as motivation for future work. Overall, the vacancy clusters formed under tensile conditions provided more interesting results, particularly in terms of formation energy responses as a function of strain.

In Fig. 5.7, $\hat{E}_f(5,\varepsilon)$ behavior is provided as a function of strain for both the strain-free, ground-state FC V_5 configuration and a pentavacancy structure (V_5^t), also with fourfold coordination, formed under 3% tensile biaxial strain. In this case, formation energies are nearly degenerate under strain-free conditions [$\hat{E}_f(5,0\%) = 1.67$ eV (V_5) and $\hat{E}_f(5,0\%) = 1.65$ eV (V_5^t)]. As additional qualification of the approximate degeneracy of these structures, note that Ref. 20 generated V_5 as the ground-state configuration, while Ref. 21 generated V_5^t through annealing of $V_4+V \rightarrow V_5$ during TBMD simulations at 1400 K. These results indicate that the stability of V_5^t is less sensitive to strain than V_5 and that V_5^t is the preferred orientation under tensile conditions.

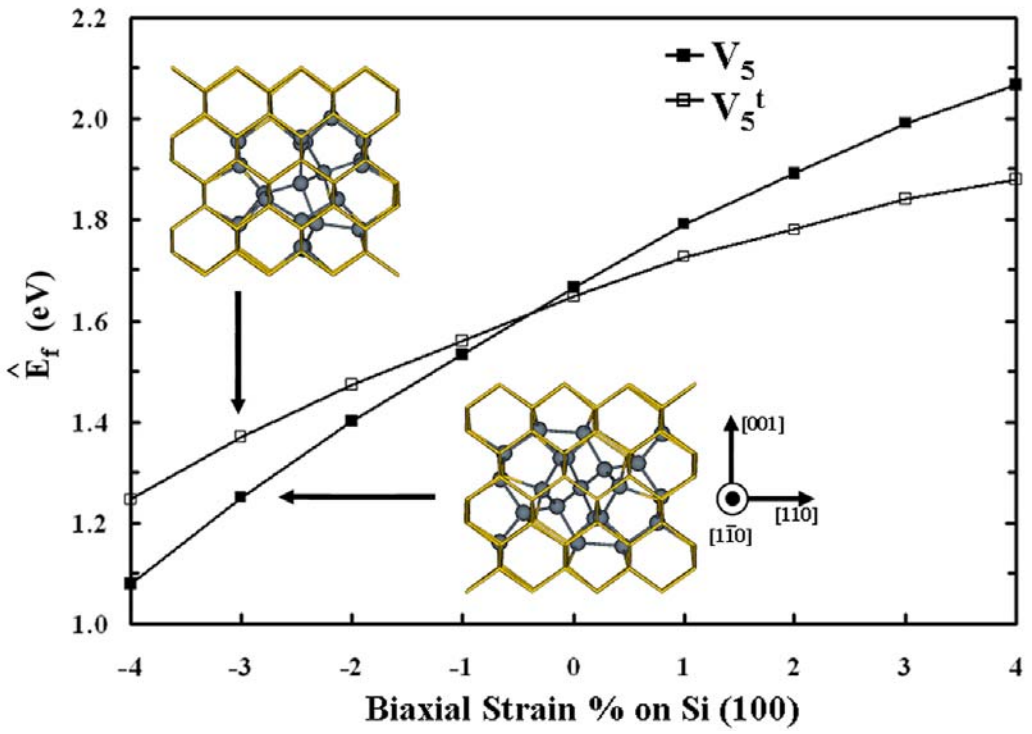

Figure 5.7: (Color available) Formation energies per vacancy as a function of biaxial strain for the strain-free, ground-state FC V_5 structure and a FC pentavacancy configuration (V_5^t) identified by formation under tensile biaxial strain conditions. These structures are approximately degenerate under strain-free conditions. Inset cluster configurations are shown along $[1\bar{1}0]$. Light gray (gold) wireframe represents bulk *c*-Si. Dark gray spheres represent highly strained atoms neighboring the V_n.

5.8 Summary

The effect of strain on the stability and structure of small, neutral Si vacancy clusters (V_n, $n \leq 12$) was investigated using periodic DFT calculations. The discussed results indicate that compressive strain generally stabilizes vacancy clusters, which is complementary to the conclusions of Chapter 3 that showed that tensile strain stabilizes Si interstitial clusters. The magnitude of stabilization provided by biaxial compression is

generally greater than the magnitude of stabilization observed under uniaxial compression.

Similar to previous work on interstitials, orientation effects are also observed for vacancy clusters in uniform strain fields. The C_{2h} symmetry configurations of V_4 and V_8 exhibit orientation-dependent behavior under biaxial strain in correlation with the orientation-dependent behavior shown by interstitial clusters with C_{2h} symmetry. This observation is significant because it emphasizes the critical role that cluster symmetry performs in orientation-dependent stabilization in strained Si, regardless of cluster composition.

The calculation results presented show that strain conditions can modulate the relative stability of competing FC and PHR-type configurations. While FC configurations are more favorable for small vacancy clusters in strain-free environments, PHR-type configurations become preferred under certain tensile conditions in both biaxial and uniaxial cases. The relative stabilization of PHR-type configurations under tension is largely attributable to the flat nature of the formation energy dependence on strain that is generally exhibited by clusters with incomplete fourfold coordination. In addition, these results illuminate a general orientation effect for PHR-type configurations ($2 \leq n \leq 6$) under uniaxial strain related to alignment of the parent ring structure with respect to the direction of applied strain.

Selected simulations also demonstrate that strain of sufficient magnitude can initiate configuration changes. An example (V_5^t) of a vacancy configuration identified by cluster formation under 3% tensile biaxial strain was presented. This particular structure was highlighted because it exhibits a different formation energy response as a function of strain when compared to its counterpart configuration (V_5) formed under strain-free conditions. This study furthers the understanding of Si vacancy clusters by providing

insight into the influence that strain has on the stability and structure of vacancy defects, which is an important step toward property prediction and ultimately defect engineering in Si-based materials.

Chapter 6

Property Predictions in Amorphous Si-based Materials

6.1 Introduction

The foundations for the use of amorphous semiconductors in photovoltaic and optoelectronic applications began in the 1960s when early work demonstrated that short-range order (SRO) sufficiently retained key optical properties present in crystalline semiconductors [87]. In an amorphous semiconductor, the disordered covalent network contains minor deviations in bond length and larger variations in bond angle relative to its counterpart crystalline lattice [88]. In the 1970s, Carlson and Wronski [89] reported the first feasible amorphous Si (*a*-Si) p-i-n solar cell using *a*-Si with radically-reduced gap defect densities attributed to H compensation of dangling bonds. Hydrogenated *a*-Si (*a*-Si:H) is remarkably promising for solar applications because the red-shifted absorption coefficient relative to *c*-Si could ultimately allow realization of inexpensive thin film (≤ 1 μm) solar cells if the light-induced degradation of the Staebler-Wronski effect [90] (SWE) is circumvented. Recent experimental work has shown that mixed-phase materials, such as nanocrystalline Si (*nc*-Si) dispersed in *a*-Si:H, can potentially mitigate the reversible SWE [91].

In recent years, nanostructure fabrication techniques have introduced the capability of growing *nc*-Si in Si-rich amorphous silicon oxide (*a*-SiO_x) matrices to produce flash memory [92] dielectrics and materials capable of light emission [93,94] via size-tunable photo- and electroluminescence processes. While many suggest light emission from *nc*-Si embedded in *a*-SiO_x is driven by quantum confinement, discrepancies in experimental results suggest other phenomena may also be influential,

such as sensitive chemical functional groups and oxide defects that may be stabilized at the *nc*-Si/*a*-SiO_x interface and size-dependent (curvature) interfacial strain energy. A variety of synthesis techniques have been reported to produce *nc*-Si embedded in *a*-SiO_x including co-sputtering of Si and SiO_2 and Si ion implantation into SiO_2 thin films [93]. Regardless of fabrication technique, a recent theoretical study has suggested that the mechanism promoting *nc*-Si formation in *a*-SiO_x is largely governed by suboxide penalty from incomplete O coordination [17]. At the present, relatively little reliable property information for *a*-SiO_x ($0 < x < 2$) is available in comparison to the well-studied endpoint cases of *a*-Si and *a*-SiO_2.

In this chapter, established methods based on first-principles DFT calculations are employed to predict mechanical and optical properties for both *a*-Si:H and *a*-SiO_x bulk materials. In particular, various compositions of bulk *a*-Si:H (at.% H = 0, 5.9, 11.1, and 15.8) and *a*-SiO_x (x = 0, 0.5, 1.0, 1.5, and 2.0) are evaluated to demonstrate elastic and bulk moduli predictions. For the same matrix compositions, the real and imaginary components of the complex dielectric function spectra ($\varepsilon(\omega) = \varepsilon'(\omega) + i\varepsilon''(\omega)$), low-frequency dielectric constants (ε_o), and band gaps (E_g) are also presented. Overall, comparison of these results with previous experimental measurements and available theoretical studies shows reasonable agreement for *a*-Si and *a*-SiO_2, which have been heavily studied. These mechanical and optical property predictions provide valuable characterization of property variation with composition for these technologically significant materials while simultaneously evaluating theoretical methodologies that are easily applicable to other materials. The majority of the work in this chapter was previously published [95].

6.2 Structural Models

Largely defect-free *a*-SiO_x and *a*-Si:H structures were constructed using an approach described in further detail by Yu *et al.* [17] that employs continuous random network model (CRN)-based Metropolis Monte Carlo (MMC) sampling with Keating-like potentials. To sample the structural variation present in the amorphous samples, three to five independent structures were evaluated for each stoichiometric composition in this study. Figure 6.1 shows the lowest energy configuration for each composition investigated, while Table 6.1 summarizes supercell composition and size, sample quantity, and density.

Figures 6.2 and 6.3 show the radial distribution function (RDF) of each composition in this study to provide a metric for comparison of SRO in the presented amorphous structures. Each subplot represents the average SRO of all samples of a given composition. In Fig. 6.2, the Si-H peak location is consistent with the reported [96] Si-H bond length of 1.48 Å. In the generation of these *a*-Si:H structures, care was taken in the initial MMC seeding to homogenize the H atoms to inhibit the occurrence of molecular hydrogen. Since the H_2 bond length is 0.74 Å [97], the RDF data in Fig. 6.2 indeed shows that H_2 is absent in these structures. Statistical analysis of bond angles ($\theta_{Si\text{-}Si\text{-}Si}$ and $\theta_{Si\text{-}Si\text{-}H}$) in these structures shows a trend for both the average and standard deviation to increase slowly as H content increases.

In Fig. 6.3, the first nearest neighbor peak of Si-Si, typically near 2.34 Å in *a*-Si [96], decays away while the Si-O and O-O peaks intensify as x increases in *a*-SiO_x. The sharpest peak representing the Si-O bond occurs near 1.6 Å, which is typical in vitreous SiO_2 [98]. Like the *a*-Si:H structures, statistical analysis of bond angles ($\theta_{Si\text{-}Si\text{-}Si}$, $\theta_{O\text{-}Si\text{-}O}$, $\theta_{Si\text{-}O\text{-}Si}$, and $\theta_{Si\text{-}Si\text{-}O}$) shows a trend for increasing average bond angle as O content increases. The Si-O-Si bond angle is an important metric for characterizing amorphous

silica. The average $\theta_{Si\text{-}O\text{-}Si}$ for the three *a*-SiO_2 samples is 150.5 ± 10.9°, which is in excellent agreement with measurements derived from NMR spectra of 151 ± 11° [99]. Analysis of the ring-size distribution shows that six-membered rings are preferred across the entire *a*-SiO_x composition range, but the distribution spreads as O content is increased.

To accommodate the unique structural topology of each sample, volume relaxation was performed using DFT on each cubic supercell to determine the equilibrium volume and density of every structure. Equilibrium volume determination from sample-specific volume relaxation, rather than a fixed volume determined from experimental densities, was found more beneficial in producing expected mechanical responses in this computational framework. Consistent with experimental results, the densities of the lowest energy structures for *a*-Si and *a*-SiO_2 show the best agreement with published densities of 2.30±0.01 (Ref. 100) and 2.2 g/cm^3 (Ref. 101), respectively. For further structural comparison, qualitatively similar electronic density of states were obtained for the *a*Si64H8 samples as reported structures of identical composition prepared using MD simulations in Ref. 102.

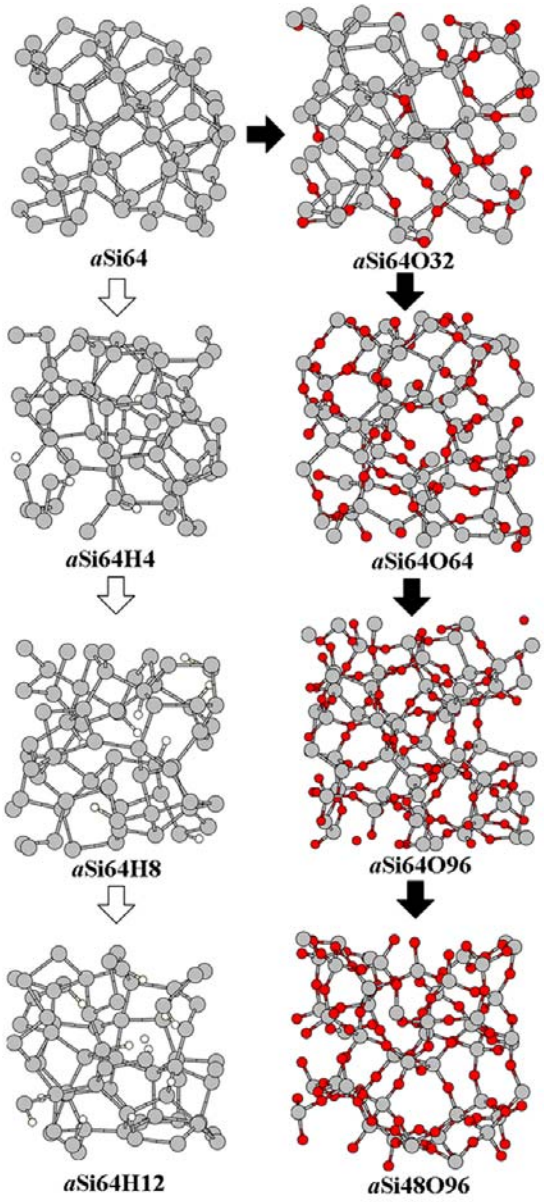

Figure 6.1: (Color available) Amorphous configurations of various compositions of *a*-Si:H and *a*-SiO_x constructed from *a*-Si. White and black block arrows denote increasing H and O content, respectively. Configuration names quantify the constituent atomic species in each sample supercell. Silicon, oxygen, and hydrogen atoms are represented by grey (large), red (medium), and white (small) spheres, respectively.

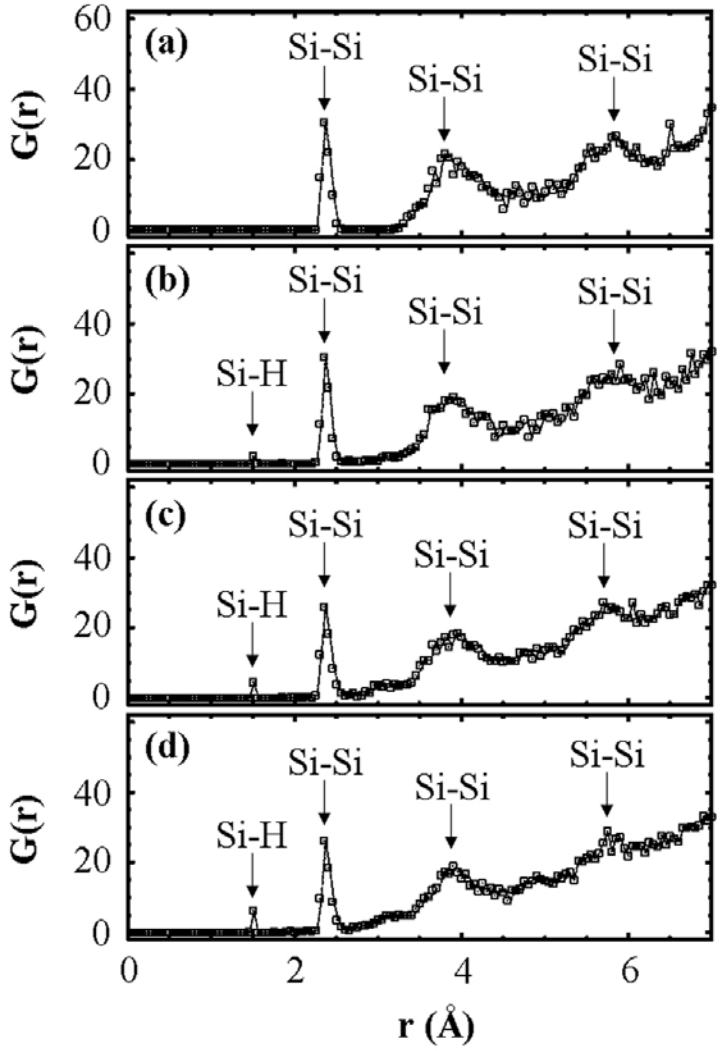

Figure 6.2: Radial distribution functions characterizing the amorphous structure of (a) *a*Si64, (b) *a*Si64H4, (c) *a*Si64H8, and (d) *a*Si64H12 compositions of *a*-Si:H. Each plot represents the bond topology of all samples of that composition. Significant peaks are annotated by the corresponding interaction pair represented.

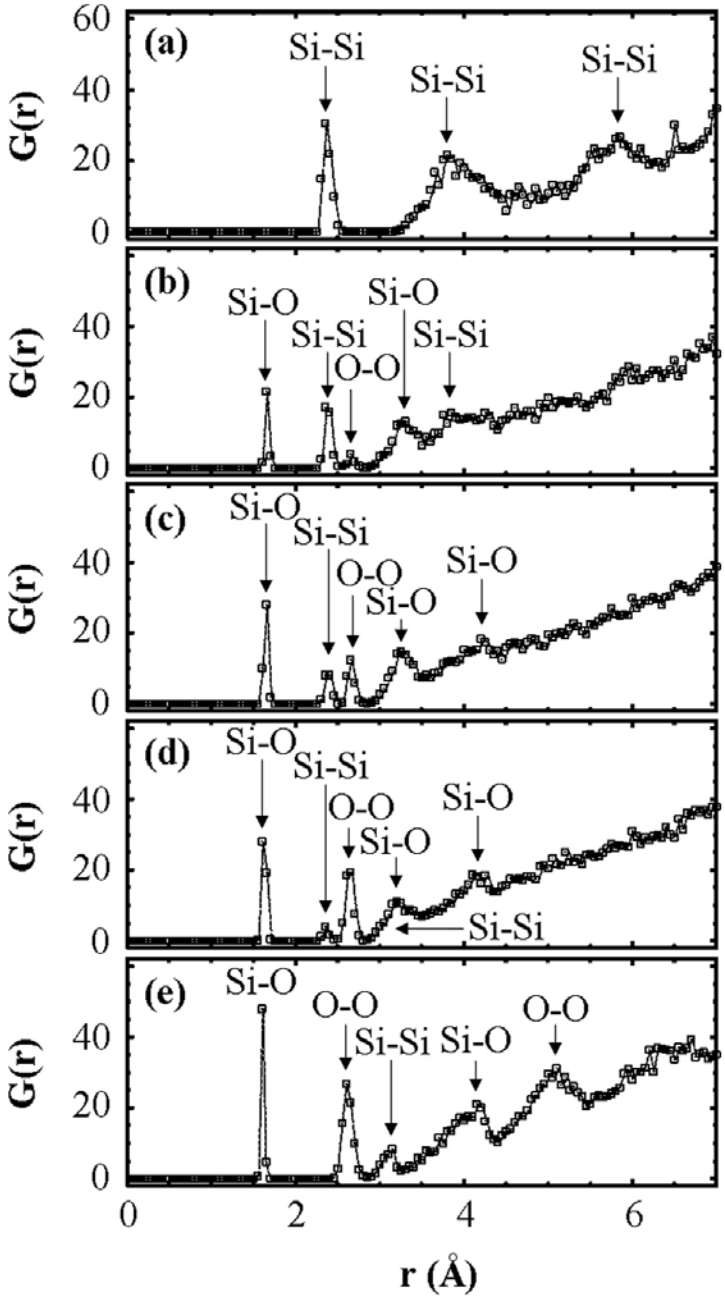

Figure 6.3: Radial distribution functions characterizing the amorphous structure of (a) *a*Si64, (b) *a*Si64O32, (c) *a*Si64O64, (d) *a*Si64O96, and (e) *a*Si48O96 compositions of *a*-SiO_x. Each plot represents the bond topology of all samples of that composition. Significant peaks are annotated by the corresponding interaction pair represented.

6.3 Mechanical Properties

For mechanical property calculations, the kinetic energy cut-offs (E_{cut}) for the planewave basis set and the Monkhorst-Pack (MP) grids for Brillouin zone (BZ) sampling are summarized in Table 6.1. Geometric optimization was run on all structures until residual forces had converged within 5×10^{-2} eV/Å tolerance. With optimized ionic positions fixed, total energies were reevaluated using increased k-point sampling as indicated in Table 6.1. Adequate BZ sampling was determined for various compositions by increasing k-point sampling until total energy convergence was achieved.

To provide adequate statistical sampling of Y for each structure sample, Y was evaluated at each condition for $-5\% \le \varepsilon \le 5\%$ at 0.5% intervals using a custom Perl script to manage numerous VASP simulations. To ensure a stress-free state occurs at strain-free conditions, a small, systematic correction (on the order of 1 GPa) was generally required for each structure and applied to all stress calculations. Similarly, B was evaluated at each condition for $-5\% \le \varepsilon_v \le 5\%$ at 0.5% intervals and corrections generally < 1 GPa were applied to enforce correspondence between stress-free states and strain-free conditions.

While both Y and B were evaluated at 21 strain conditions per sample [$-5\% \le y \le 5\%$ ($y=\varepsilon,\varepsilon_v$ at 0.5% intervals)], the mechanical responses nearest strain-free conditions were systematically poorly-behaved; consequently, the reported values in Table 6.1 represent the remaining 16 strain conditions per sample following omission of the data range $-1\% \le y \le 1\%$ ($y=\varepsilon,\varepsilon_v$). Additional mechanical properties, such as Poisson's ratio (ν) and shear modulus (G), can be calculated once Y and B are known because only two of these four quantities are independent in isotropic materials [103].

Table 6.1 provides a summary of mechanical property calculations over 35 total amorphous samples studied representing eight different compositions of *a*-Si:H and *a*-

SiO_x matrices. For the supercell sizes employed, it is not possible to achieve an ideally random sample of disordered bond topology, so compensation is achieved by sampling multiple independent structures at various strain conditions. Standard deviations are provided with all calculated moduli to show the inherent variation that occurs when sampling small amorphous structures.

Table 6.1: Computed mechanical property summary by composition of *a*-Si:H and *a*-SiO_x structures. Sample names quantify the constituent atomic species in each supercell. BZ sampling schemes using MP meshes are given for geometric optimization together with increased sampling schemes in () when optimized ionic positions were fixed. The average mass density over each sample count is given by ρ_m. *Y* represents an average elastic modulus over all structures sampled, each of which is an average over the strain conditions evaluated. The uncertainty associated with each *Y* is the average standard deviation obtained from each sample. *B* represents analogous quantities for the bulk modulus.

Sample	Sample Count	k-point mesh[a]	E_{cut}[b]	ρ_m (g/cm^3)	Y (GPa)	B (GPa)
			***a*-Si:H**			
a Si64	3	α (β)	γ	2.26	140.7 ± 8.1	74.5 ± 14.9
a Si64H4	4	α (β)	γ	2.20	134.0 ± 18.1	70.9 ± 15.1
a Si64H8	5	α (β)	γ	2.17	121.5 ± 7.8	67.9 ± 16.2
a Si64H12	5	α (β)	γ	2.13	115.0 ± 10.5	62.4 ± 14.6
			***a*-SiOx**			
a Si64	3	α (β)	γ	2.26	140.7 ± 8.1	74.5 ± 14.9
a Si64O32	4	Γ (α)	λ	2.24	129.0 ± 8.6	66.9 ± 11.9
a Si64O64	4	Γ (α)	λ	2.21	118.1 ± 12.1	63.1 ± 9.4
a Si64O96	4	Γ (α)	λ	2.16	101.3 ± 13.6	56.6 ± 11.2
a Si48O96	3	Γ (α)	λ	2.17	91.4 ± 19.6	46.0 ± 12.2

[a] Γ=Γ-point, α=(2×2×2), β=(3×3×3)

[b] γ=160 eV, λ=350 eV

6.3.1 Amorphous Hydrogenated Silicon (a-Si:H)

From Table 6.1, the calculations show a trend for the elastic modulus (*Y*) to decrease in *a*-Si:H materials as H content increases and density decreases. *Y* decreases from 140.7 to 115.0 GPa as H content increases from 0 to 15.8 at.%. Previous experimental results are varied for *Y* dependence on H content. Kuschnereit *et al.* [88]

deposited both laser and plasma CVD *a*-Si:H films and observed *Y* to reach a maximum of 134±5 GPa at 10 at.% H, then sharply decrease with increasing H content. A similar *Y* is seen in the present results of 121.5 GPa at 11.1 at.% H, but instead embedded in a monotonically decreasing trend with increasing H content. Kuschnereit *et al.* acknowledged both evidence of hydride polymerization for the highest H content films and the simultaneous sharp decrease in density suggesting void formation as aspects likely unique to their CVD deposition processes.

In a different study, Jiang *et al.* [104] studied *a*-Si:H films deposited by RF sputtering and show a consistent decrease in *Y* from 100 GPa near 1 at.% H to 55 GPa near 17 at.% H. While their monotonically decreasing *Y* trend is similar to the present results, they also show $Y \approx 105$ GPa for Si(111), which is lower than expected (Brantley [36] shows *Y* is 168.9 GPa on Si{111}). In addition, Jiang *et al.* acknowledged holes in the surface morphologies of their films which suggests void incorporation and consequent reduction in *Y*. The present results likely deviate from these experimental studies because both the H distribution and void fraction in the deposited *a*-Si:H films is likely less homogeneous than the model atomic structure samples.

The present calculations also predict a trend for the bulk modulus to decrease as H incorporation in *a*-Si:H increases. *B* decreases from 74.5 to 62.4 GPa with increasing H content from 0 to 15.8 at.%, consistent with previous *B* experimental results (75 to 109 GPa for *a*-Si (Refs. 100 and 105) and 59 GPa for films with ~10% H (Ref. 106)). This wide range of *B* (75 to 109 GPa) in *a*-Si from the work of Szabadi *et al.* [100] was determined using surface acoustic wave and Rutherford backscattering spectroscopies on amorphized Si layers in implanted *c*-Si. Their property summary provides a good example of the variation in amorphous material properties attributable to changes in

implant dose, implant energy, and annealing parameters and also shows that both *Y* and *B* decrease as *a*-Si film density decreases.

In order to justify the three to five sample sizes used at each composition, additional samples of both *a*Si64 and *a*Si64H12 structures were generated and their mechanical properties were evaluated. For *a*Si64, the sample count was increased from three to ten. As a result, *Y* decreased from 140.7 to 139.0 GPa and *B* increased from 74.5 to 75.6 GPa. This represents a 1.2 and 1.5% change in *Y* and *B*, respectively. For *a*Si64H12, the sample count was increased from five to twelve. As a result, *Y* decreased from 115.0 to 114.8 GPa and *B* increased from 62.4 to 63.4 GPa. This represents a 0.3 and 1.6% change in *Y* and *B*, respectively. In an effort to balance calculation accuracy and computational requirements, the small percent change in the moduli predictions resulting from seven additional samples of *a*Si64 and *a*Si64H12 justifies the three to five sample count criterion in this work, particularly in the objective of identifying property changes as a function of composition.

6.3.2 Amorphous Silicon-Rich Silicon Oxide (a-SiO_x, $0 \leq x \leq 2$)

The present calculations also show a clear trend for *Y* to decrease in *a*-SiO_x as O content increases and density generally decreases. The DFT-GGA calculations predict *Y* = 140.7 GPa and 91.4 GPa for *a*-Si and *a*-SiO_2, respectively. Experimentally-measured *Y* values for *a*-Si range from 125 (Ref. 100) to 167 GPa (Ref. 107). For *a*-SiO_2, experimental *Y* measurements include 70 (Ref. 108) to 73 GPa (Ref. 109) in bulk silica, 76.6±7.2 GPa (Ref. 110) for *a*-SiO_2 nanowires (independent of wire diameter), and values as large as 144 GPa have been reported in films deposited by plasma-enhanced chemical vapor deposition (PECVD) [111].

Similarly, a distinct trend is observed for *B* to decrease in *a*-SiO_x with increasing O content and decreasing density. The predicted values of *B* = 74.5 and 46.0 GPa in *a*-Si

and *a*-SiO_2, respectively, are in good agreement with previous computational results (75 GPa for *a*-Si (Ref. 112) and 37 GPa for *a*-SiO_2 (Ref. 113)) and reasonable agreement with results determined from experimental studies (75 to 109 GPa for *a*-Si (Refs. 100 and 105) and 33.3 GPa for *a*-SiO_2 (Ref. 108)).

A limited amount of experimental information has been reported on the mechanical properties of amorphous silicon monoxide (*a*-SiO_x, x=1) thin films. The work of Hoffman *et al.* [114] produced *a*-SiO_x ($0.9 \leq x \leq 1.0$) films through various evaporative deposition techniques and Young's modulus measurements using a nanotensilometer. They reported *Y* to vary between 53 and 75 GPa, which suggests that *Y* for *a*-SiO is actually softer than either *a*-Si or *a*-SiO_2 and smaller than the computed *Y* of 118 GPa for *a*-SiO in this work. However, they also acknowledged that the bulk film density (2.13 g/cm^3) used to calculate *Y* could be a likely source of variation in their reported values and further detailed that evaporative deposition can yield *a*-SiO films with densities varying from 1.51 to 2.15 g/cm^3. Furthermore, their assumed bulk density applied to all samples likely lowers the *Y* for their films. For comparison, the average density of the *a*-SiO samples in this work is 2.21 g/cm^3, which is intermediate to the densities of the *a*-Si and *a*-SiO_2 samples. As previously described, volume and density were optimized for every structure sample and this is likely the primary reason for calculation of a higher *Y* for *a*-SiO.

6.3.3 Structural Contributions to Moduli

From the moduli synopsis in Table 6.1, it is apparent that addition of either H or O to *a*-Si tends to reduce or soften both *Y* and *B*. Fundamentally, this observed property behavior is related to changes in atomic network connectivity. For example, a complete covalent network for Si only occurs in pure *c*-Si and *Y* along <110> directions within {100} planes is 168.9 GPa [36]. In *a*-Si, disorder reduces the interconnectivity among Si

atoms, the mean coordination number correspondingly falls below four, and *Y* drops to 140.7 GPa (Table 6.1). O incorporation in *a*-Si further reduces atomic connectivity because each O is a twofold-coordinated flexible linkage in the network rather than the more rigid fourfold-coordinated linkage of each Si in *a*-Si. As a result, bond angle distortion in *a*-SiO_x preferentially occurs at bond angles subtended by O atoms, not Si atoms. Similarly, H incorporation in *a*-Si increases the atomic network flexibility because every Si-H bond formed effectively severs covalent network interconnection. Decreased atomic network connectivity also correlates with a general reduction in density of *a*-Si as either H or O content is increased.

Variations in mechanical properties obtained via experiment are related to a number of factors including deposition process and conditions, annealing procedure, measurement technique, film density, material homogeneity, and sample purity. In this first-principles approach, the biggest source of property variation, particularly within the same composition, is likely attributable to limited sampling of the ideally random bond topology. It is expected that the standard deviations in reported moduli could be reduced through a better statistical sampling of the amorphous network by either increased sample counts (intersample variance reduction) and/or larger supercells (intrasample variance reduction).

6.4 Optical Properties

The computational details of the four-step optical calculation procedure (Chapter 2) applied to bulk amorphous materials are described in this section. First, the ionic positions in each structure sample were optimized using the same force convergence criterion as the mechanical property calculations and the same BZ sampling schemes shown in Table 6.1. Second, the charge density distribution was obtained with 5×5×5 and 3×3×3 k-point meshes for *a*-Si:H and *a*-SiO_x, respectively. Third, the frequency-

dependent dielectric matrix was calculated from the optimized charge density distribution using the tetrahedron method [10] and 200 conduction bands for each composition (which was found sufficient to sample transition energies across the range of supercell sizes investigated). Finally, the OPTICS code of Furthmüller [46] was used to compute the imaginary (ε") and real (ε') parts of ε(ω). For all optical property calculations in this chapter, the cut-off energies employed with PAW pseudopotentials were 250 eV and 300 eV for *a*-Si/*a*-Si:H and *a*-SiO_x (x > 0) systems, respectively. Note that the same DFT calculation conditions were used for *a*-Si and *a*-Si:H, unless noted otherwise.

Figures 6.4 and 6.5 show the optical spectra obtained through calculation of the dielectric function for all compositions of *a*-Si:H and *a*-SiO_x considered in this study. As typically seen in amorphous systems, the absence of long-range order and k-point conserving transitions smoothes out the optical response and washes away many of the characteristic transition edges and peaks exhibited by crystalline semiconductor spectra [41,115]. The major features that remain to distinguish among the amorphous samples are the fundamental absorption edge (E_0) and asymmetric main absorption peak (E_2) in Im[ε(ω)] and the transition energy of anomalous dispersion and dielectric constant (ε_o) evident in Re[ε(ω)]. These key spectral features are also sensitive to material phase. For example, ε_o = 11.9 in *c*-Si [87], while amorphization changes ε_o to ~16 in *a*-Si [115]. Similarly, ε_o = 4.6 in *c*-SiO_2 (α-quartz || to optical z-axis [116]), while amorphization changes ε_o to 3.9 in *a*-SiO_2 (thermal oxide thin film [109]).

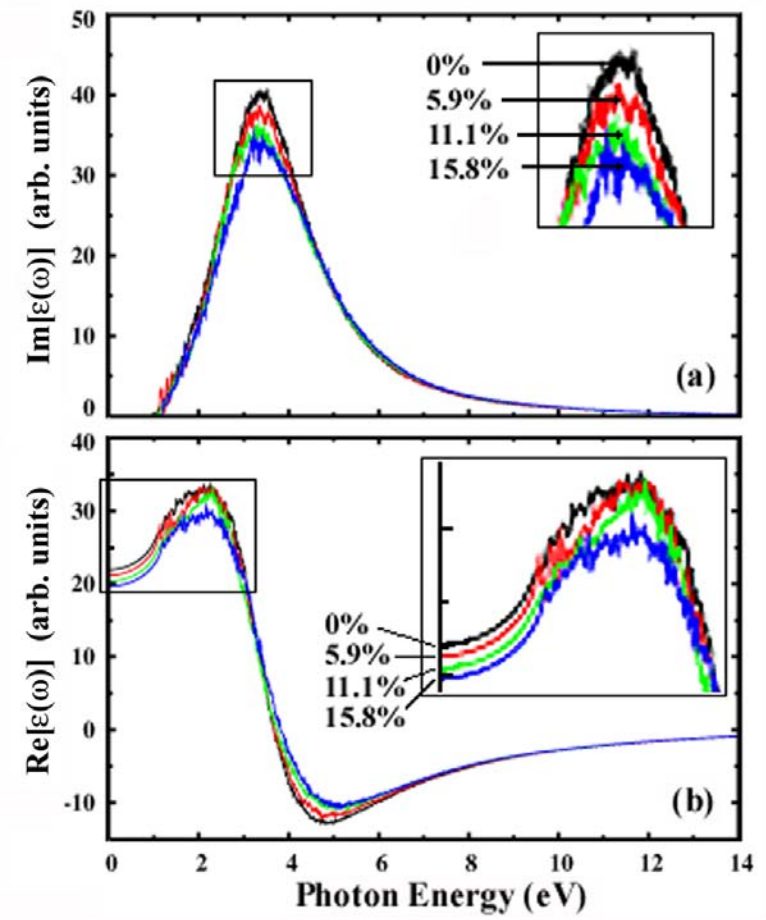

Figure 6.4: (Color available) Imaginary (a) and real (b) parts of the complex dielectric function spectra for *a*-Si:H computed from DFT-GGA calculations. The spectra are annotated by at.% H. For each composition, only the lowest energy structure is represented in the spectra. The insets provided illustrate the sequence of constituent spectra.

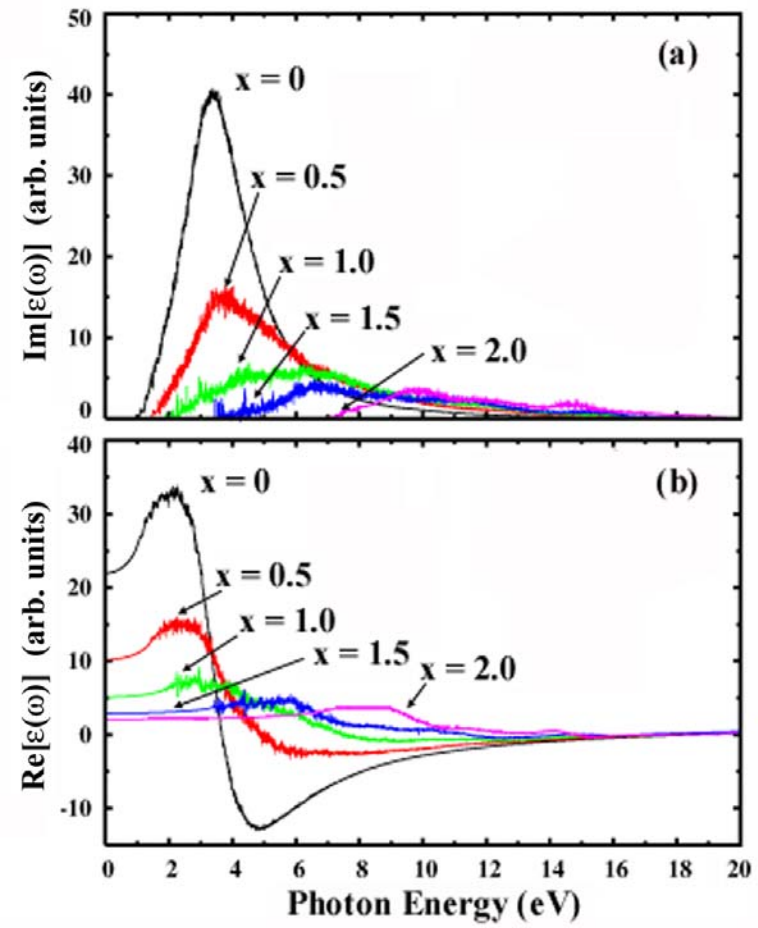

Figure 6.5: (Color available) Imaginary (a) and real (b) parts of the complex dielectric function spectra for *a*-SiO_x computed from DFT-GGA calculations. The spectra are annotated according to O stoichiometry (x) relative to Si. For each composition, only the lowest energy structure is represented in the spectra.

Figure 6.6 provides the DFT-calculated Im[ε(ω)] spectra for *c*-Si and *c*-SiO_2 (α-quartz) for comparison with their amorphous counterparts. Simulated *c*-Si spectra [Fig. 6.6(a)] in this work is similar to that reported by Adolph *et al.* [41] and provides a classic example for introduction of important nomenclature in Im[ε(ω)] spectra. The onset of Im[ε(ω)] intensity in the low-energy region is often termed the fundamental absorption edge or E_0 transition. Im[ε(ω)] rises to an asymmetric peak (E_1) just above the absorption edge from transitions occurring along <111> directions in the BZ. The

Im[ε(ω)] spectra typically reach a maximum at a characteristic energy called the E_2 transition, which is associated with transitions occurring over a large region of the BZ. Note that the well-known DFT band gap underestimation in these GGA independent-particle calculations is manifested as spectral redshifting to lower energies, so these results should not be compared directly to experiments without proper adjustment of transition energies. The *c*-SiO_2 spectra [Fig. 6.6(b)] is reasonably similar to that shown in Refs. 49 and 117 for α-quartz. The details of the electronic structure of *c*-SiO_2, even from experimental results, is often a bit ambiguous in the literature because of measurement difficulties associated with the formation of excitons that obscure accurate determination of the band gap and the persistence of crystal defects [49].

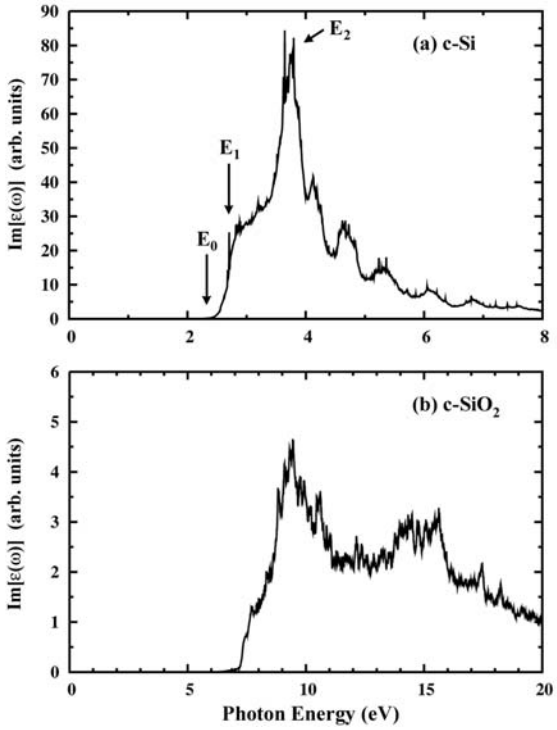

Figure 6.6: Computed imaginary component of ε(ω) for both (a) *c*-Si and (b) *c*-SiO_2 (α-quartz phase). Unlike their amorphous counterparts, the spectra of crystalline materials reveal distinct peaks that are attributed to transitions near Van Hove singularities in the joint density of states. The nomenclature for labeling optical transition energies in tetrahedrally-bonded semiconductors is described in further detail by Yu and Cardona [87].

6.4.1 Amorphous Hydrogenated Silicon (a-Si:H)

As shown in Fig. 6.4(a), the shape of Im[ε(ω)] incrementally transitions as the H content increases in *a*-Si:H. In particular, the reduction in intensity of the main E_2 absorption peak, which occurs between 3 and 4 eV, is evident and consistent with experimentally-derived spectra [115,118] In the Re[ε(ω)] spectra of Fig. 6.4(b), a subtle broadening is observed in the anomalous dispersion region that coincides with incremental reduction in ε_o as H incorporation increases. Decreasing spectral peak intensities and decreasing ε_o are observed for *a*-Si:H as H increases, which correlates with an increasing optical gap [115]. Experimental results [115] also confirm increasing H content lowers ε_o in *a*-Si:H.

Feng *et al.* [118] report Im[ε(ω)] spectra for *a*-Si:H films of variable H content grown by DC magnetron sputtering and measured with spectroscopic ellipsometry. Their spectra exhibits a similar reduction in E_2 peak intensity like that observed in Fig. 6.4(a), as well as the expected blueshift of the E_2 peak as H content increases that is not readily apparent in the present results. The expected blueshift of E_2 is easier to see in the results of Feng *et al.* partly because they examined films up to 24 at.% H. Despite the limitations of DFT calculation methods, the E_2 transition energy for the unhydrogenated *a*-Si sample (3.4 eV) is surprisingly similar to the results of Feng *et al.* (3.60 eV). To produce their Im[ε(ω)] spectra from ellipsometric data, they made several assumptions that potentially affect their results: (1) 50% void fraction for estimation of the film surface layer roughness, (2) film morphologies identical to those from previous experiments, and (3) validity of the effective medium approximation [119] to derive film densities. Since optical characterization of thin films through ellipsometry requires accurate description of structural parameters (film thickness, surface roughness, and substrate interface quality) [119,120], the validity of these requisite assumptions is

paramount to the extracted properties. Furthermore, they report ±10% error in the measurement of H content of their films.

The results of Rantzer *et al.* [120] on films grown by DC magnetron sputtering corroborate the expectation that a greater change in H content in *a*-Si:H films is required to observe the blueshift in the E_2 transition energy. They report a change of only 0.5% in E_2 transition energy when H content is increased from 8 to 10 at.% H. This amount of change is effectively noise considering the uncertainty inherent in their fitting methods. In addition, they report a reduction in E_2 peak magnitude of only 1.1% for the same composition change.

In order to better correlate the relationship between optical spectra and electronic structure as a function of composition, the E_g and ε_o of all sample structures studied are shown in Fig. 6.7. Figure 6.7(a) shows a trend of reduction in ε_o as H content increases in *a*-Si:H; however, a trend in E_g with composition is not readily apparent. The variation in E_g observed is also likely aggravated by the aforementioned small increments in H composition across *a*-Si:H samples, which makes a clear trend difficult to resolve.

In addition, supplemental simulation results were analyzed which show that E_g generally decreases with sample mass density at an arbitrary *a*-Si:H composition, so fluctuations in density from sample-to-sample can produce small fluctuations in E_g, although these fluctuations in E_g are on the order of 0.01 eV. An increasing trend for E_g with increasing H content is expected to be more apparent with larger supercells and/or increased sample sizes.

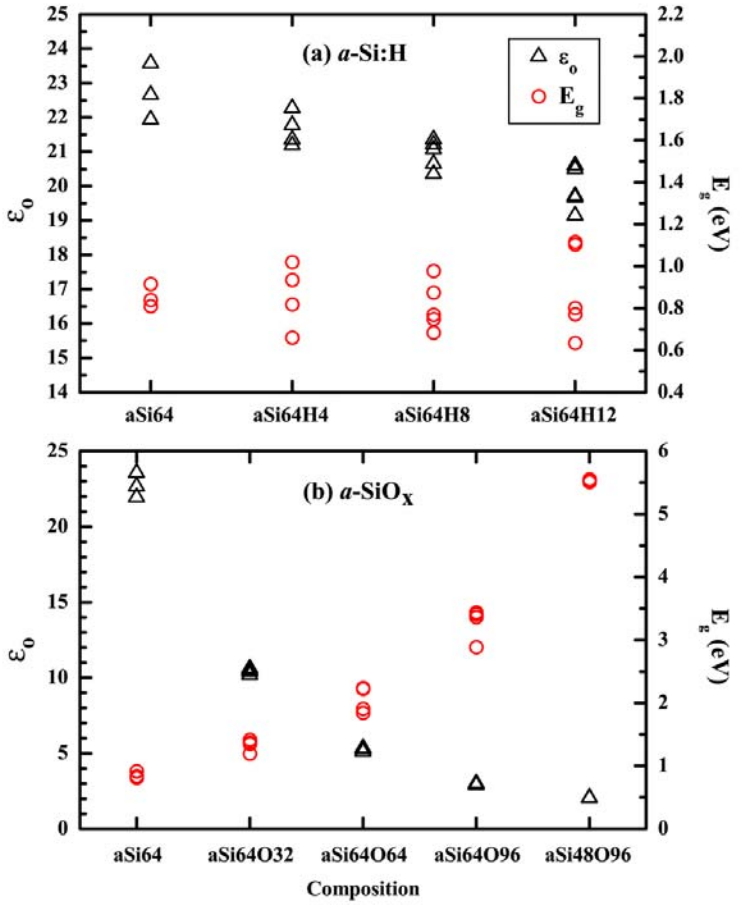

Figure 6.7: (Color available) Dielectric constant (ε_o) and band gap (E_g) for all (a) *a*-Si:H and (b) *a*-SiO_x amorphous structure samples studied. The dielectric constants were obtained from the optical spectra as $\lim_{\omega \to 0} \mathrm{Re}[\varepsilon(\omega)]$. The band gaps were obtained from total density of states calculations for each sample. The data shown is produced from DFT-GGA calculations; therefore, E_g values are underestimated and ε_o values are overestimated. The scaling of ε_o and E_g in (a) was arbitrarily adjusted to separate the two trends for visual clarity.

6.4.2 Amorphous Silicon-Rich Silicon Oxide (a-SiO_x, $0 \leq x \leq 2$)

Similar to the *a*-Si:H optical response behavior, Fig. 6.5(a) shows the shape of Im[ε(ω)] incrementally transitions from *a*-Si to *a*-SiO_2 with a more pronounced trend than observed for *a*-Si:H. As O content increases, the magnitude of the E_2 absorption

peak sharply decreases and blueshifts, while the absorption edge also blueshifts to higher photon energies. The decreasing peak magnitude with increasing O content is largely associated with an increasing band gap as shown in Fig. 6.7(b). As shown in Fig. 6.5(b), a similar incremental transition is evident in Re[ε(ω)] as O content increases from *a*-Si to *a*-SiO_2. Not only does the anomalous dispersion region blueshift, but the transition region broadens in correlation with the peak broadening seen in the Im[ε(ω)] spectra. The incremental decrease in low-frequency ε_o ($\lim_{\omega \to 0} \mathrm{Re}[\varepsilon(\omega)]$) is also evident in Fig. 6.5(b) as O content increases. The ε_o data obtained from each *a*-SiO_x sample is consolidated as a function of composition in Fig. 6.7(b). Unlike the *a*-Si:H case, the inverse relationship between ε_o and E_g is vividly apparent over the complete *a*-SiO_x composition range. Excellent precision is obtained across three samples for the predicted properties of *a*-SiO_2 as shown in Fig. 6.7(b).

Note that the DFT-GGA method employed here using the longitudinal form of the dielectric matrix provides instructive qualitative behavior for ε_o, but this method also tends to overestimate ε_o because the well-known band gap underestimation increases ε_o, while lattice constant sensitivity and finite basis set errors have additionally been cited for inflating ε_o [41,47]. In addition, the values of ε_o reported herein are from the electronic contribution only, so no ionic contributions are considered. Previous studies have shown neglecting the ionic contribution will not change the trends observed, but can impact the magnitude of the ε_o values [42]. The work of Gajdoš *et al.* [47] provides more details on the sensitivity of the dielectric constant to various approximations within the PAW methodology used in this work.

For both the main absorption peak magnitude and ε_o, it is evident that the greatest changes occur for small values of x, when *a*-SiO_x is most Si-rich. This behavior is consistent with the semiempirical simulation study of Hübner [121] of semiconductor

property variation in the transition region of *c*-Si/*a*-SiO_2 interfaces. There, various electronic properties, including valence charge density distribution and E_g, are shown to have strong x variation for $0 \leq x \leq 1.5$, while properties become similar to *a*-SiO_2 for $x > 1.5$. In contrast to the conclusions of Hübner, E_g [Fig. 6.7(b)] is observed here to increase more rapidly as x increases in *a*-SiO_x. In addition, the fundamental absorption edge is seen to blueshift more rapidly for larger x [Fig. 6.5(a)]. The present results, particularly for E_g dependence on x, may differ from those of Hübner as a consequence of the crystalline structural models used. Not only is the x=0 structural contribution from *c*-Si by design (typical transistor substrate) in his study, but structural parameters derived from *c*-SiO_2 (β-cristobalite) are interpolated with x to model *a*-SiO_x ($x > 0$). In contrast, the structures in this work are all amorphous and bulk in nature.

Reliable optical property data in the literature is scarce for the intermediate compositions of *a*-SiO_x ($0 \leq x \leq 2$), with only a limited amount of information for amorphous silicon monoxide. Hjortsberg and Granqvist [122] calculated $\varepsilon(\omega)$ of evaporated, 99%-pure *a*-SiO films used infrared spectrophotometric measurements. They report a static ε_o value of ~7.2 for *a*-SiO extracted from their $\mathrm{Re}[\varepsilon(\omega)]$ spectra, while tabulated [123] optical properties for *a*-SiO suggest ε_o is 4.0. Here, the results from Fig. 6.7(b) produced an average ε_o for *a*-SiO of 5.3 across four samples. In the E_g data for the suboxide compositions, particularly *a*Si64O64 and *a*Si64O96, some spread in the computed values is attributable to a somewhat ambiguous band gap in which either or both the VB and CB edges have a discontinuous splintering of eigenstates as a function of energy; as a result, it is not possible to precisely define the edges of the gap in those cases. Overall, the wide variation reported in material properties for these suboxide systems is suspected to be a result of significant uncertainty in both composition (including impurities) and sample morphology.

In general, the more subtle changes in optical spectra with composition for *a*-Si:H relative to *a*-SiO_x is largely correlated to the magnitude of change in optical gaps as composition changes. Furthermore, aside from any chemical effects, the physical range of composition investigated is much smaller for *a*-Si:H (0 to 15.8 at.% H) than for *a*-SiO_x (0 to 66.7 at.% O), so the impact on resulting optical spectra should be significantly greater for *a*-SiO_x. The gaps are 1.4 and ~9.0 eV for *a*-Si [87] and *a*-SiO_2 [124], respectively, so the *a*-SiO_x spectra presented cover a gap change of ~7.6 eV; in contrast, a maximum gap of about 1.8 eV [87] can be achieved in *a*-Si:H, so the *a*-Si:H spectra presented here cover a gap change somewhat smaller than the limiting case of 0.4 eV.

The limitations and strengths of DFT-based property predictions in amorphous materials have been detailed throughout this chapter. The most significant limitation in the mechanical property predictions is attainment of either a sufficiently large supercell or a sufficiently large sample size to adequately represent a random bond topology network. The significant limitations in optical property predictions are grounded in both the well-known band gap underestimation associated with DFT calculations and the independent particle approximation for optical transitions. The chief strength of this approach, provided realistic structural models are used, is representation of an exact stoichiometric composition and nanoscale morphology. Experimental property measurements are often obscured by accurate identification of the sample material because factors including deposition process and conditions, annealing procedure, measurement technique, film density, material homogeneity, sample purity, and surface roughness all potentially influence the material properties evaluated.

6.5 Summary

In summary, DFT-based methods are employed for predicting the mechanical and optical properties of variable-composition amorphous matrices (*a*-Si:H and *a*-SiO_x). A

statistical sampling of total energy data for eight different amorphous compositions is used to calculate elastic (Y) and bulk (B) moduli using second order numerical derivatives. Addition of H to *a*-Si monotonically reduces Y by 18.3 % and B by 16.2 % as H incorporation increases to 15.8 at.% H in *a*-Si:H. Similarly, addition of O to *a*-Si monotonically reduces Y by 35.0 % and B by 38.3 % as x increases to 2.0 in *a*-SiO_x. In both cases, the reduction in moduli strongly correlates with decreasing sample density and is largely related to the weakening of the rigid tetrahedral network in Si.

An established PAW methodology based on calculation of the longitudinal form of the dielectric matrix is used to compute optical spectra for the imaginary and real parts of the complex dielectric function, $\varepsilon(\omega)$. As H is added to *a*-Si, the intensity of the main E_2 transition peak of $\mathrm{Im}[\varepsilon(\omega)]$ is observed to decay slowly, while the low-frequency dielectric constant (ε_o) extracted from $\mathrm{Re}[\varepsilon(\omega)]$ simultaneously decreases by 12.3 % as the H content increases to 15.8 at.%. If this study were extended to higher H content in *a*-Si:H, the expected blueshift in the E_2 transition peak with increasing H content should also become apparent. As O is added to *a*-Si, similar, but more pronounced, changes are seen in the optical spectra. A reduction in E_2 peak intensity is accompanied by a blueshift of both the E_2 transition energy and the fundamental absorption edge. Values of ε_o decrease by 91.0 % as x increases to 2.0 in *a*-SiO_x. Unlike the *a*-Si:H case, the decrease in ε_o with increasing O content is observed to strongly correlate to the significant increase in E_g as x increases in *a*-SiO_x.

The strengths have been summarized and the limitations acknowledged in implementation of DFT methods to predict mechanical and optical properties in amorphous materials. Considering the large variation in reported experimental measurements and the limited availability of previous computational results, the property predictions in this chapter provide valuable insight into the mechanical and optical

behavior of *a*-Si:H and *a*-SiO_x materials, especially for the less-characterized intermediate compositions.

Chapter 7

Role of Structural Disorder in Optical Absorption in Silicon

7.1 Introduction

The low efficiency (η) of optical absorption in *c*-Si photovoltaics is one of the fundamental challenges impeding improvement in today's most prolific [125] solar cell substrate. Since Carlson and Wronski [89] reported the first feasible *a*-Si *p*-*i*-*n* solar cell in 1976, relatively inexpensive Si-based thin film materials (including *a*-Si:H and derivative mixed-phase materials containing microcrystalline and/or nanocrystalline Si phases dispersed in *a*-Si:H) [91] have been expected to revolutionize the photovoltaics industry. However, the highest confirmed η for a single-junction *a*-Si:H cell is still less than 10% (Ref. 126), which is inadequate to provide serious competition to reigning *c*-Si solar cell technologies. The redshifted absorption coefficient ($\alpha(\omega)$) and enlarged band gap ($E_g \approx 1.8$ eV) (Refs. 125 and 87) of *a*-Si:H are particularly advantageous relative to *c*-Si with respect to the spectral irradiance [127] from the sun, but the low η ceiling of *a*-Si:H materials will remain until the light-induced degradation of the reversible Staebler-Wronski effect [90,128] (SWE) is circumvented. Significant effort is required to improve *c*-Si absorption through techniques including transition metal doping to create intermediate bands [43] and growth of Si nanowire arrays that function as broadband absorption layers [129].

It is well-established that variations in phase [89,130], defect-content [131,132], and morphology [133-136] (porous Si morphologies vary greatly) of Si produce appreciable changes in the absorption spectra. Knief and von Niessen [131] succinctly

classify the absorption spectra of *a*-Si materials into three categories: (1) high-energy absorption (like *c*-Si) in which transitions occur between extended electronic states (bands); (2) Urbach absorption at lower photon energies in which optical transitions occur between localized states in one band (valence or conduction) and extended states in the opposite band; and (3) tail or defect absorption at the lowest photon energies in which optical transitions are assisted by localized states near the Fermi energy. Localized defects include native defect clusters, which are often generated during ion implantation and crystal growth [73] processes. The recent theoretical work of Pan *et al.* [137] proposed an atomistic topological relationship connecting short (long) Si-Si bonds with valence (conduction) band character in the electronic structure of *a*-Si, which suggests that the strain distribution associated with the bond topology of an arbitrary structure can modify the joint density of states, and consequently optical absorption, in Si.

The ubiquitous presence of vacancies in all crystalline materials and their further proliferation through a variety of semiconductor processes has made them extensively studied using both experimental and computational techniques. A brief synopsis of the theoretical and experimental milestones made in the study of Si vacancy clusters (V_n) was previously provided in Chapter 5. Despite recent computational achievements, small FC clusters have remained elusive to physical verification because of their expected transparency to common experimental techniques such as deep-level transient spectroscopy (DLTS) and photoluminescence (PL) [78]. Similarly, Davies *et al.* [138] report classes of V_n defects which are invisible to infrared spectroscopy and DLTS, yet detectable through positron annihilation and broadband luminescence; however, the structures of their reported cluster defects are not identified. A disconnect remains between theory and experiment because spectroscopic techniques, in general, cannot

provide the structural configurations for small V_n, and microscopy techniques, likewise, cannot provide the subnanometer resolution necessary to resolve small V_n.

In this chapter, a DFT simulation approach is applied to explore the contribution of structural disorder to optical absorption in Si using charge-neutral, ground-state Si vacancy clusters (V_n, $n \leq 6$, $n = 12$ and 32). In particular, calculated optical spectra are presented for the dielectric function ($\varepsilon(\omega)$) and absorption coefficient ($\alpha(\omega)$) for previously-identified FC vacancy clusters and the results are discussed in context with the archetypal spectra of the *a*-Si and *c*-Si phases. In addition, this computational approach is extended to assess the effect of defect concentration, using incremental dilutions of monovacancy optical response, and the effect of density, using amorphous samples, on optical absorption in Si. These simulation results should provide improved understanding of bulk Si optical absorption by exploring the influence of subnanometer-scale structural disorder in *c*-Si via native defect cluster incorporation. Most of the work presented in this chapter was previously published [139].

7.2 Computational Details

During structural optimization with Vanderbilt-type US-PPs [13], a planewave basis set was applied with a kinetic energy cut-off (E_{cut}) of 160 eV, the BZ was sampled at the Γ-point, and all atoms were relaxed until residual forces between atoms had converged within 5×10^{-2} eV/Å. A fixed, DFT-optimized lattice constant of 5.457 Å along <100> or 3.859 Å along <110> was applied to all *c*-Si supercells (with and without defects). For all *a*-Si structures, initial structural optimization was followed by DFT-based volume relaxation on each cubic supercell to determine the equilibrium volume and density of each structure.

For optical calculations, the four-step procedure described in Chapter 2 was utilized to compute $\varepsilon(\omega)$ with VASP following the general theoretical framework

described by Adolph *et al.* [41] Table 7.1 is provided to recapitulate the DFT conditions for the optical calculation sequence for the essential supercell sizes used throughout this chapter.

In the first optical calculation step, the configuration of the relaxed structure (US-PPs) was optimized with PAW pseudopotentials [14] using the same force convergence criterion with cut-off energies and BZ sampling as indicated in Table 7.1. Second, the charge density distribution was obtained using increased cut-off energies and BZ sampling in accordance with Table 7.1. Third, the frequency-dependent dielectric matrix was determined from the optimized charge density distribution using the tetrahedron method [10] and an adequate number of conduction bands that was carefully scaled with supercell size. Since the optical spectra is sensitive to the number of conduction bands, especially at high energies, preliminary calculations were performed to ensure saturation of both the optical spectra and low-frequency dielectric constant (ε_o) as a function of the number of bands simulated. Performing DFT calculations on large 980-atom supercells also presented an unusual challenge. Bound by the constraint of the tetrahedron method (minimum of four k-points), yet also seeking to minimize k-point quantity for the conservation of computational resources, a 2×2×2 Γ-centered mesh was used in the full BZ (k-point reduction via symmetry suppressed), instead of the VASP [10] implementation of the standard Monkhorst-Pack scheme used to generate the other meshes. Inclusion of the Γ-point on even meshes often results in more k-points, while identical meshes are observed for both schemes for odd meshes. This detail was necessary to ensure a mesh with eight k-points for all 980-atom supercells so the tetrahedron method could be applied in all cases, including *c*-Si. Finally, the OPTICS code of Furthmüller [46] was used to obtain both the imaginary (ε_2) and real (ε_1) parts of

$\varepsilon(\omega)$. With ε_1 and ε_2 determined at each ω, the absorption coefficient is computed as an algebraic expression,

$$\alpha(\omega) = \frac{\sqrt{2}E}{\hbar}\left[\sqrt{\varepsilon_1^2(\omega)+\varepsilon_2^2(\omega)} - \varepsilon_1(\omega)\right]^{1/2}, \tag{7.1}$$

where E represents photon energy, $\hbar$ represents the reduced Planck's constant, and energy and frequency are essentially interchangeable via $E=\hbar\omega$.

Table 7.1: Summary of important DFT conditions used for optical calculations with PAW pseudopotentials at various supercell sizes. BZ sampling schemes and cut-off energies are given for structural optimization together with conditions for increased accuracy in () when optimized ionic positions were fixed. The 2×2×2 meshes are Γ-centered, while the odd meshes are standard Monkhorst-Pack grids.

Base Supercell	k-point mesh[a]	E_{cut}[b] (eV)	Conduction Bands
72	α(χ)	δ(γ)	200
480	Γ(β)	δ(γ)	750
980	Γ(α)	δ(γ)	1300

[a] Γ=Γ–point, α=(2×2×2), β=(3×3×3), χ=(9×9×9).

[b] δ=250 eV and γ=300 eV.

7.3 Structure Generation

The same ground-state vacancy structures presented in Chapter 5 provide the foundation for the investigation presented in this chapter. Figs. 5.1(a)-(f) present the neutral, ground-state FC configurations of V_3 through V_6 along with the monovacancy (D_{2d} symmetry) and divacancy (C_{2h} symmetry) configurations. Unless noted otherwise, V_1 through V_6 optical calculations were conducted in 480-atom basis supercells. Figure 7.1 provides illustrations of the larger structures investigated that required the use of 980-atom supercells. Unlike Figs. 5.1(a)-(f), the previously reported structural cores have been isolated for V_{12} [Fig. 7.1(a)] (Ref. 20) and V_{32} [Fig. 7.1(b)] (Ref. 21) from the Si lattice to enhance visual clarity for the reader. Figure 7.1(c) shows the 980-atom *a*-Si

supercell and its RDF, which will be used extensively as a reference case throughout this chapter.

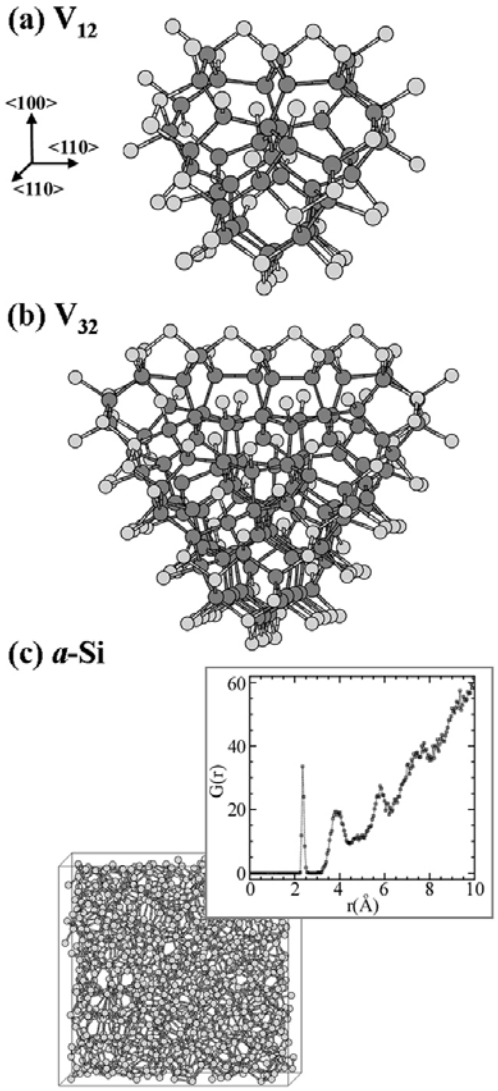

Figure 7.1: Illustrations of large structures modeled with 980-atom basis supercells. The large vacancy clusters (a) V_{12} and (b) V_{32} are isolated from the Si lattice to help highlight their complex, FC configurations. Dark gray spheres represent highly-strained atoms neighboring the V_n, while light gray spheres represent peripheral atoms comprising the bulk *c*-Si interface. The 980-atom representation of *a*-Si is shown in (c) along with its radial distribution function (RDF), which shows excellent agreement with the *a*-Si RDF from x-ray diffraction measurements in Fig. 2 of Ref. [140].

Amorphous Si samples were constructed free of coordination defects using a derivative approach of the method described by Yu *et al.* [17] that employs CRN-MMC sampling with Keating-type potentials. This CRN-MMC method was used to generate at least five samples of each unique size/density of *a*-Si supercell studied, including five different densities (*vide infra* Table 7.4) of *a*-Si in 480-atom basis supercells as well as the 980-atom *a*-Si supercell. The variable-density *a*-Si samples were constructed using the experimental density of 2.28 g/cm^3 (Ref. 141) as the basis for the *a*Si480 reference structure containing 480 atoms. Lower density structures (*a*Si468, *a*Si456, *a*Si444, and *a*Si432) were subsequently generated by seeding the same volume supercell with incrementally fewer Si atoms. Cost-effective US-PPs were applied during structural relaxation to select the lowest energy amorphous sample(s) at each density, then sample-specific volume relaxation was applied on the remaining candidate(s) to identify the lowest energy representative structure for each cell size and/or density.

7.4 Structural Disorder Effects in *c*-Si

This investigation originated as a systematic evaluation of optical spectra based on the FC vacancy clusters described in Chapter 5. The effects of Si divacancies (dangling bonds) on optical absorption were previously measured with spectrophotometry by Stein *et al.* [132] and Knief and von Niessen [131] modeled the effect of both vacancy concentration and coordination defects on optical absorption. These previous results motivated an effort to determine if optical signatures would be readily observable for FC vacancy clusters despite their expected transparency to common experimental characterization techniques [77,78,138].

7.4.1 Small Cluster Absorption (V_n, $n \leq 6$)

Figure 7.2 provides absorption coefficient spectra as a function of both photon energy and wavelength for all V_n shown in Figs. 5.1(a)-(f) along with *c*-Si as a reference for comparison. While an optical signature was anticipated based on the results of Stein *et al.* [132] for clusters with dangling bonds (V_1 and V_2), the substantial magnitude and bandwidth of optical absorption enhancement over *c*-Si was unexpected. The unsaturated bonds in V_1 and V_2 correspond to typical defect absorption [131] in which sharp

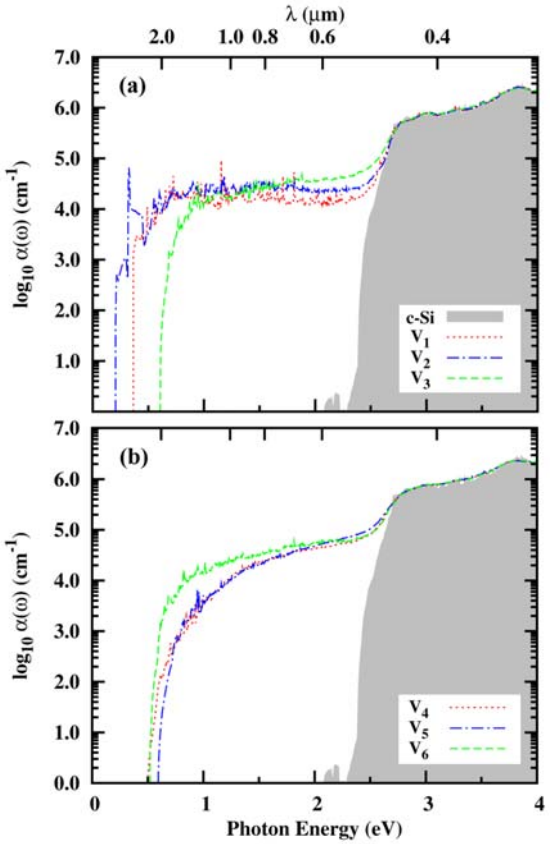

Figure 7.2: (Color available) Absorption coefficient spectra from DFT-GGA calculations for the small vacancy clusters (V_n, $n \leq 6$) depicted in Figs. 5.1(a)-(f) using 480-atom basis supercells. In each plot, the gray-filled region represents the reference $\alpha(\omega)$ for *c*-Si in a 480-atom supercell.

absorption peaks are observed at low energies. These results reveal that similar increases in absorption are also observed for all FC clusters (V_n, $3 \leq n \leq 6$). For these clusters, the onset of incipient absorption occurs at relatively higher photon energies ($E \geq 0.5$ eV) and the general shape of the absorption envelope tends to be much smoother than that seen for the V_1 and V_2 cases.

7.4.2 Large Cluster Absorption (V_{12}, V_{32})

To evaluate the significance of the observations on small V_n ($n \leq 6$), the investigation proceeded with examination of the optical spectra for the large, FC configurations of V_{12} and V_{32}. Since the expanded $\alpha(\omega)$ envelope observed for small V_n is somewhat reminiscent of the well-known *a*-Si $\alpha(\omega)$ enhancement [89], a second reference for *a*-Si is included throughout most of the remaining results for comparison. Figure 7.3 provides the $\alpha(\omega)$ spectra for V_{12} and V_{32} along with *c*-Si [142] and *a*-Si references, all modeled using 980-atom basis supercells, while the corresponding imaginary and real components of $\varepsilon(\omega)$ are introduced for the same structures in Fig. 7.4. From inspection of Fig. 7.3, it is evident that the enhanced absorption seen for the small V_n clusters in Fig. 7.2 is indeed a general attribute of a vacancy cluster embedded in *c*-Si. In Fig. 7.3, observe that the $\alpha(\omega)$ spectra are similar, yet unique, for V_{12} and V_{32} and both are strikingly similar to the $\alpha(\omega)$ spectra of *a*-Si. V_{12}, V_{32}, and *a*-Si all show incipient absorption around 0.5 eV, where the sharp peaks and discontinuities observed exclusively for *a*-Si are likely attributable to highly-strained bonds since structural analysis [143] confirms complete fourfold coordination throughout the final configuration.

The additional details provided by $\varepsilon_2(\omega)$ in Fig. 7.4(a) help exemplify incremental transition across the four sample structures. Using the nomenclature of Yu and Cardona [87] for labeling optical transition energies in tetrahedrally-bonded semiconductors, the sharpness of the fundamental absorption edge, or E_0 transition energy, washes out and

concomitantly redshifts through this structural sequence: *c*-Si, V_{12}, V_{32}, and *a*-Si. Likewise, the sharpness of the shoulder just above E_0, known as the E_1 transition, exhibits an incremental softening across the same aforementioned structural sequence. The critical point at E_1 arises from optical transitions occurring along <111> directions in the BZ [87,144] and has been shown as a resilient metric [144] in the quantification of disorder during amorphization well-beyond the disintegration of other features in the optical spectra. Furthermore, the maximum $\varepsilon_2(\omega)$ peak intensity, or E_2 transition, decays in magnitude and slightly redshifts across the same structural sequence. Correspondingly, inspection of $\varepsilon_1(\omega)$ in Fig. 7.4(b) shows both a broadening in anomalous dispersion and an increase in low-frequency dielectric constant ($\varepsilon_o = \lim_{\omega \to 0} \mathrm{Re}[\varepsilon(\omega)]$) across the same structural sequence.

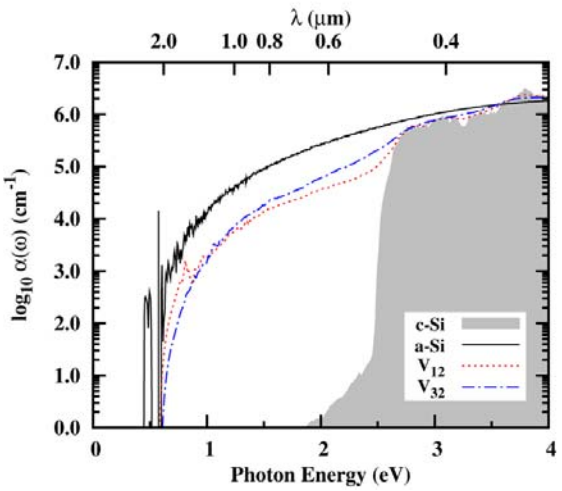

Figure 7.3: (Color available) Absorption coefficient spectra for V_{12}, V_{32}, *c*-Si, and *a*-Si in 980-atom basis supercells computed from DFT-GGA calculations. The gray-filled region represents the reference $\alpha(\omega)$ for *c*-Si.

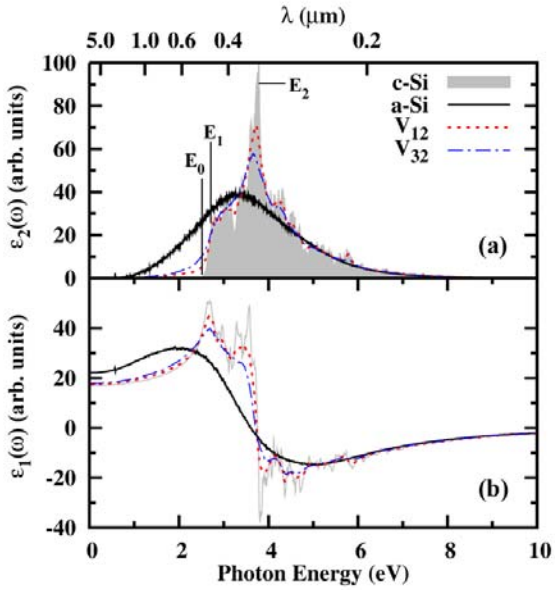

Figure 7.4: (Color available) (a) Imaginary and (b) real parts of the complex dielectric function spectra for V_{12}, V_{32}, *c*-Si, and *a*-Si in 980-atom basis supercells computed from DFT-GGA calculations. The important E_0, E_1, and E_2 transition energies are labeled for *c*-Si in (a).

7.4.3 Absorption in Constant-Density Cluster Distributions

To isolate the influence of topological disorder observed in absorption spectra from the density variation that occurs with changes in vacancy concentration, three different constant-density, 980-atom basis supercells were constructed, each containing a total of twelve vacancies using different combinations of small, FC V_n clusters in Figs. 5.1(a)-(f). Each of these derivative supercells, V_6×2, V_4×3, and V_3×4, contains 968 atoms in a *c*-Si matrix, where the nomenclature V_n×q indicates the quantity (q) of cluster size (n) embedded in each supercell. During the construction of each supercell, an effort was made to homogenize the cluster spatial distribution in order to minimize cluster-to-cluster interactions. These three additional structures, together with V_{12}, provide four samples of constant density and variable topological disorder for further investigation.

Figure 7.5 presents the cumulative absorption spectra for this constant-density vacancy structure set along with the *a*-Si and *c*-Si references. The integrated or cumulative absorption coefficient is defined as

$$\Xi(\omega) = \int_0^{E_{\max}} \alpha(\omega) dE \,, \tag{7.2}$$

where $E_{\max}$ is the maximum photon energy considered and Ξ(ω) is expressed in units of eV/cm. As will be shown later (*vide infra* Fig. 7.8), the cumulative quantity is useful in emphasizing visual trends in somewhat noisy spectra. Inspection of Fig. 7.5 reveals a general trend of absorption enhancement (redshift in E_0 and increase in Ξ(ω) magnitude) among the constant-density spectra largely following this sequence up through the spectral confluence between 2.5 and 3.0 eV: V_{12}, V_6×2, V_4×3, and V_3×4.

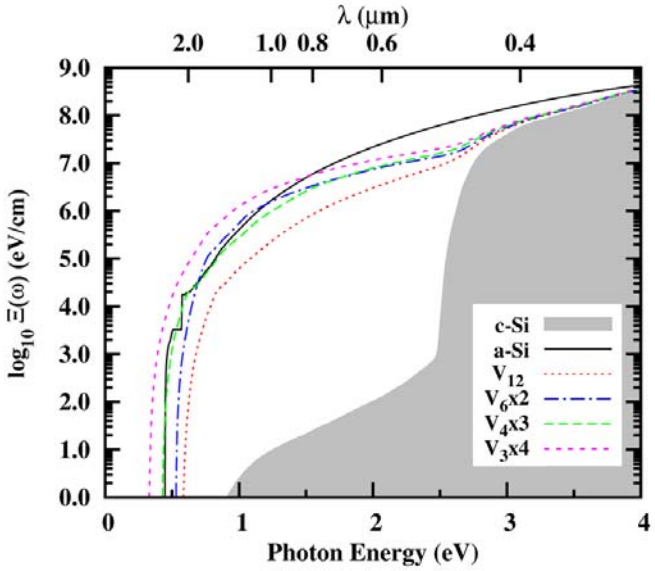

Figure 7.5: (Color available) Cumulative absorption coefficient spectra for constant-density 968-atom supercells (V_{12}, V_6×2, V_4×3, and V_3×4) along with *c*-Si and *a*-Si 980-atom references computed from DFT-GGA calculations. The gray-filled region represents the reference Ξ(ω) for *c*-Si.

Additionally, these simulation results suggest that the V_3×4 configuration has greater cumulative absorption than the *a*-Si reference up to about 1.5 eV. The aforementioned structural sequence of enhanced absorption suggests that cluster size and/or variation in topological disorder likely influence the resultant optical properties.

7.4.4 Statistical Characterization of Structural Disorder

In order to further illuminate the relationship between structural disorder and optical absorption, distributions of highly-distorted bond lengths and angles associated with the 980-atom structures are provided in Fig. 7.6 as well as comprehensive structural analysis in Fig. 7.7 of most of these same structures using cumulative distribution functions (CDFs) of bond lengths and angles. Since the strain fields of small FC clusters can be spatially extensive, CDFs were chosen to elucidate subtle variations among the constant-density vacancy structure bond distributions that were anticipated. Figure 7.6 provides structural distribution signatures for each V_n cluster that highlight the unique character of each cluster in contrast to the almost Gaussian distributions of *a*-Si. It is readily apparent that the bond length distributions for all V_n are distinctly tensile, while the bond angle distributions do not exhibit significant deviations in the mean, relative to *c*-Si. The largest cluster, V_{32}, shows bond length and angle distributions that are beginning to exhibit some Gaussian character, which is a trend expected to continue with increasing *n*.

Figure 7.7 visually depicts the intermediate nature of the structural bond topologies of the constant-density vacancy structures relative to the extreme cases offered by the *c*-Si and *a*-Si distributions. For bond lengths [Fig. 7.7(a)], a general trend is discerned above the 50th percentiles (with some crossover between V_4×3 and V_3×4) of increased spread in bond length distributions correlating with the same structural sequence (V_{12}, V_6×2, V_4×3, and V_3×4) of optical absorption enhancement. Interestingly,

the CDFs for $V_4\times3$ and $V_3\times4$ indicate considerably more compressive bond length character than the CDFs for $V_6\times2$ and V_{12}. Reinforcing the distributions of Fig. 7.6, the plenary bond angle data provided by Fig. 7.7(b) shows a more symmetric nature for all structures relative to the bond length distributions. In addition, increased spread (flattening in CDF) in bond angle distributions below the 25th and above the 70th percentiles for the constant-density vacancy structures is again observed in this sequence: V_{12}, $V_6\times2$, $V_4\times3$, and $V_3\times4$. Thus far, a pattern is consistently observed for enhanced optical absorption corresponding to both increased spatial dispersion ($V_n\times q$, n decreases, q increases) of a fixed vacancy quantity ($n\times q = 12$) in concert with increased dispersion in bond topology distributions.

Table 7.2 provides quantification of important statistics that characterize the bond topology distributions of the 980-atom supercells as well as sample densities and internal strain energies. Strain energies were computed by calculating formation energies on a per atom basis of charge-neutral, Si vacancy clusters as

$$E_f(n) = E_{tot}(n) - \frac{N-n}{N} E_{bulk}, \tag{7.3}$$

where $E_{tot}(n)$ is the total energy of each N-n atom supercell, n is the number of vacancies, N is the basis number of atoms in the c-Si supercell, and E_{bulk} is the total energy of the N-atom c-Si supercell. Equation 7.3 is similarly applicable to variable-density amorphous structures, where $E_{tot}(n)$ instead represents the total energy of the N-n atom a-Si sample and n represents the number of removed Si atoms, if any, relative to the experimental reference density. Based on the work of Lee and Hwang [20], it is not surprising that a trend of increased strain energy is observed as the twelve constituent vacancies are dispersed across an increasing number of clusters since the smaller vacancy clusters have higher $E_f(n)$ on a per vacancy basis. Statistical trends in bond lengths for the constant-

density $V_n \times q$ structures are not readily apparent, but the standard deviations (σ) and interquartile ranges (IQRs) for the bond angles quantify the observations described in the CDFs of Fig. 7.7. Perhaps most importantly, the maximum bond angle (θ_{max}) data for the constant-density $V_n \times q$ structures reveals that both $V_4 \times 3$ (θ_{max}=153.86°) and $V_3 \times 4$ (θ_{max}=159.09°) contain larger bond angles than *a*-Si (θ_{max}=150.58°), which offers a plausible structural explanation for the enhanced redshift in incipient absorption observed for $V_4 \times 3$ and $V_3 \times 4$ relative to *a*-Si in the $\Xi(\omega)$ spectra of Fig. 7.5.

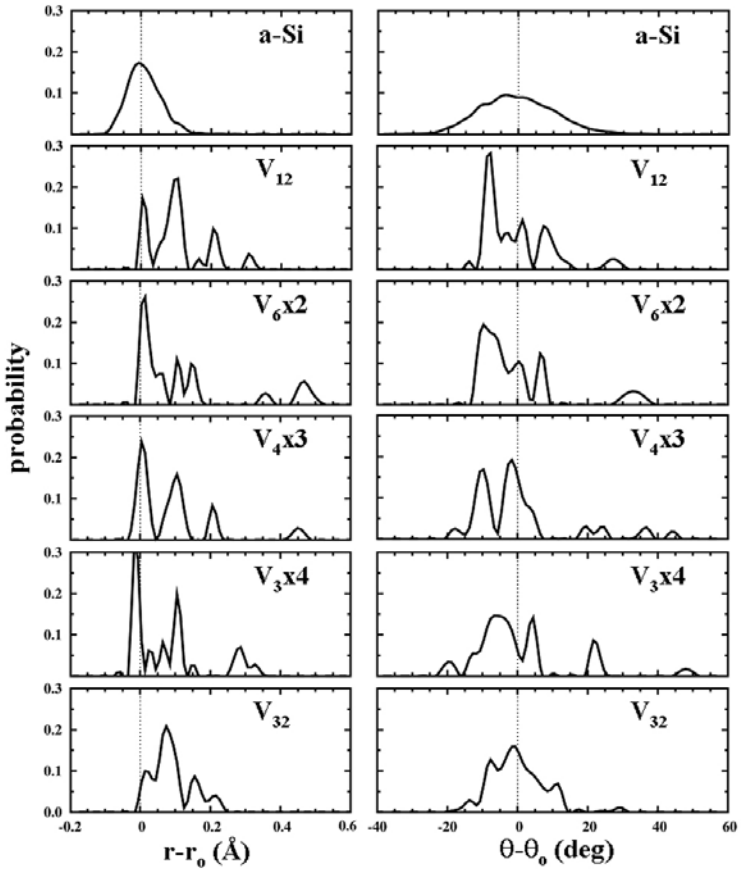

Figure 7.6: Distributions of bond length (left frames) and bond angle (right frames) deviations from their respective DFT-optimized *c*-Si values for various structures in 980-atom basis supercells. In all cases, the probability scale has been normalized to reflect only the highly-distorted atoms comprising each structure. The dotted reference lines represent the equilibrium *c*-Si values of r_o = 2.363 Å and θ_o = 109.47°.

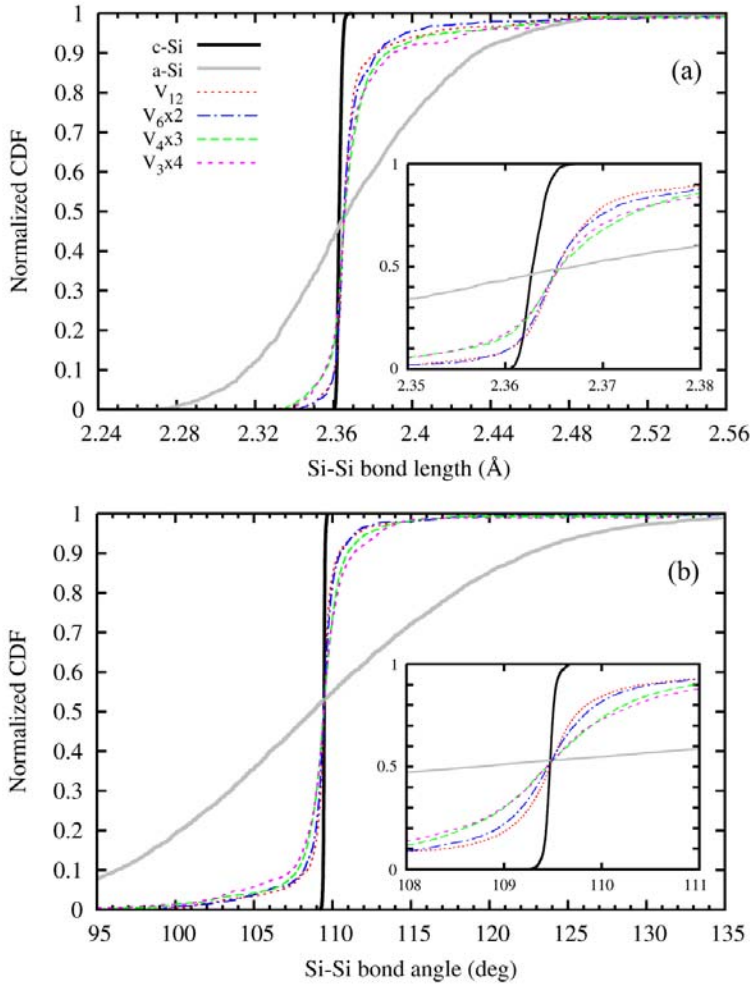

Figure 7.7: (Color available) Normalized cumulative distribution functions representing all bond lengths (a) and bond angles (b) in the constant-density, 968-atom supercells (V_{12}, V_6×2, V_4×3, and V_3×4) along with their 980-atom *c*-Si and *a*-Si references. For both (a) and (b), the insets illustrate the fine details differentiating the constant-density structural distributions, while their respective parent plots provide perspective.

Table 7.2: Summary of selected bond topology statistics compiled for various structures represented in 980-atom basis supercells. Strain energies are computed as formation energies referenced to *c*-Si and mass densities are given as ρ_m. Bond angle and bond length distribution statistics are computed comprehensively over the entire configuration represented in each supercell. Standard deviations and interquartile ranges are represented by σ and IQR, respectively.

Structure	N-n	Strain Energy	ρ_m	Bond Angle (deg)				Bond Length (Å)	
		(eV/atom)	(g/cm^3)	mean	σ	maximum	IQR	mean	σ
c-Si	980		2.296	109.47	0.06	109.69	0.06	2.363	0.001
a-Si	980	0.203	2.252	109.18	10.31	150.58	14.15	2.373	0.048
V_{12}	968	0.014	2.268	109.45	2.48	139.06	0.56	2.372	0.029
V_6×2	968	0.020	2.268	109.45	2.92	145.59	0.74	2.373	0.044
V_4×3	968	0.024	2.268	109.45	3.47	153.86	1.21	2.373	0.036
V_3×4	968	0.029	2.268	109.44	3.98	159.09	1.29	2.375	0.039
V_{32}	948	0.029	2.221	109.43	3.57	137.99	1.85	2.386	0.037

7.4.5 Bond-Length Contribution

Expecting to identify a relationship between bond length and optical absorption, the investigation continued by exploiting the unique structural manipulation of hydrostatic strain which provides a method to decouple the contributions of bond length and bond angle. Application of hydrostatic strain permits uniform variation of bond length throughout the structure while the bond angles remain constant. The conclusions of Idrobo *et al.* [145] show the Si-Si bond exhibits a universal optical response in the dominant spectral peak, regardless of bonding configuration. Here, their results are extended in Table 7.3 with $\varepsilon_2(\omega)$ calculations obtained via application of hydrostatic strain to 72-atom *c*-Si supercells. Increasing compression of the Si-Si bond corresponds to an increasing redshift in the E_0 transition energy, while the E_2 transition is simultaneously blueshifting and increasing in intensity. Since Si-Si bond elongation conversely modulates $\varepsilon_2(\omega)$ in ways that contribute to reduced absorption, it is possible that the enhanced absorption associated with the largely tensile nature of V_n is either driven by the minority compressive bonds or through the more elusive effect of bond angle variation. It is unfortunate that an analogous method of equivalent simplicity to

strictly control bond angle distribution is not readily available for a tetrahedrally-bonded network. The intermediate nature of topological disorder in constant-density $V_n \times q$ structures was compared to the broad, nearly-Gaussian distributions that characterize the bond topology of *a*-Si and the sharp distributions that define *c*-Si. Conceptually, the optical absorption spectra in a Si material of arbitrary morphology can be interpreted as the weighted superposition, or perhaps convolution, of all individual spectra representing the constituent bond lengths and angles in the system.

Table 7.3: Summary of Si-Si bond length influence on selected critical features of $\varepsilon_2(\omega)$ using hydrostatically-strained 72-atom *c*-Si supercells. The bond lengths shown represent averages at each strain condition, where the σ for each bond length distribution is $\sim 3 \times 10^{-4}$ Å and the average bond angle for each distribution is $109.47° \pm 0.01°$. E_2 peak intensities are normalized to the strain-free case.

hydrostatic strain %	Si-Si bond (Å)	E_0 transition (eV)	E_2 transition (eV)	E_2 intensity (normalized)
-5	2.245	0.42	4.04	1.102
-4	2.268	0.49	4.08	1.080
-3	2.292	0.56	3.92	1.085
-2	2.316	0.62	3.87	1.018
-1	2.339	0.68	3.80	1.004
0	2.363	0.74	3.75	1.000
1	2.387	0.79	3.72	0.992
2	2.410	0.83	3.67	0.987
3	2.434	0.87	3.63	0.938
4	2.457	0.90	3.58	0.907
5	2.481	0.93	3.52	0.892

7.5 Defect Concentration Effect in *c*-Si

In light of numerous recent endeavors [77,78,138] that have discussed the expected transparency of FC Si vacancy clusters, a plausible explanation was sought to justify the distinguishing optical signatures of FC vacancy clusters observed from DFT-GGA simulation results. Since the computational demands of this first-principles approach essentially restricts a feasible supercell size to approximately $N \leq 1 \times 10^3$, it is

usually prudent to estimate how DFT calculation results at the subnanometer scale will translate with system size as guidance for subsequent studies.

In Fig. 7.8, both $\alpha(\omega)$ and $\Xi(\omega)$ spectra are provided for a monovacancy embedded in a variety of supercell sizes (192, 256, 480, 576, and 980 atoms) to gauge the effect of concentration on the DFT results. In this case, V_1 was chosen, rather than a larger FC structure, to maximize the range of feasible basis supercell sizes. To accommodate the additional basis supercells, BZ sampling was increased to 4×4×4 meshes for the 192 and 256-atom basis supercells, while the 576-atom cell retained the 3×3×3 k-point mesh. Except for the 980-atom supercell, all cells used 750 conduction bands. No other changes were made to the previously detailed optical approach.

The utility of expressing $\alpha(\omega)$ in its cumulative form is immediately evident in comparison of Figs. 7.8(a) and 7.8(b). Inspection of $\alpha(\omega)$ spectra provides an impression that the absorption signal of V_1 is diluted with increasing supercell size, while $\Xi(\omega)$ is visually more effective at establishing the same trend. Since the dilution of the V_1 signal is sufficiently established over less than an order of magnitude change in basis supercell size ($192 \leq N \leq 980$), it is reasonable to conclude that concentration has a significant effect on the practical measurement of optical absorption. Consequently, it is possible to speculate from the simulated $\Xi(\omega)$ that a critical threshold V_n concentration is required to optically validate the presence of V_n clusters with experimental techniques and insufficient V_n concentration is a primary reason for the reported transparency of FC vacancy clusters.

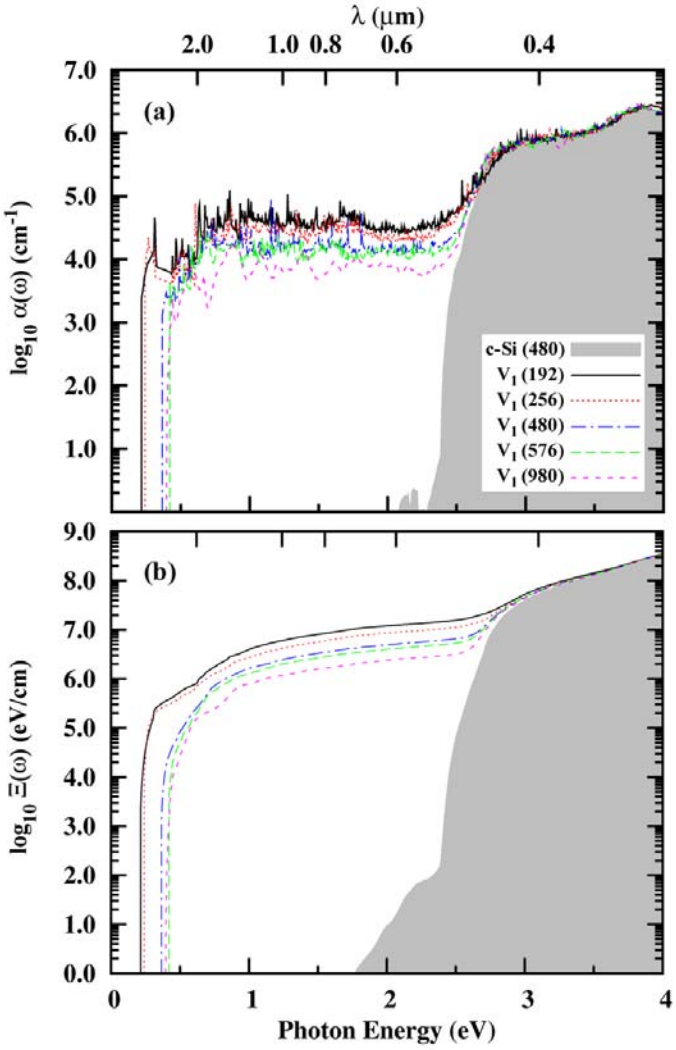

Figure 7.8: (Color available) Effect of concentration on (a) absorption coefficient spectra and (b) cumulative absorption coefficient spectra for a *c*-Si monovacancy. Each concentration is designated by the basis number of atoms in () for each supercell in the legend. In each plot, the gray-filled region represents the 480-atom *c*-Si reference spectra.

7.6 Density Effect in *a*-Si

In order to assess the contribution of atomic/mass density variation in optical absorption, the same optical computational procedure was applied to a set of five variable-density *a*-Si structures. Not surprisingly, application of volume relaxation to

each structure reduces the total range and incremental change in density covered by the resultant five-sample set, but previous simulation work [95] has shown this method to be most effective in reproduction of expected material properties.

One limitation of the current approach is that the density effect reported is specific to one type of morphology. Using the method described in Section 7.3 for supercell sizes where $N \leq 480$, the reduction in density generated is approximately uniform if the structural topology is extrapolated to larger size scales; however, note that experimentally-produced, low-density Si, such as *a*-Si [88,104] or porous Si (*p*-Si) [133,135,146], typically exhibits more heterogeneous morphologies in which lower density is often achieved from the contribution of large, open-volume voids.

In Table 7.4, the effect of density variation on $\varepsilon_2(\omega)$ is presented, which is rather minor for the density range investigated. The critical features of $\varepsilon_2(\omega)$ are provided, rather than the spectra, because the effect of density is sufficiently small such that all spectra appear nearly identical. A consistent reduction in E_2 peak intensity is observed as density decreases, as well as a less-distinguished trend for E_0 to redshift. The utility of the logarithmic scale for $\alpha(\omega)$ is used to resolve the small changes in optical response among the five variable-density *a*-Si structures in Fig. 7.9. Relative to the structural effect on optical absorption discussed in Section 7.4 and observed in Figs. 7.2, 7.3, and 7.5, the effect of density on optical absorption is secondary for the amorphous morphologies investigated. The main feature distinguishing the spectra in Fig. 7.9 is the transition energy for incipient absorption. Even this feature is actually structural in origin since the discontinuities observed in incipient absorption (similar to Fig. 7.3) are typical signatures [131] of highly-localized states (highly-strained or dangling bonds) contributing to tail absorption.

The insignificant effect of density in Fig. 7.9 is counterintuitive to classical optics principles, where application of the effective medium approximation [119] (EMA) to the large difference in dielectric constants between vacuum ($\varepsilon_o = 1$) and either *a*-Si ($\varepsilon_o \approx 16$) (Ref. 115) or *c*-Si ($\varepsilon_o = 11.9$) (Ref. 87) suggests an appreciable effect on optical absorption. However, as discussed by Banerjee *et al*. [147], voids (or vacancy clusters) that are significantly smaller than the wavelength of light, as is the case for all structures presented in this work, invalidate EMA and require computation of an effective $\alpha(\omega)$ comprehending both diffraction of light by nanocrystallites between the voids as well as Rayleigh scattering by the voids. Similar to the present work, this mathematical optical theory described by Banerjee *et al*. [147] predicts significant enhancement of the effective $\alpha(\omega)$ in thin *c*-Si layers by optimization of both nanovoid dimensions and distributions.

Table 7.4: Summary of variable-density *a*-Si sample structures. Structure names indicate the constituent number of Si atoms in each supercell. Strain energies are computed as formation energies referenced to *c*-Si, mass densities are given as ρ_m, and selected critical features of $\varepsilon_2(\omega)$ characterize the optical response of each structure. E_2 peak intensities are normalized to the basis *a*Si480 structure.

Structure	Strain Energy (eV/atom)	ρ_m (g/cm^3)	E_0 transition (eV)	E_2 transition (eV)	E_2 intensity (normalized)
a Si480	0.153	2.251	0.81	3.47	1.000
a Si468	0.158	2.245	0.75	3.23	0.999
a Si456	0.149	2.236	0.75	3.47	0.986
a Si444	0.159	2.226	0.61	3.24	0.974
a Si432	0.167	2.210	0.68	3.27	0.952

Despite the insignificant effect of density observed on the *a*-Si morphologies studied, further investigation is warranted on characteristic multiphase (voids interspersed in *a*-Si) *a*-Si morphologies. The density effect on absorption should be significant, but its importance is probably only relevant on larger length scales. Using simulation methods capable of handling tens of thousands of atoms would allow representation of large,

open-volume voids. For void dimensions comparable to the wavelength of light, a more significant effect of density is expected to be evident using EMA.

The results presented in this chapter suggest that incorporation of modest amounts of localized structural disorder in *c*-Si on a subnanometer scale is sufficient to provide optical absorption enhancement similar to that characteristic of *a*-Si. Based on these results, a more complete picture of optical absorption could be obtained with a multiscale study to better understand how both disorder and density contribute to optical absorption in Si. Furthermore, if the ability to precisely control V_n distributions and concentrations becomes feasible to an extent similar to modern control of Si dopant profiles, manipulation of V_n profiles could analogously provide a method to dictate Si absorption in a myriad of integrated optoelectronic and photovoltaic applications.

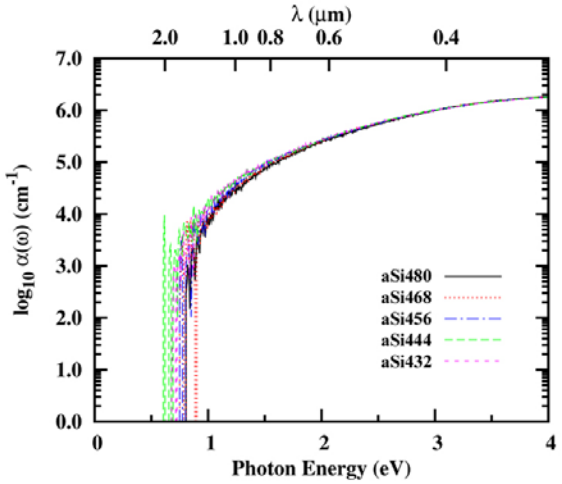

Figure 7.9: (Color available) Absorption coefficient spectra for the variable-density *a*-Si structure samples summarized in Table 7.4 computed from DFT-GGA calculations. Structure sample names indicate the constituent quantity of Si atoms present in each supercell.

7.7 Summary

To recapitulate, a DFT-based methodology is used to explore the structural contribution to optical absorption using charge-neutral, ground-state Si vacancy clusters

(V_n, $n \leq 6$, $n = 12$ and 32). An established PAW methodology based on computation of the longitudinal form of the dielectric matrix is utilized to calculate the imaginary and real parts of the complex dielectric function, $\varepsilon(\omega)$, and absorption coefficient, $\alpha(\omega)$. For small clusters (V_n, $n \leq 6$), a substantial redshift of ~2 eV is observed in the onset of incipient absorption as well as a magnitude of absorbance covering several orders of magnitude. The generality of these observations was validated by examining both $\varepsilon(\omega)$ and $\alpha(\omega)$ on larger, fourfold-coordinated (FC) clusters (V_{12} and V_{32}) and compared the resulting spectra to the well-known cases of both *a*-Si and *c*-Si. The optical spectra of V_{12} and V_{32} not only substantiated generality of optical absorption enhancement by smaller Si vacancy clusters, but remarkable similarities were also observed in the broad absorption envelopes of FC vacancy clusters when compared to *a*-Si.

To isolate the effects of topological disorder observed in absorption spectra from the density variation that accompanies vacancy incorporation, three additional 980-atom supercells ($V_6\times2$, $V_4\times3$, and $V_3\times4$) were constructed, each containing twelve vacancies, by dispersing different combinations of small FC clusters in each supercell. Together with V_{12}, this set of four constant-density ($V_n\times q$, $n\times q = 12$) vacancy structures provides a means to evaluate the impact of increasing structural disorder at a fixed density. Evaluation of the cumulative absorption coefficient spectra, $\Xi(\omega)$, of the constant-density $V_n\times q$ structures alongside *a*-Si and *c*-Si shows that increasing optical absorption follows a structural sequence of increasing V_n dispersion: $V_{12} < V_6\times2 < V_4\times3 < V_3\times4$. In addition, the simulation results suggest that $\Xi(\omega)$ of the $V_3\times4$ cluster dispersion exceeds that of *a*-Si up to about 1.5 eV. The structural disorder was characterized of each constant-density $V_n\times q$ bond topology by comparing cumulative distribution functions (CDFs) of bond lengths and angles with reference to both *a*-Si and *c*-Si, which revealed approximately symmetric distributions of bond angles around the *c*-Si mean (109.47°) as

well as the expected tensile nature of bond length distributions. More importantly, the constant-density CDFs also show increased spread across the same structural sequence ($V_{12} < V_6 \times 2 < V_4 \times 3 < V_3 \times 4$) which provides evidence for increased structural disorder (strain) as a driving force for optical absorption enhancement. Furthermore, hydrostatic strain was used as a convenient method to uniformly change bond length at constant bond angle to reveal that increasing bond compression correlates to a redshift of the E_0 transition, blueshift of the E_2 transition, and concomitant increase in the E_2 peak intensity.

For completeness, this simulation approach was extended to evaluate the effects of both defect concentration and density on optical absorption. The monovacancy was embedded in increasingly larger supercells (192, 256, 480, 576, and 980 atoms) to show a surprisingly strong concentration effect; extrapolation of these results provides sufficient doubt that FC clusters can be optically-resolved in bulk samples with modern instrumentation, which supports the difficulty reported in the literature in physical verification of small Si FC vacancy clusters. Using variable-density, void-free *a*-Si samples, the subnanometer-scale effect of density on optical absorption was observed to be secondary to the effect of structural disorder, contrary to expectations grounded in the effective medium approximation (EMA); however, this is justifiable since EMA is invalidated by subnanometer-scale clusters that are significantly smaller than the range of light wavelengths evaluated. The density effect is expected to be significant, but practical supercell sizes using first-principles methods are insufficient to describe typical variable-density, multiphase morphologies (voids interspersed in *a*-Si) that are routinely observed in experimentally-grown *a*-Si samples. Overall, these simulation results provide valuable insight into the fundamentals of subnanometer-scale optical absorption which indicates that increased structural disorder in *c*-Si via vacancy cluster incorporation constitutes a significant contribution to optical absorption in bulk Si.

Chapter 8

Optical Absorption Enhancement: Si Native Defect Clusters Under Biaxial Strain

8.1 Introduction

Improvement in the net efficiency of *c*-Si solar cells has been impeded by various intrinsic properties including low absorption over much of the solar spectrum and a band gap (E_g) precluding photogeneration of carriers over most of the infrared. Low optical absorption inflates solar module cost by requiring thick substrates (~100 μm) [87] and has consequently generated strong interest in derivative thin film materials, like *a*-Si:H [91], which significantly reduce the requisite substrate thickness (~1 μm) [87,89] through a serendipitous redshift of the absorption coefficient that accompanies the loss of long range crystalline order.

Optical methods [87], in general, provide an effective, non-destructive means to characterize subtle variations in semiconductors because optical properties are essentially determined by the electronic structure. It is well-established that variations in phase [89] and defect-content [131,132] of Si produce significant changes in the optical absorption spectra, which suggests the plausibility of defect engineering [148] the spectra through manipulation of atomic structure. While ambient temperature *c*-Si absorption [149] is negligible below the 1.11 eV experimental band gap [1], Si absorption at lower energies is attainable through the participation of band tail extended states (Urbach region) or at even lower energies in the presence of localized defects that create states near the Fermi level [131]. Localized defects include native defect clusters, which are commonly generated during ion implantation and crystal growth processes. The recent theoretical

work of Pan *et al*. [137] elucidates an atomistic topological relationship connecting short (long) Si-Si bonds with valence (conduction) band character in the electronic structure of *a*-Si, which suggests that control of internal strain distributions can influence optical absorption.

In this chapter, the first-principles prediction of enhanced Si optical absorption in the presence of structural disorder is extended based on the results of Chapter 7. Here, optical absorption is evaluated in the presence of native defects in which locally-generated strain fields are further modified by applied biaxial strain. In particular, optical spectra are calculated for the absorption coefficient, $\alpha(\omega)$, for previously-identified FC defect clusters comprised of four vacancies (V_4) and four interstitials (I_4) and further modification of the spectra is shown under applied biaxial strain. In addition, local density of states (LDOS) calculations are provided to describe the qualitative relationship between structural strain and optical absorption via modification of the electronic structure governing optical transitions. The majority of work presented in this chapter was recently submitted for publication [150].

8.2 Computational Details

The atomic configurations, electronic structures, and optical spectra reported in this chapter were calculated using a planewave pseudopotential method within the generalized gradient approximation of Perdew and Wang (GGA-PW91) [11] to DFT [66], as implemented in VASP [10]. The PAW methodology [14] was used to describe the interaction between ion cores and valence electrons. Kinetic energy cut-offs of 250 and 300 eV were used on the planewave basis set during ionic relaxation and for electronic calculations, respectively. BZ sampling was accomplished during ionic relaxation using one k-point (Γ) until residual forces had converged within 5×10^{-2} eV/Å tolerance. BZ sampling was increased to a 3×3×3 Monkhorst-Pack mesh for electronic

and optical calculations on the optimized structures. Transition energies were sampled up to 20 eV using 750 conduction bands and the four-step optical calculation procedure was ultimately capped by employment of the OPTICS code of Furthmüller [46] to compute the dielectric function, ε(ω). As previously detailed in Chapter 7, the absorption coefficient was subsequently computed from the dielectric function as

$$\alpha(\omega) = \frac{\sqrt{2}E}{\hbar}\left[\sqrt{\varepsilon_1^2(\omega) + \varepsilon_2^2(\omega)} - \varepsilon_1(\omega)\right]^{1/2}, \tag{7.1}$$

where E represents photon energy and $\hbar$ represents the reduced Planck's constant.

A DFT-optimized Si lattice constant (a_{Si}) of 5.457 Å along <100> or 3.859 Å along <110> was used to construct the strain-free Si supercell. Biaxial strain (±3%) was applied to supercells using the same approach detailed in Chapter 2. The upper panel of Fig. 8.1 indicates how the biaxial strain scheme is implemented in the crystallographic reference frame. Conditions of ±3% biaxial strain (tensile is defined to be positive) were chosen to best exemplify the results with maximum clarity (±1, ±2, and ±4% strain were also studied).

8.3 Modification of Optical Absorption Spectra

The V_4 and I_4 clusters will be used in this chapter to exemplify general FC cluster behavior. The embedded configurations of V_4 and I_4 are illustrated in Figs. 8.1(a) and (b), respectively. For each structure, the atom representing the highest strain energy (degeneracy creates additional candidates), as calculated using a Keating-type parameterization of the Si network [65], is annotated for discussion.

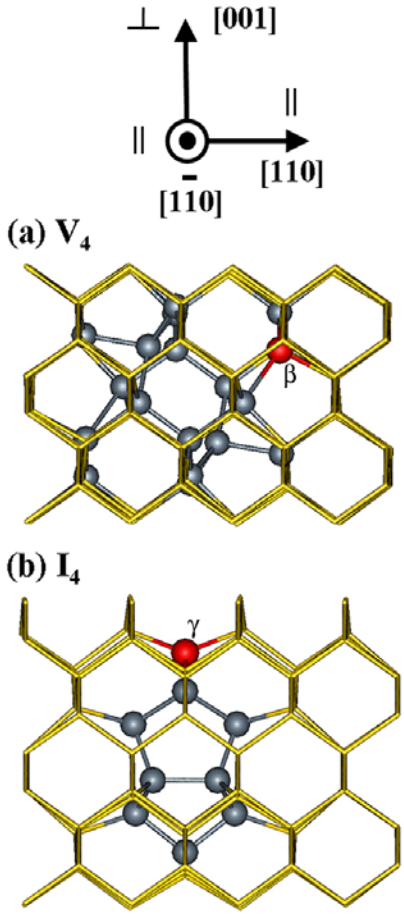

Figure 8.1: (Color available) Strain-free representations of V_4 (a) and I_4 (b) clusters shown embedded inside subsections of their respective 480-atom supercells. Light gray (gold) wireframe represents bulk Si atoms in the lattice. Dark gray spheres represent interstitial atoms comprising the cluster (I_4 only) as well as highly-strained atoms adjacent to the cluster cores (V_4 and I_4). The atoms representing the highest strain energy in each case (V_4, atom β; I_4, atom γ) are labeled and colored (red). The out-of-plane and in-plane directions for biaxial strain are depicted with the crystallographic axes.

Figure 8.2 shows the absorption coefficient as a function of both photon energy and wavelength for *c*-Si, V_4, and I_4 subjected to various biaxial strain conditions. Note that the absorption edge in the $\alpha(\omega)$ plots is modified from the fundamental band gap in two ways: (1) the indirect nature of Si precludes significant optical transitions from occurring at the 1.11 eV band gap, so significant transitions begin at higher energies

where the first direct transitions are possible [87] and (2) DFT E_g underestimation tends to reduce calculated direct transition energies. In Fig. 8.2(a), it is apparent that biaxial strain of either sign redshifts the onset of absorption (E_0 transition) [87], where the greater absorption enhancement is seen for the tensile case. Similar behavior was observed at other strain magnitudes (±1, ±2, and ±4%) and it was verified that the magnitude of redshift (enhancement) in absorption onset correlates with the applied strain magnitude. In Figs. 8.2(b) and (c), the inception of low-energy optical absorption is redshifted by nearly 2 eV in the presence of either FC native defect cluster embedded in strain-free Si. In Fig. 8.2(b), incipient absorption for strain-free V_4 occurs at 0.48 eV, which reduces to 0.23 (0.17) eV under 3% tensile (compressive) biaxial strain. Similarly, in Fig. 8.2(c), incipient absorption for strain-free I_4 occurs at 0.55 eV, which reduces to 0.37 (0.10) eV under 3% compressive (tensile) biaxial strain. Note that the observed optical response is complementary with respect to the structural strain configuration: V_n imparts a tensile local strain field on the surrounding lattice and is consequently stabilized by applied compressive conditions; likewise, I_n imparts a compressive local strain field on the surrounding lattice and is consequently stabilized by applied tensile conditions. These simulation results suggest that characteristic optical absorption in a perfect, bulk crystal can be modified through manipulation of the comprehensive strain field profile.

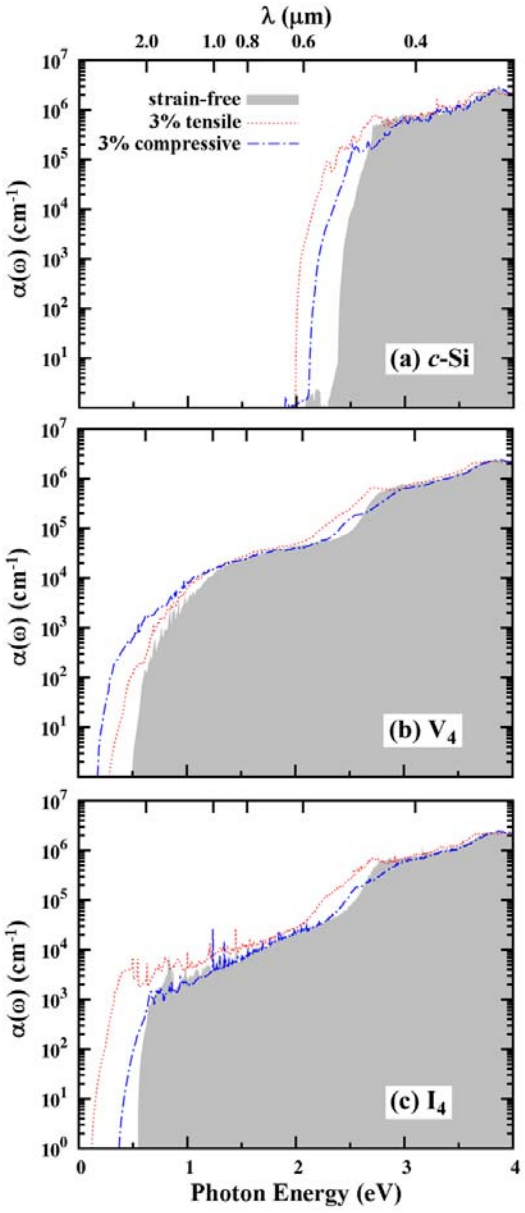

Figure 8.2: (Color available) Absorption coefficient spectra from DFT-GGA calculations for (a) *c*-Si, (b) V_4, and (c) I_4 structures using 480-atom supercells under various biaxial strain conditions. In each plot, the gray-filled region represents the reference $\alpha(\omega)$ for the strain-free structure.

8.4 Electronic Structure Signatures

To better understand the complementary behavior exhibited in optical absorption, the LDOS was examined for atoms selected through inspection of atomistic strain profiles of each structure. Searching for a potential structural connection to the observed absorption phenomena, the LDOS character was reviewed at the compressive and tensile extrema (atomic sites) for both clusters; however, a complementary LDOS relationship between dominant valence band (VB) and conduction band (CB) character was not readily apparent within the same structure using this approach. Instead, the investigation proceeded to analyze the effect of variable applied strain conditions on the atomic site representing the highest strain energy in each structure. These results are collectively presented in Fig. 8.3 for each case. The complementary LDOS behavior originally anticipated is present when the V_4 LDOS at atom β is compared to the I_4 LDOS at atom γ. Consistent with the results of Pan *et al*. [137], increased CB character is observed with the longer bonds associated with the locally-tensile strain field around V_4, while increased VB character is observed with the shorter bonds associated with the locally-compressive strain field around I_4.

Furthermore, evaluation of the LDOS dependence on applied strain for each structure reveals that the primary reason for increased optical absorption in each case is an effectively shrinking E_g that correlates with the observed redshifting trends in incipient absorption. For V_4, a prominent distribution of intermediate band (IB) states is also observed, which can be manipulated by strain, that can reduce the minimum energy required to absorb an incident photon and lower the effective E_g similar to studies of IB solar cell materials that rely on transition metal doping [43,151].

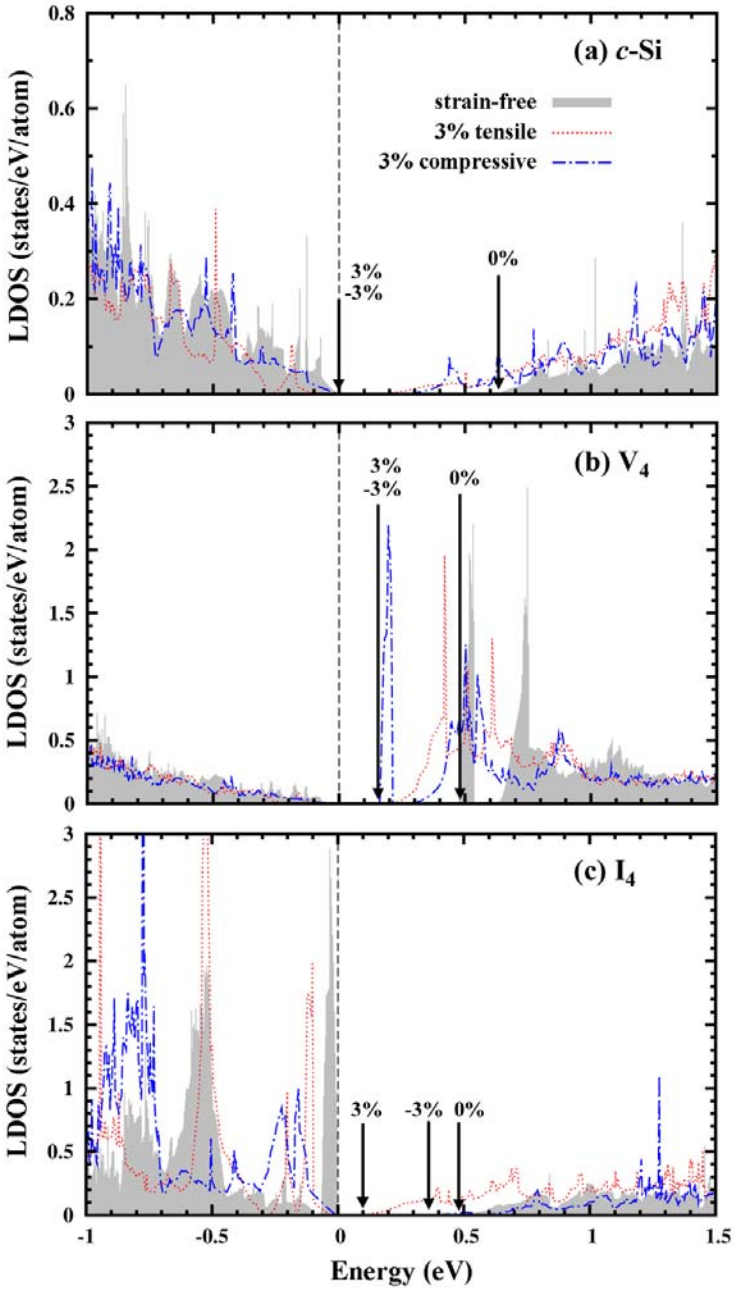

Figure 8.3: (Color available) Local density of states near the Si band gap for (a) *c*-Si, (b) V_4, and (c) I_4 projected onto respective atoms representing the highest strain energy for the clusters (V_4, atom β; I_4, atom γ) and an arbitrary atom for *c*-Si. In each plot, the gray-filled background spectra represents the reference LDOS under strain-free conditions. All LDOS spectra are referenced to their respective valence band maxima as indicated by dashed black reference lines and respective Fermi energies for each strain condition are indicated by vertical, black arrows.

8.5 Summary

In summary, the presented DFT calculations predict optical absorption enhancement (redshift) in *c*-Si in the presence of either vacancy (V_4) or interstitial (I_4) FC clusters that can be further enhanced by biaxial strain. While applied strain improves absorption in all cases studied (ε = -3, 0, and 3%), compressive strain exhibits the largest enhancement on V_4, while tensile strain exhibits the largest enhancement on I_4. LDOS examination of the most-strained atom in each structure reveals that the primary reason for increased absorption correlates with a decreased band gap, including an IB for V_4 under certain strain conditions.

Chapter 9

Property Predictions in Oxide-Sheathed Silicon Nanowires

9.1 Introduction

One-dimensional (1-D) nanostructures, such as silicon nanowires (SiNWs) and carbon nanotubes, have sustained intense interest because they exhibit unique, technologically-significant properties that are often substantially different from their bulk counterparts as a result of various nanoscale phenomena such as quantum confinement and enormous interfacial surface areas. In particular, recent studies of SiNWs have explored numerous effects on observable properties including orientation [152-157], passivation [153,158], diameter [152,154,159,160], cross-section (shape and aspect ratio) [152,158,161], doping [162,163], surface-to-volume ratio [152,161], strain [154,155,164], and surface morphologies [162,165]. The unrealized technological potential of SiNWs is vast, especially in devices already dominated by Si materials, and includes applications such as Si-process compatible optical interconnects and waveguides in CMOS integrated circuits [166], SiNW-based solar cell arrays with enhanced broadband optical absorption [129,167], and efficient three-dimensional anode architectures in Li-ion battery anodes [168].

Techniques to fabricate SiNWs include both bottom-up and top-down strategies [169]. The bottom-up approach is essentially 1-D crystal synthesis involving nucleation and subsequent epitaxial growth; the most common methods are vapor-liquid-solid (VLS) and oxide-assisted growth (OAG) mechanisms [170]. VLS-grown SiNWs typically suffer from residual metal catalyst contamination, like Au or Cu [170,171], that degrades

electronic properties. OAG SiNWs can be produced by either thermal evaporation [172-175] or laser ablation [160,174] of SiO_x in a growth mechanism involving phase separation into a recrystallizing Si (*c*-Si) core and amorphous silicon oxide (*a*-SiO_x, $0 \leq x \leq 2$) sheath that is proposed [160,174] to inhibit lateral growth. The preferred orientations of OAG SiNWs are <110> and <112>, where smaller diameters favor <112> [162,173]. The top-down approach is a subtractive process that relies on combinations of high-resolution microfabrication processes, such as lithography and etching, to define Si nanoscale columns on a bulk Si substrate.

While the desirable electronic properties of *a*-SiO_2 are arguably the primary reason for the immense proliferation of Si-based devices, accurate atomistic modeling of *a*-SiO_x materials and their interfaces is surprisingly limited. Tu and Tersoff [176] investigated improved models of the *c*-Si/*a*-SiO_2 interface using CRN-MMC simulations [16] that apply the bond switching moves of Wooten *et al.* [24] within the context of a Keating-like model [25] of force field energetics. A recent effort [15] extends the work of Tu and Tersoff [176] through parameterization of a Keating-like potential optimized with the aid of DFT calculations. Further extension of this structural model to the Si(001)/*a*-SiO_2 interface revealed the sensitivity of the interface structure to the relative rigidity of the parameterized potentials in each phase [23].

Despite this recent progress on the planar Si(001)/*a*-SiO_2 interface, nanostructure oxidation can be more complex, especially in generation of physically realistic structural models. Recent first-principles studies examining structural parameters [177], optical spectra [178], and conductance [179] in oxidized SiNWs have provided reasonable consistency with experiment, but these SiNW oxidation models are limited to specific O influences from either hydroxyls (-OH) or bridge-bonded/back-bonded O atoms on/near the NW surface. As evidenced by experimental studies of oxidation on SiNWs [180] and

Si nanocrystals (SiNCs) [181], nanoscale oxidation is more strongly influenced by certain structural parameters, including curvature and strain, than a macroscopic substrate surface, so accurate atomistic models are critical to improved understanding of nanostructure properties.

In this chapter, DFT calculations are used to investigate the dielectric function optical spectra and electronic structure of various SiNW orientations (<100>, <110>, <111>, and <112>) with -*a*SiO_x surface passivations and compare the results to H-terminated reference SiNWs. In addition, this same computational approach is extended to specifically examine both the chemical effects and disorder imposed by the passivation layer on <111> SiNWs using various functional groups (-H, -OH, and -F) and three different thicknesses of oxide sheath passivation. Average Seraphin coefficients are also computed for each <111> SiNW passivation to identify optical signatures for both functional group surface termination and surface oxidation. Most of the work presented in this chapter was recently submitted for publication [182].

9.2 Computational Details

The nanowire configurations, optical spectra, and electronic structure calculations presented in this chapter were all computed using a planewave pseudopotential approach within the generalized gradient approximation of Perdew and Wang (GGA-PW91) [11] to DFT [66], as implemented in VASP [10]. Vanderbilt-type US-PPs [13] were used to represent the interaction between ion cores and valence electrons for initial structural optimization and during volume relaxation of functionally-passivated (-H, -OH, and -F) SiNWs; PAW pseudopotentials [14] were employed for all optical and electronic calculations. The PAW methodology effectively comprises an all-electron frozen-core representation that describes exact valence wavefunctions; therefore, PAW pseudopotentials were employed to help ensure enhanced representations of electronic

transitions. Table 9.1 summarizes all kinetic energy cut-offs (E_{cut}), force-based ionic convergence criteria, and conduction bands simulated for each SiNW presented.

Table 9.1: Essential DFT conditions used for various SiNW structures. Cut-off energy values are first provided for structural optimization and in () when optimized ionic coordinates were fixed for optical and electronic calculations. Tolerances are given for force-based ionic convergence criteria. Conduction band values are first given for optical calculations and in () for electronic structure calculations.

SiNW	E_{cut} (eV)	tolerance ($\times 10^{-2}$ eV/Å)	conduction bands
<100>-H	160(250)	5	900(300)
<110>-H	160(250)	5	900(300)
<112>-H	160(250)	5	900(300)
<111>-H	160(250)	5	900(300)
<111>-OH	270(300)	7.5	1200(400)
<111>-F	273(250)	5	1200(400)
<100>-*a* SiO_x	270(300)	7.5	1200(400)
<110>-*a* SiO_x	270(300)	7.5	1200(400)
<112>-*a* SiO_x	270(300)	7.5	1200(400)
<111>-*a* SiO_x	270(300)	7.5	1200(400)
<111>-*a* SiO_x	270(300)	7.5	1200(400)
<111>-*a* SiO_x	270(300)	7.5	1200(400)

9.2.1 Nanowire Structure Generation

Reference SiNWs were first constructed by extracting sections of bulk *c*-Si with a DFT-optimized lattice constant of 5.460 Å followed by manual termination of surface dangling bonds with various functional groups (-H, -OH, and -F). Next, these configurations were DFT-relaxed with US-PPs using planewave basis sets and Γ-point Brillouin zone (BZ) sampling. In addition, each reference SiNW was then subjected to a volume relaxation procedure that effectively optimized the period along the wire axis (a_z). Table 9.2 provides key structural information about each SiNW including total number of atoms (N), atomic composition (N_{Si}, N_O, N_H, and N_F), transverse period

defining both *X* and *Y* supercell dimensions, and minimum vacuum spacing. Figures 9.1(a)-(d) and 9.2(a) and (b) illustrate all reference SiNW cross-sections generated with this procedure while also introducing a SiNW nomenclature used throughout this chapter of <hkl>-X, where <hkl> designates the wire orientation and -X represents the nanowire sheath composition. Figure 9.2 introduces a variety of surface passivations on <111> SiNWs for later discussion of passivation effects.

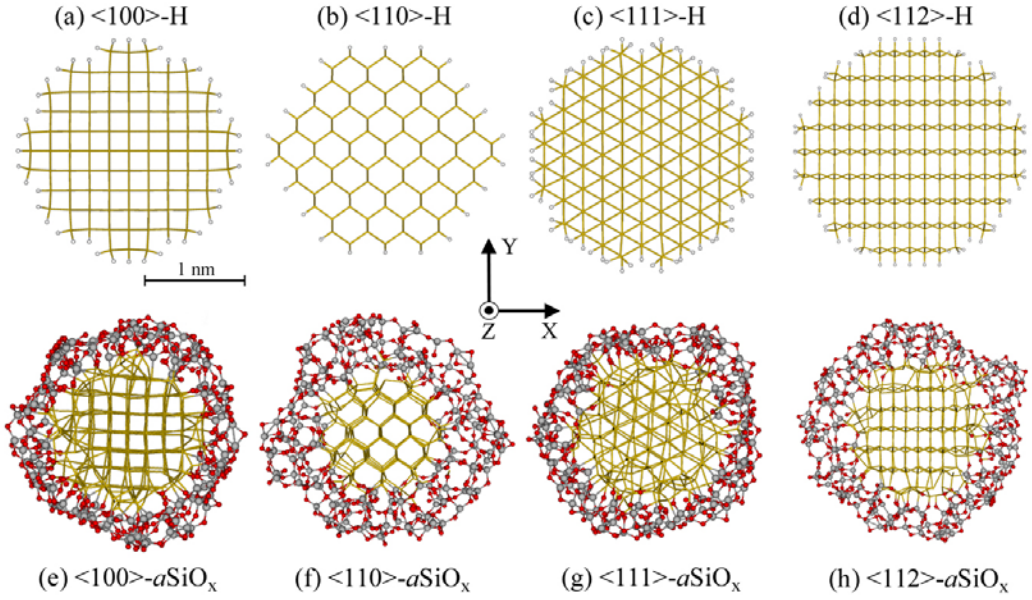

Figure 9.1: (Color available) DFT-relaxed configuration cross-sections for each SiNW orientation in both H-passivated (a)-(d) and corresponding oxidized (e)-(h) states. In all cases, the wire axis is aligned in the *Z* direction. Small white spheres represent H atoms. Gold wireframe depicts all Si atoms in (a)-(d), while in (e)-(h) wireframe represents only *c*-Si core atoms in neutral, +1, or +2 oxidation states. In the -*a*SiO_x sheaths, gray spheres represent Si atoms in +3 and +4 oxidation states, while medium red spheres represent O atoms. The measurement bar is scaled specifically for (a), but still provides approximate perspective for all structures shown.

Four independent oxidized SiNWs for each orientation and/or oxide thickness of interest were generated from the same *c*-Si cores as previously described. Instead of Si dangling bond surface termination with functional groups, -*a*SiO_x layers were generated

on lateral surface facets by strategically inserting O atoms in between surface Si-Si bonds. Then, amorphization of the oxide sheath layers was implemented using a customized derivative procedure described in concurrent work [23] which is based on CRN-MMC simulations using an optimized *a*-SiO_x potential [15]. This *a*-SiO_x potential is based on *ab initio* parameterization of a valence force field model that improves structural description of partial phase separation and mechanical properties that are experimentally observed near strained *c*-Si/*a*-SiO_2 interfaces. The size (*N*) of each oxidized SiNW (-*a*SiO_x) studied was determined as a balance between sufficient supercell size and adequate wire length (=$Z_n \times a_z$, where Z_n is number of periods along the Z axis) to allow generation of a reasonably random amorphous layer while still being sufficiently small to practically facilitate DFT simulation. In addition, preservation of some crystallinity was intended in the SiNW cores, so this objective imposed additional constraints on the oxide thicknesses that could be accommodated. As shown in Fig. 9.1, all SiNWs generated have diameters of approximately 2 to 3 nm.

Following simulated amorphizations to generate the -*a*SiO_x sheath layers, these intermediate configurations were also DFT-relaxed with US-PPs and Γ-point BZ sampling. From evaluation of the resultant DFT total energies, the lowest energy structure was selected from each four-sample set as the representative structure for subsequent property calculations. These representative oxidized SiNWs are illustrated in Figs. 9.1(e)-(h) and 9.2(c) and (d). Table 9.3 provides a brief summary of the suboxide distribution for each oxidized SiNW. The minimum measured vacuum separation for any SiNW in this study is 8.44 Å (<112>-*a*SiO_x).

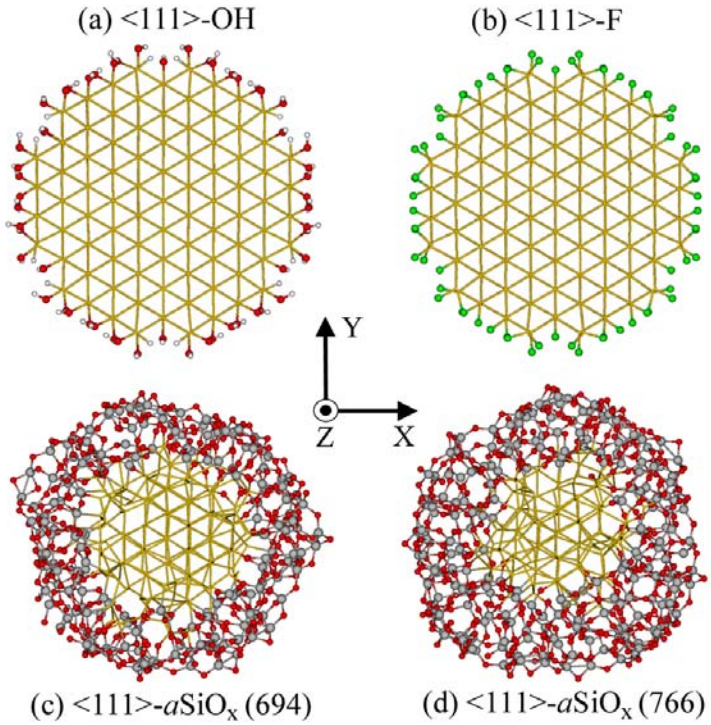

Figure 9.2: (Color available) DFT-relaxed configuration cross-sections for additional surface passivations on <111> SiNWs as viewed along the *Z* axis. Small white spheres represent H, medium red spheres represent O, and green spheres represent F. Gold wireframe depicts all Si atoms in (a) and (b), while in (c) and (d) wireframe represents only *c*-Si core atoms in neutral, +1, or +2 oxidation states. In the -*a*SiO_x sheaths, gray spheres represent Si atoms in +3 and +4 oxidation states. To prevent steric hindrance between -OH groups at 24 surface sites between the six main {110} lateral facets in (a), these sites remained -H passivated, rather than -OH passivated.

Preliminary calculations showed that SiNW total energies were well-converged when vacuum separation ≥ 3 Å. Unlike the reference SiNWs, structure-specific volume relaxation was not found effective in lowering the energy of oxidized SiNWs, so this step was omitted in the generation of optimized structural configurations for property calculations. Surrounded by an annular, interconnected -*a*SiO_x sheath, the dimensions of the crystalline SiNW core are highly-constrained relative to its reference SiNW counterpart in which surface passivation with terminal (no interconnections) functional

groups should be more flexible. This result is not surprising in the context of parallel work [23] which shows that the oxide model produced by the DFT-parameterized *a*-SiO_x potential [15] has a significant influence on the *c*-Si/*a*-SiO_2 interface structure that is driven by respective strain energies of the two phases and their relative rigidity.

Table 9.2: Structural summary of various SiNW models detailing atomic compositions, number of supercell axial periods (Z_n), axial lattice constants (a_z), transverse periods defining *X* and *Y* supercell dimensions, and minimum lateral vacuum spacing.

SiNW	N	N_{Si}	N_O	N_H/N_F	Z_n	a_z (Å)	*X,Y* period (Å)	min. vacuum (Å)
<100>-H	532	356		176	4	5.452	32	10.19
<110>-H	432	320		112	4	3.868	36	10.41
<112>-H	552	420		132	2	6.680	40	10.56
<111>-H	472	340		132	2	9.437	33	10.72
<111>-OH	580	340	108[a]	132	2	9.431	33	9.32
<111>-F	472	340		132	2	9.445	31	8.81
<100>-*a* SiO_x	652	356	296		4	5.256	35	10.92
<110>-*a* SiO_x	664	320	344		4	3.869	40	10.46
<112>-*a* SiO_x	800	420	380		2	6.579	42	8.44
<111>-*a* SiO_x	622	340	282		2	9.105	35	9.24
<111>-*a* SiO_x	694	340	354		2	9.547	35	8.89
<111>-*a* SiO_x	766	340	426		2	9.509	37	10.70

[a] To avoid steric hindrance between some -OH groups, 24 surface sites remained -H passivated.

Table 9.3: Overall suboxide distributions for various oxide-sheathed SiNW structures. For the <111> orientation, three different oxide thicknesses are provided.

wire orientation	N	N_{Si}	Si oxidation state				
			0	+1	+2	+3	+4
<100>	652	356	0.46	0.10	0.05	0.11	0.29
<110>	664	320	0.37	0.05	0.04	0.13	0.41
<112>	800	420	0.45	0.06	0.06	0.10	0.34
<111>	622	340	0.47	0.08	0.06	0.10	0.29
<111>	694	340	0.37	0.07	0.04	0.14	0.38
<111>	766	340	0.29	0.04	0.05	0.15	0.48

9.2.2 Optical Calculations

A four-step procedure was employed in all optical calculations to calculate $\varepsilon(\omega)$. First, the ionic configuration of each SiNW was optimized with PAW pseudopotentials and Γ-point BZ sampling using the conditions shown in Table 9.1. Second, the charge density distribution was determined with the BZ sampling increased to a 1×1×10 Γ-centered mesh [10] which results in six k-points in the irreducible BZ along the axis for all SiNWs. Third, the frequency-dependent dielectric matrix was determined from the optimized charge density distribution with the tetrahedron method [10] and an adequate number of conduction bands (see Table 9.1) that was adjusted according to surface passivation. Fourth, the OPTICS code of Furthmüller [46] was employed to obtain both the imaginary part (ε_2) of $\varepsilon(\omega)$ by sampling optical transitions up to 20 eV and compute the real part (ε_1) through application of the Kramers-Kronig transformation.

9.2.3 Electronic Structure Calculations

Band structure and DOS calculations started from the charge density distributions previously determined during calculation of $\varepsilon(\omega)$. For each SiNW, the energy dispersion relationship was evaluated along the wire axis using 30 k-points along a line from Γ to Z, where Z is Π/a_z along an arbitrary wire axis to the BZ edge. Since electronic structure is only presented in the band gap proximity, the number of conduction bands included for both band structure and DOS calculations was reduced to 1/3 of the value used for optical calculations as summarized in Table 9.1. For DOS calculations, the same 1×1×10 k-point mesh employed for optical calculations was used.

9.3 Si Nanowire (SiNW) Orientations

Guided by the results of previous theoretical studies [152,153,156,157] and reports of commonly synthesized SiNWs [160,173,174], this investigation focused on

four SiNW orientations: <100>, <110>, <111>, and <112>. As-grown SiNWs are often sheathed in passivating oxide layers, either from evolution of a native oxide [183], intentional growth via subsequent thermal oxidation [180], or remnant from NW synthesis (OAG) [160,172,174,175]; consequently, this motivated application of the *a*-SiO_x structural modeling procedure [15,23] with DFT-parameterized potentials to commonly studied SiNWs to determine the influence of oxidation on observable properties.

9.3.1 Optical Absorption Spectra

For all optical calculations, the four-step procedure described in Chapter 2 was utilized to compute $\varepsilon(\omega) = \varepsilon_1(\omega) + i\varepsilon_2(\omega)$ with VASP following the general theoretical framework described by Adolph *et al.* [41] Additional details about this procedure and its limitations are discussed in Chapter 2.

The study of 1-D periodic systems naturally results in the application of supercells with tetragonal symmetry where two independent components of ε_2 exist [153]. As a result, both components of ε_2 will be presented for all optical spectra: (1) parallel to the wire axis, the ε_2 tensor reduces to $\varepsilon_{zz}(\omega) = \varepsilon_2^{\parallel}(\omega)$ and (2) perpendicular to the wire axis, ε_2 reduces to two identical components that will be represented as an average, $[\varepsilon_{xx}(\omega)+\varepsilon_{yy}(\omega)]/2 = \varepsilon_2^{\perp}(\omega)$.

Figure 9.3 introduces both $\varepsilon_2^{\parallel}(\omega)$ and $\varepsilon_2^{\perp}(\omega)$ spectral components for all four SiNW orientations representing all structures depicted in Fig. 9.1. Similar to the results of Aradi *et al.* [153], a blueshift is seen in the fundamental absorption edge (E_0 transition in Si) of all $\varepsilon_2^{\perp}(\omega)$ components relative to $\varepsilon_2^{\parallel}(\omega)$ for all orientations and surface passivations (-H and -*a*SiO_x). Since the SiNWs presented here have larger diameters than those of Aradi *et al.*, the degree of shift observed in the present work is generally smaller because the quantum confinement (QC) effect on the $\perp$ components is diminished.

Based on a previous report [184], the perceived reduction in anisotropy with reduced QC is a misleading conclusion that arises from approximations made in sampling optical transitions. Bruneval *et al.* [184] made the critical observation that the approximations in this established optical calculation method [41], especially in neglecting local field (LF) effects, do not allow accurate description of anisotropy at this scale. Bruneval *et al.* further demonstrated that first-principles calculations including LF effects and classical estimations based on effective medium theory indicate that optical anisotropy remains even while QC effects are vanishing.

As anticipated, growth of the -*a*SiO_x surface layer on all SiNW orientations has an appreciable and consistent effect on $\varepsilon_2(\omega)$. For all cases in Fig. 9.3, the -*a*SiO_x passivation diminishes the main absorption peak (E_2 transition in Si) near 4 eV relative to the -H reference NWs and also washes out most characteristic *c*-Si transition edges and peaks. Since the growth of the -*a*SiO_x layer results in a two-phase nanostructure, the optical spectra consequently represent a weighted hybrid of both distorted *c*-Si and *a*-SiO_x responses. The growth of the -*a*SiO_x surface layer creates strain in the *c*-Si NW cores and disorder at the *c*-Si/*a*-SiO_x interface that can be viewed as incipient amorphization of the *c*-Si core; despite this, the remnant E_2 Si peak remains. The other $\varepsilon_2(\omega)$ contribution from the oxide phase is represented by the long tails present for all -*a*SiO_x SiNW orientations that gently rise to almost imperceptible peaks near 10 eV, consistent with previous results for SiO_2 optical response (see Figs. 5 and 6 in Ref. 95). Despite significant residual crystallinity visually apparent in the core of each -*a*SiO_x SiNW [see Fig. 9.1(e)-(h)], these optical spectra reinforce the acute sensitivity of optical techniques in semiconductor characterization [87,144,165].

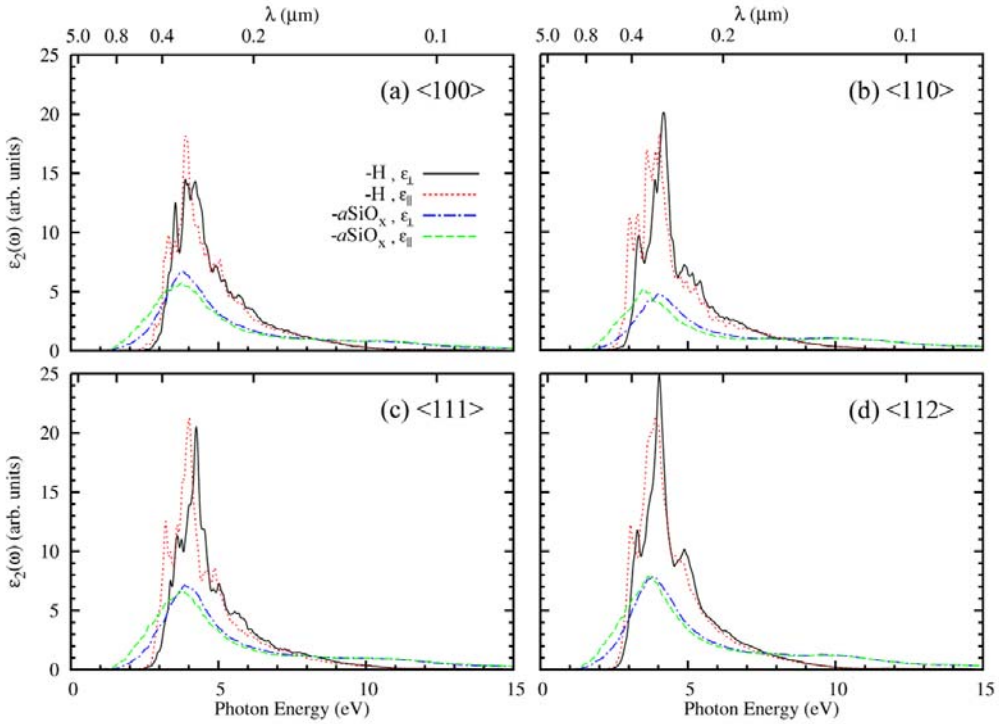

Figure 9.3: (Color available) Imaginary components of the complex dielectric function spectra computed from DFT-GGA calculations for all SiNW configurations in Fig. 9.1. Within each subfigure, the ε_2 components are provided both parallel ($\varepsilon_2^{\parallel}$) and perpendicular ($\varepsilon_2^{\perp}$) to each wire axis.

9.3.2 Electronic Structure

In Fig. 9.4, band structure and total density of states (DOS) are provided for all nanowires represented in Fig. 9.1. The band structures exhibited by the -H SiNWs are found to be qualitatively consistent with results in the literature; however, the relatively larger [153,156,157,158] -H reference SiNWs investigated here (E_g scales down with increasing diameter) and the various functionals [153,154,158] and E_g corrections [156,157] employed in other studies understandably impart some quantitative variations. Direct gaps are observed for both <100>-H and <110>-H, while <111>-H and <112>-H exhibit indirect gaps. Similar to the work of Scheel *et al.* [157], the E_g direct nature,

essential for photonic applications, of <110>-H is found to be dampened by a low population of states near the gap which effectively nullifies the direct gap character for device operation.

The most interesting aspect of the present band structure results lies in comparison of each reference SiNW [Figs. 9.4(a)-(d)] with its corresponding oxidized SiNW [Figs. 9.4(e)-(h)]. For all wire orientations, it is readily apparent that the usual energy dispersions with respect to **k** are averaged and flattened out with the growth of the -*a*SiO_x layer relative to the reference SiNWs. This result is attributed to the disorder imposed on the SiNW cores as a result of their close proximity to the *c*-Si/*a*-SiO_x interface since the band structure observed on the oxidized SiNWs is similar to what might be expected at the onset of amorphization. As the configuration approaches complete amorphization, all remnant band structure should disappear as **k** becomes undefined. For the case of <100>-*a*SiO_x [Fig. 9.4(e)], the band structure has almost reduced to an elaborate, but redundant, plot of band gap states as a result of the flat nature and high density of bands present. Note that this is also partially a function of the <100>-H band structure since the energy dispersions along the bottom of the conduction band and top of the valence band are inherently subtle in this orientation. In other cases, such as the <110> and <111> SiNWs, the oxidized SiNW band structure is more easily seen as a k-averaged counterpart of the corresponding –H SiNW band structure.

Another interesting consequence of the evolution of SiNW disorder in the core is the effect on the direct/indirect nature of the band gap. Previous studies [154,155,164] have examined the effect of applied strain on both the magnitude and nature of the SiNW E_g, including reports [155] that specific strain conditions can change the nature of the gap. Other studies [177,178] have also provided insight into the effect of O incorporation on QC in SiNCs. As Ramos *et al.* report [178], the effect of O incorporation is

complicated by competing effects. On one hand, oxidation of the surface increases the nanostructure diameter, which reduces QC and E_g; however, O incorporation via backbond oxidation effectively reduces the *c*-Si core, which increases QC and E_g. The growth of amorphous oxide layers on SiNWs introduces an additional structural influence that promotes averaging of **k** in the band structure which can shift the k-point coordinate of both conduction band minima (CBM) and valence band maxima (VBM).

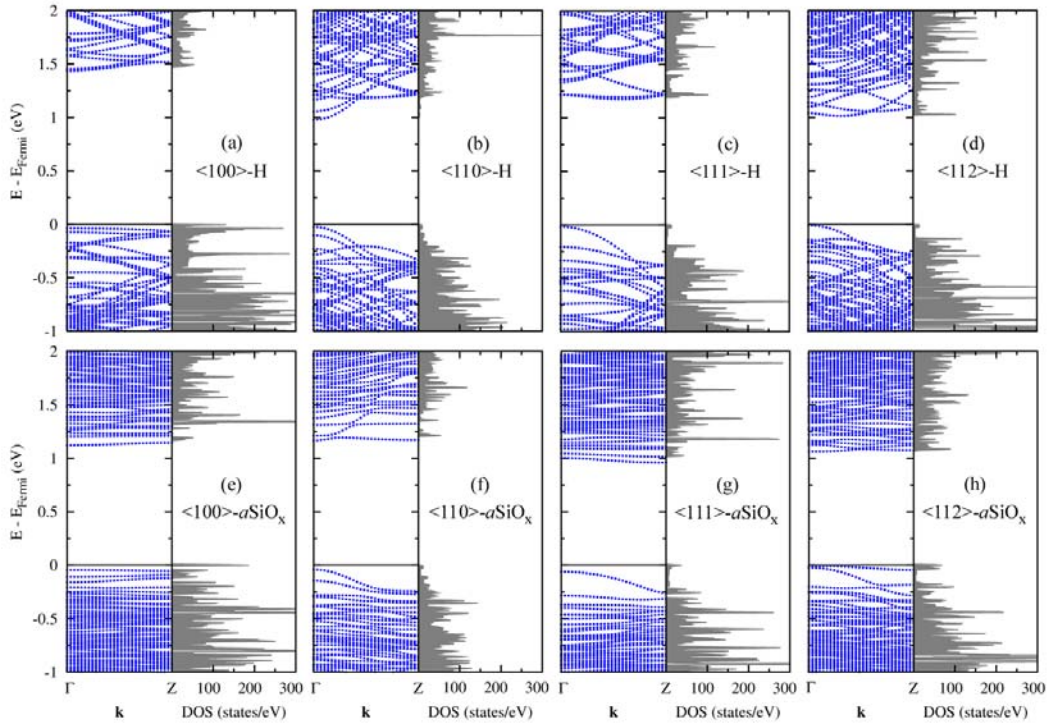

Figure 9.4: (Color available) Band structure and total DOS computed from DFT-GGA calculations for each SiNW configuration shown in Fig. 9.1. The top panels represent -H reference SiNWs, while the corresponding bottom panels represent the oxidized SiNW for each orientation. Reference Fermi energies for band structures are computed during determination of the charge density distribution. Some variation in energy referencing between band structure and DOS calculations is an inevitable consequence of different k-point sampling schemes.

As a result of these competing oxidation effects, different band structure changes are observed from SiNW oxidation. In Fig. 9.4, the magnitude of E_g is seen to shrink for <100> and <111>-oriented SiNWs, while E_g increases for both the <110> and <112> cases. Analyzing Fig. 9.4 in terms of SiNW gap character, the k-averaging effect of oxidation on the CBM around Γ almost destroys the strongly direct appearance of the <110> SiNW E_g [Fig. 9.4(b) and (f)]. However, comparison of the <112> SiNWs [Fig. 9.4(d) and (h)] indicates oxidation of the surface has changed the nature of the gap from indirect to a weakly direct character since k-averaging has moved the k-point coordinate of CBM to Γ.

9.4 <111> SiNW Surface Passivations

To better understand the effect of various surface passivations, the commonly synthesized <111> wire orientation was chosen for further examination. Figures 9.1(c) and (g) and 9.2 collectively illustrate three functional group (-H, -OH, and -F) passivations to assess chemical effects as well as three different thicknesses of oxide sheath passivation (622-, 694-, and 766-atom <111>-aSiO$_x$) to study the expected effects of variable oxide thickness. In particular, the functional groups provide a basis for comparison of electronegativity (EN) influence. On the Pauling scale, the EN values of the relevant elements are 1.9, 2.2, 3.4, and 4.0 for Si, H, O, and F, respectively [97]. For the -aSiO$_x$ passivations, it is expected that variation in interface composition (suboxide distribution) and degree of strain/disorder imparted on the c-Si core will be observed with increasing oxide thickness. Revisiting Table 9.3, the suboxide (Si^{1+}, Si^{2+}, Si^{3+}) fraction of Si atoms is seen to remain nearly constant at ~0.25 for <111> SiNWs; however, the nature of the interface changes with increasing oxide thickness because the Si^{3+} population is increasing at the expense of the Si^{1+} population.

9.4.1 Optical Absorption Spectra

Figure 9.5 extends the results shown in Fig. 9.3(c) with separate plots for $\varepsilon_2^{\parallel}$ and $\varepsilon_2^{\perp}$ that show the influence of surface passivation on the optical spectra. Using <111>-H as the base reference, substitution of -H with either -OH or -F has a similar effect on both components of ε_2. Substitution with -F reduces and redshifts the E_2 peak and also redshifts E_0; substitution with -OH further reduces E_2 peak intensity and shows a similar redshift in both E_2 and E_0 as observed for the -F case. The E_1 peak (between E_0 and E_2) is particularly apparent in $\varepsilon_2^{\parallel}$ for the three cases of surface termination with functional groups. For <111>-H, the $E_1^{\parallel}$ transition occurs at 3.22 eV; however, substitution with either -F or -OH redshifts the $E_1^{\parallel}$ peak to 2.97 and 3.03 eV, respectively. While the $E_1^{\perp}$ peak is evident for the -H case in $\varepsilon_2^{\perp}$, the $E_1^{\perp}$ peak is no longer apparent for -OH and -F passivations. Furthermore, substitution of -H with either -OH or -F also increases the high energy tail (> 10 eV) in both $\varepsilon_2^{\parallel}$ and $\varepsilon_2^{\perp}$ spectra. Aradi *et al.* [153] observed similar redshifting of E_0 on both <110> and <112> SiNWs when -H passivation was substituted with -OH passivation which they attributed to reduced band gaps from the high EN (3.4) of O in the -OH groups.

For the <111>-*a*SiO_x SiNWs, the expected results are observed in Fig. 9.5 for both ε_2 components of Si E_2 peak intensity reduction and broadening in correlation with increased oxide thickness. This optical response is not only characteristic of amorphization [95,139], but is also a signature of stoichiometric shift in bulk *a*-SiO_x ($0 \leq x \leq 2$) as x increases [95]. If the oxide contribution in these SiNWs were increased following further oxidation, observation of a blueshift would be expected in the E_2 peak (see Fig. 5 in Ref. 95). In addition, closer inspection of Fig. 9.5(b) via the inset shows that the main characteristic SiO_2 $\varepsilon_2(\omega)$ peak near 10 eV increases as the oxide sheath thickness increases.

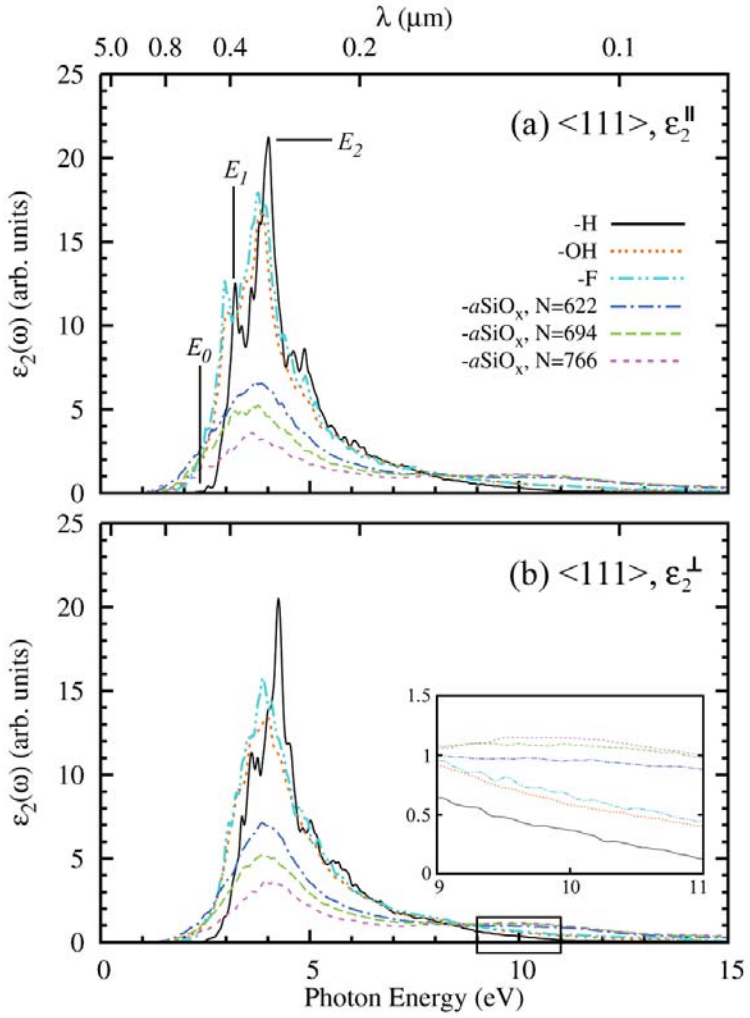

Figure 9.5: (Color available) (a) Parallel and (b) perpendicular components of the imaginary parts of the complex dielectric function spectra computed from DFT-GGA calculations for all <111> SiNW passivations. The optical transitions annotated in (a) for <111>-H follow the nomenclature of Yu and Cardona (Ref. 87). The tail spectra magnified in the inset in (b) has the same trend for (a) and is therefore omitted in (a).

9.4.2 Electronic Structure

Figure 9.6 extends the results in Fig. 9.4 with a comparison of <111> SiNW band structures resulting from all six surface passivations. Substitution of -H with -OH [Fig. 9.6(b)] has modest implications on the band structure; the most obvious effect is simply

an increase in band density that is also reflected as a general rise in DOS. Substitution of -OH with -F [Fig. 9.6(c)] results in few modifications in the electronic structure. In contrast, the effects of increasing oxidation on the <111> SiNW are more interesting [see Figs. 9.6(d)-(f)]. The degree of disorder present for the N=766 case was expected to fully average out any remaining dispersion in the band structure, but this is not observed. Increased oxidation among the three <111>-aSiO$_x$ cases (N = 622, 694, and 766 atoms) has the general effect of making the DOS increasingly sparse and more discontinuous with respect to energy. The increasingly sparse nature of near-gap states is a consequence of complete Si oxidation. While Si^0 and the suboxide states contribute to near-gap electronic structure, the influence of Si^{4+} is farther removed (E_g for SiO_2 ~ 9 eV (Ref. 185)).

Interestingly, the gap for N=694 becomes weakly direct after oxidation, although the sparse DOS in the CB precludes applicability to photonic devices and nearly flat CBs correspond to large electron effective masses. While oxidation is observed to be capable of changing the direct/indirect nature of the gap in Figs. 9.6(d)-(f), it is possible to speculate that a statistical sampling of oxidized SiNWs would reveal that the random nature of -aSiO$_x$ yields mixed distributions of direct/indirect SiNWs for each oxide thickness. It appears that oxidation-induced disorder is responsible for changing the direct/indirect nature of the gap; however, oxidation may not be a reliable tool to augment gap character because the random aspect of k-averaging will likely make the direction of change hard to control.

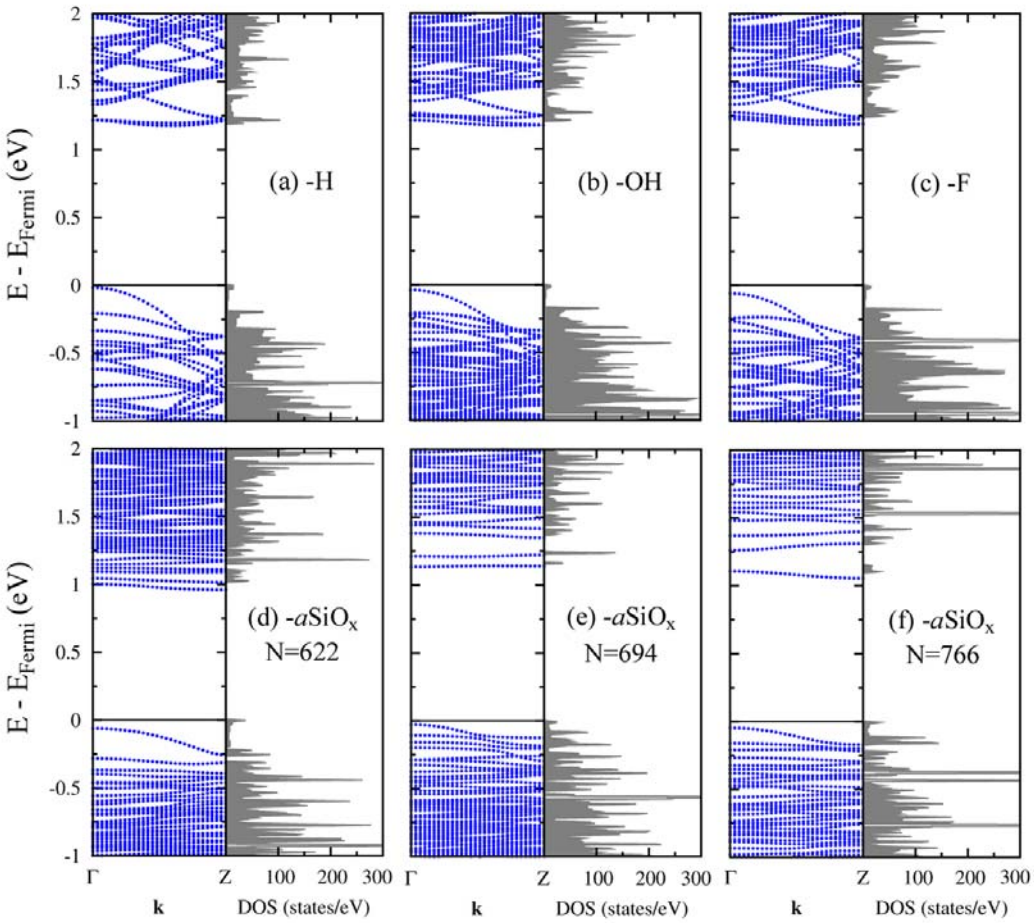

Figure 9.6: (Color available) Band structure and total DOS computed from DFT-GGA calculations for all <111> SiNW passivations. The top panels represent SiNWs passivated with functional groups, while the bottom panels represent the effect of increasing oxidation from left to right. Reference Fermi energies for band structures are computed during determination of the charge density distribution. Some variation in energy referencing between band structure and DOS calculations is an inevitable consequence of different k-point sampling schemes.

Carrier *et al.* [185] studied Si/SiO_2 superlattice interfaces to reach the conclusion that the suboxide is responsible for the nearly dispersionless (k-invariant) bands; however, since the oxide is simultaneously responsible for both suboxide influence (Si charge states) and imposition of disorder in the *c*-Si phase, the relative contribution of

each effect remains to be determined. Note that -OH passivation [Fig. 9.6(b)] produces a near-surface population of Si^{1+}, yet the band structure is hardly dispersionless.

9.4.3 Optical Characterization: Seraphin Coefficients

Previous reports [144,186] used Seraphin coefficients to optically characterize the structure of bulk semiconductors and heterostructures based on the original work of Seraphin and Bottka [187]. Optical calculation techniques will be exercised to help illuminate the relationship between the atomic structure of differently passivated SiNWs and the response of Seraphin coefficients with specific attention given to the contributions of the suboxide layer and structural disorder from oxide passivations.

Experimental studies based on Seraphin coefficients [187] use various modulation spectroscopies [188] to structurally characterize Si, such as determination of intrinsic interface strain [186] and disorder [144]. Similarly, the method described by Sundari *et al.* [144] will be employed here since all necessary quantities are extracted from $\varepsilon(\omega)$ for an arbitrary material, which is typically a semiconductor. The ratio of change in reflectivity (ΔR) to absolute reflectivity (R) is calculated as

$$\Delta R/R = \alpha\Delta\varepsilon_1 + \beta\Delta\varepsilon_2, \tag{9.1}$$

where $\Delta\varepsilon_1$ and $\Delta\varepsilon_2$ are changes in respective components of the complex dielectric function, $\alpha = 2A/(A^2+B^2)$, $\beta = 2B/(A^2+B^2)$, $A = n(n^2 - 3k^2 - 1)$, and $B = k(3n^2 - k^2 - 1)$. The frequency-dependent quantities, α and β, are the Seraphin coefficients [187] and n and k are the real and imaginary parts [189], respectively, of the complex refractive index:

$$n(\omega) = \left[\frac{\sqrt{\varepsilon_1^2(\omega) + \varepsilon_2^2(\omega)} + \varepsilon_1(\omega)}{2} \right]^{1/2}, \tag{9.2}$$

$$k(\omega) = \left[\frac{\sqrt{\varepsilon_1^2(\omega) + \varepsilon_2^2(\omega)} - \varepsilon_1(\omega)}{2} \right]^{1/2}. \tag{9.3}$$

The work of Sundari *et al.* shows that determining the frequency or energy ($E=\hbar\omega$) of intersection between α and β, which they denote as the crossover energy (E_c), can be used as a reliable method to quantify bulk Si structural disorder.

In Fig. 9.7, α and β (derived from both || and ⊥ components of calculated ε(ω)) for the various investigated surface passivations of <111> SiNWs are plotted on an energy spectrum. Figure 9.8 is also provided as a reference to illustrate the behavior of α and β strictly for changes in phase and composition for the relevant bulk structures of *c*-Si, *c*-SiO_2, and *a*-SiO_x (x = 0, 0.5, 1.0, 1.5, and 2.0). In Fig. 9.7, the qualitative result is the same for both components, although the ⊥ components are again blueshifted relative to the || components. The α/β intersections (E_c) are demarcated with circles for each SiNW. When -H is substituted with higher EN functional groups, E_c is seen to redshift from 3.12 eV [Fig. 9.7(a)]. In contrast, the <111>-*a*SiO_x SiNWs exhibit a different trend. E_c for the 622-atom SiNW occurs near 2.5 eV [Fig. 9.7(a)]; increased oxidation of the SiNW largely results in the vertical coordinate of E_c increasing with a slight blueshift. Note that α and β are representative of the comprehensive oxidized SiNW structure (*c*-Si and *a*-SiO_x phases). Giri *et al.* [190] mention the significance of explicitly accounting for each phase via multilayer model fitting in spectroscopic ellipsometry; however, since no attempt is made here to extract numerical parameters from this analysis, this demonstration of qualitative discernment among various surface passivations using Seraphin coefficients should still provide a meritable contribution.

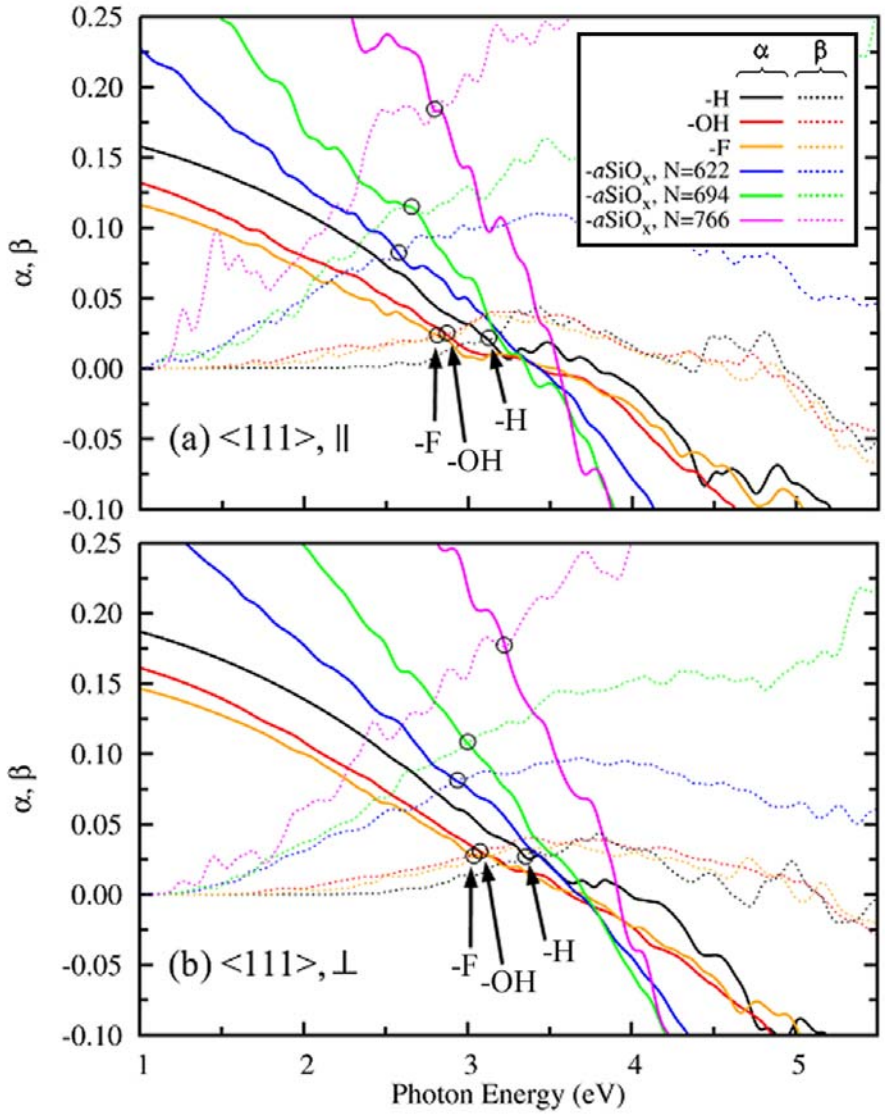

Figure 9.7: (Color available) Seraphin coefficients evaluated from (a) parallel and (b) perpendicular components of the dielectric function spectra computed from DFT-GGA calculations for all <111> SiNW passivations. Solid lines represent α values and dashed lines represent β values. The crossover energies (E_c) for each SiNW are identified by open circles for clarity.

Inspection of Fig. 9.8 illustrates three significant details about the behavior of Seraphin coefficients in SiO_x structures. First, amorphization of Si appears strictly as a redshift in E_c as emphasized by Sundari *et al*. [144]. Second, increasing oxide character

(x) in *a*-SiO_x has a substantial influence on both the vertical and horizontal coordinates of E_c. Third, the effect of *c*-SiO_2 amorphization is largely observed as change in vertical coordinate of E_c. In comparison, the oxide composition contribution appears to be a stronger influence on α and β than the induced structural disorder. In the context of oxidized SiNWs, the Seraphin coefficient behavior can be interpreted [Fig. 9.7] with the following contributions: (1) the blueshift and increasing E_c vertical coordinate with increasing oxidation is largely driven by changes in constituent Si oxidation states, (2) the energy coordinates for all three E_c values are somewhat redshifted relative to the -H case as a result of disorder, and (3) increasing Si disorder with increasing oxidation might be manifested as an increase in slope of the E_c trend.

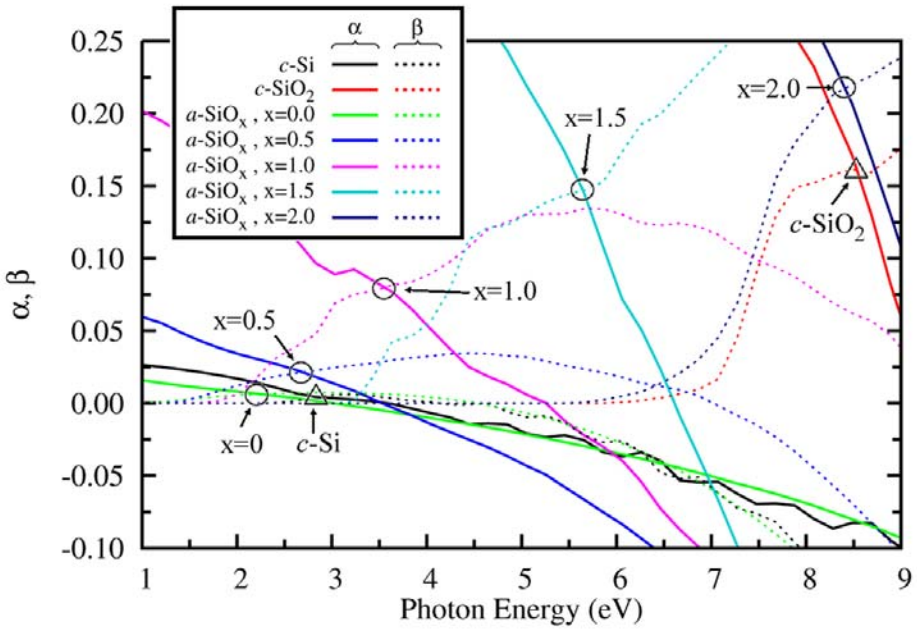

Figure 9.8: (Color available) Seraphin coefficients evaluated from DFT-GGA calculations for bulk *c*-Si, *c*-SiO_2 (α-quartz), and *a*-SiO_x (x = 0, 0.5, 1.0, 1.5, and 2.0) reference structures. All structures and their $\varepsilon_2(\omega)$ were previously described in Ref. 95. Solid lines represent α values and dashed lines represent β values. Crossover energies (E_c) are identified by open circles for *a*-SiO_x structures and open triangles for the limiting crystalline cases.

9.5 Oxidation Effect on Structure

The -*a*SiO_x SiNW cross-sections [see Figs. 9.1(g), 9.2(c), and 9.2(d)] illustrate a qualitative increase in disorder as oxide thickness increases. A brief summary is provided in Table 9.4 of the structural changes incurred from oxidation of the {110} lateral facets of <111>-oriented SiNWs. Observation of an increasing compressive character of the core Si-Si bonds is expected, but that trend is not readily apparent in Table 9.4. Instead, the 622-atom -*a*SiO_x wire has an average bond length (2.362 Å) nearly identical to the -H reference SiNW (2.363 Å). Further oxidation (N = 694 and 766 cases) actually increases the average Si-Si bond length. The average Si-Si-Si bond angle from the -H reference case (109.5° ± 0.9°) is decreased following oxidation and the introduced disorder is evidenced by an order of magnitude increase in the standard deviation. A trend for increased Si-O-Si bond angle approaching that of bulk *a*-SiO_2 (151° ± 11° Å) (Ref. 99) is observed as the oxidation thickness is increased on <111>-*a*SiO_x SiNWs. Note that one limitation of Monte Carlo methods in oxidation simulations is the inability to capture kinetically-limited processes during structural relaxation; in consequence, some resultant structures can be over-relaxed and thus distort some structural statistics.

As other reports indicate [177,181], the structural effects of oxidation on Si nanostructures is a complex, multivariate problem. Hofmeister *et al.* [181] synthesized oxidized SiNCs from silane pyrolysis and demonstrated that SiNCs with diameter < 3 nm (*c*-Si core) exhibit core tension, while SiNCs of larger diameter exhibit core compression relative to bulk Si. They attribute the observed diameter-dependent sign of core strain to an estimated negative interface stress contribution. The SiNW results presented here are qualitatively similar to the SiNC results of Hofmeister *et al.* Oxidized <111> SiNWs with core diameters < 3 nm have been presented here that exhibit core tension; on the

other hand, larger oxidized SiNWs (diameters ~ 10 nm, $N \sim 10^4$ atoms) have also been generated in unpublished work that indeed exhibit compressive strain in the Si core (magnitude dependent on oxide thickness) relative to the bulk Si-Si bond length (2.363 Å).

Table 9.4: <111> SiNW bond topology statistics for various surface passivations. Bond length statistics for -*a*SiO_x wires represent only Si^0 state atoms, while the -H reference excludes perimeter Si atoms with H neighbors. Bond angle values are comprehensive for each SiNW structure. All statistics are given as mean ± standard deviation.

Passivation	*N*	bond length	bond angle	
		Si-Si (Å)	Si-Si-Si (°)	Si-O-Si (°)
-*a* SiO_x	622	2.362 ± 0.050	109.0 ± 9.2	131.9 ± 17.7
-*a* SiO_x	694	2.390 ± 0.056	109.1 ± 9.2	133.7 ± 18.7
-*a* SiO_x	766	2.382 ± 0.057	109.0 ± 9.9	134.4 ± 18.1
-H	472	2.363 ± 0.003	109.5 ± 0.9	

9.6 Summary

In summary, a custom CRN-MMC simulation procedure was applied to generate amorphous oxide layers on four important orientations of SiNWs (<100>, <110>, <111>, and <112>) to study the effects of wire orientation, surface passivation, and degree of strain/disorder in the *c*-Si core on resultant optical spectra and electronic structure. To isolate the effects of surface passivation, the <111> SiNW orientation passivated with three different functional groups (-H, -F, and -OH) and three thicknesses of oxide sheath (622-, 694-, and 766-atom <111>-*a*SiO_x) was also studied.

For all SiNW orientations, the effect of oxidation on both $\varepsilon_2^{\parallel}(\omega)$ and $\varepsilon_2^{\perp}(\omega)$ dielectric function spectra shows consistent and appreciable reduction in the Si E_2 transition peak, redshift in fundamental absorption edge (E_0), and appearance of a high energy tail peaking near 10 eV representing the oxide contribution. The effect of quantum confinement imparts a blueshift on all $\varepsilon_2^{\perp}$ components relative to $\varepsilon_2^{\parallel}$. Band

structure calculations indicate an onset of amorphization resulting from oxidation as the disintegration of crystalline order is evidenced by smoothing of all bands in the gap vicinity that is attributed to k-point averaging along the SiNW axis. For the <112>-*a*SiO_x SiNW, k-point averaging changes the nature of the band gap from indirect to direct by moving the conduction band minimum to Γ.

The effect of surface passivation on the <111> SiNW in the $\varepsilon_2^{||}$ spectra by substitution of -H with either -F or -OH groups is similar: (1) redshift and reduction of $E_2^{||}$ peak, (2) redshift in both $E_1^{||}$ and $E_0^{||}$ transitions, and (3) increase in high energy tail intensity. Similar effects are seen for $\varepsilon_2^{\perp}$, but the $E_1^{\perp}$ peak is no longer evident with electronegative -F or -OH passivations. Influenced by previous employment of Seraphin coefficients (α and β) to optically characterize semiconductor structures, average α and β were computed from spectra for all six <111> SiNW surface passivations to evaluate the optical contributions of suboxide composition and disorder. The results obtained show a unique crossover energy (E_c) for each case and a clear distinction between functional group passivations and oxidation layers. In addition, increasing oxide thickness is identified using Seraphin coefficients as an increase mostly in the vertical coordinate of E_c, which was shown to correlate largely to increasing oxide character (x) in *a*-SiO_x. The present electronic and optical characterization of SiNWs passivated with amorphous oxide layers extends current understanding of these technologically interesting nanostructures, particularly in revealing how oxidation-induced disorder and composition modulate predicted properties.

Chapter 10

Conclusions

The economics and convenience of Si-based devices virtually ensure their sustained importance for the foreseeable future, so the ability to engineer better performance characteristics over intrinsic crystalline Si offers a challenging, but feasible, technological opportunity. The simulation results presented emphasize the significance of combining realistic structural descriptions with first-principles modeling techniques to attain meaningful property predictions that can potentially influence future experimental work.

Extensive results presented on the strain effects on the structure and stability of native defect clusters showcase a surprisingly strong relationship between cluster orientation and stability that is driven by symmetry considerations. Not only does strain influence cluster orientation in a strain field, but strain must also be considered in determination of the minimum energy configuration under arbitrary strain conditions. Fourfold-coordinated (FC) cluster configurations are particularly important; not only do FC configurations prevail for all but the smallest clusters, but they also appear exceedingly hard to detect since they do not usually introduce deep-level defect states in the band gap.

The property predictions presented for amorphous materials emphasize a strength of modeling techniques over experiment in providing absolute confidence in material identity, which is surprisingly difficult to achieve from physical measurements. At the same time, first-principles techniques push the limits of modern computational hardware

in terms of model size, *N*, which is essential in capturing the random nature of an amorphous network.

The work presented for structural disorder emphasizes a considerable enhancement of optical absorption driven at the subnanometer scale. While these results show the effects of strain and structural disorder are stronger than that of density, the influence of density is suspected to become an important contribution at larger length scales than is currently feasible with *ab initio* techniques. In addition, a strong concentration effect for optical absorption justifies experimental reports of electrical and optical transparency for small native defect clusters. Both band structure and optical spectra provide insight into the significant influences of both oxidation-induced disorder and suboxide contributions generated by growth of amorphous oxide layers on Si.

The work presented can certainly be extended as both computational resources and methods become increasingly capable of managing the demands of increasingly realistic material models. The ability to model ever-larger systems is pivotal to improved atomistic modeling of multiphase materials, amorphous networks, and systems containing extended defects. It is also desirable to improve the quantitative property prediction capacity of conventional DFT calculations, especially the band gap underestimation which obscures quantitative electrical and optical analyses. Nevertheless, this work provides an important contribution toward advancement of first-principles property predictions in modified Si-based materials.

References

[1] B. G. Streetman, *Solid State Electronic Devices* (Prentice Hall; Upper Saddle River, NJ; 1995).

[2] G. K. Teal, IEEE Trans. Electron Devices **23**, 621 (1976).

[3] E. H. Poindexter, P. Caplan, B. Deal, and R. Razouk, *J. Appl. Phys.* **52**, 879 (1981).

[4] H. Fukuda, M. Yasuda, T. Iwabuchi, S. Kaneko, T. Ueno, I. Ohdomari, *J. Appl. Phys.* **72**, 1906 (1992).

[5] R. G. Parr and W. Yang, *Density-Functional Theory of Atoms and Molecules* (Oxford Univ. Press; New York; 1989).

[6] P. Hohenberg and W. Kohn, Phys. Rev. **136**, B864 (1964).

[7] K. F. Brennan, *The Physics of Semiconductors* (Cambridge Univ. Press; New York; 1999).

[8] A. R. Leach, *Molecular Modelling: Principles and Applications* (Pearson Education Limited; Dorchester, United Kingdom; 2001).

[9] W. Kohn and L. J. Sham, Phys. Rev. **140**, A1133 (1965).

[10] G. Kresse and J. Furthmüller, *VASP the Guide* (Vienna University of Technology, Vienna, 2001).

[11] J. P. Perdew and Y. Wang, Phys. Rev. B **45**, 13244 (1992).

[12] J. P. Perdew, K. Burke, and M. Ernzerhof, Phys. Rev. Lett. 77, 3865 (1996).

[13] D. Vanderbilt, Phys. Rev. B **41**, 7892 (1990).

[14] P. E. Blöchl, Phys. Rev. B **50**, 17953 (1994).

[15] S. Lee, R. J. Bondi, and G. S. Hwang, "Ab Initio Parameterized Valence Force Field for the Structure and Energetics of Amorphous SiO_x ($0 \leq x \leq 2$) Materials," submitted (2010).

[16] Y. Tu, J. Tersoff, G. Grinstein, and D. Vanderbilt, Phys. Rev. Lett. **81**, 4899 (1998).

[17] D. Yu, S. Lee, and G. S. Hwang, J. Appl. Phys. **102,** 084309 (2007).

[18] S. Lee and G. S. Hwang, Phys. Rev. B **77**, 085210 (2008).

[19] S. Lee and G. S. Hwang, Phys. Rev. B **78**, 045204 (2008).

[20] S. Lee and G. S. Hwang, Phys. Rev. B **78**, 125310 (2008).

[21] S. Lee, R. J. Bondi, and G. S. Hwang, Phys. Rev. B **80**, 245209 (2009).

[22] S. Lee, R. J. Bondi, and G. S. Hwang, Mol. Simul. **35**, 867 (2009).

[23] S. Lee, R. J. Bondi, and G. S. Hwang, "Atomistic Structural Description of the Si(001)/*a*-SiO_2 Interface: The Influence of Different Keating-like Potential Parameters," submitted (2010).

[24] F. Wooten, K. Winer, and D. Weaire, Phys. Rev. Lett. **54**, 1392 (1985).

[25] P. N. Keating, Phys. Rev. **145**, 637 (1966).

[26] Y. Zhang, J.-M Zhang, and V. Ji, Physica B **389**, 372 (2007).

[27] T. Courtney, *Mechanical Behavior of Materials* (McGraw-Hill; Boston; 2000).

[28] R. Zhu, E. Pan, P. W. Chung, X. Cai, K. M. Liew, and A. Buldum, Semicond. Sci. Technol. **21**, 906 (2006).

[29] P. Bhattacharya, *Semiconductor Optoelectronic Devices* (Prentice Hall; Upper Saddle River, NJ; 1997).

[30] J. Singh, Physics of *Semiconductors and Their Heterostructures* (McGraw-Hill, New York, 1993).

[31] L. Lin, T. Kirichenko, B. R. Sahu, G. S. Hwang, and S. K. Banerjee, Phys. Rev. B **72**, 205206 (2005).

[32] C. G. Van de Walle and R. M. Martin, Phys. Rev. B **34**, 5621 (1986).

[33] M. E. Levinshtein, S. L. Rumyantsev, and M. S. Shur, *Handbook Series on Semiconductor Parameters* (World Scientific, London, 1996) Vol. 1, p. 29.

[34] N. Arai, S. Takeda, and M. Kohyama, Phys. Rev. Lett. **78**, 4265 (1997).

[35] B. J. Coomer, J. P. Goss, R. Jones, S. Oberg, and P. R. Briddon, J. Phys.: Condens. Matter 13, L1-L7 (2001).

[36] W. A. Brantley, J. Appl. Phys. **44**, 534 (1973).

[37] J. J. Wortman and R. A. Evans, J. Appl. Phys. **36**, 153 (1965).

[38] T. Engel and P. Reid, *Physical Chemistry* (Pearson Education, Inc.; New York; 2006).

[39] M. J. Mehl, Phys. Rev. B **47**, 2493(1993).

[40] F. Birch, J. Geophys. Res. **83**, 1257 (1978).

[41] B. Adolph, J. Furthmüller, and F. Bechstedt, Phys. Rev. B **63**, 125108 (2001).

[42] I. J. Wu and G. Y. Guo, Phys. Rev. B **76**, 035343 (2007).

[43] K. Sánchez, I. Aguilera, P. Palacios, and P. Wahnón, Phys. Rev. B **79**, 165203 (2009).

[44] L. E. Ramos, E. Degoli, G. Cantele, S. Ossicini, D. Ninno, J. Furthmüller, and F. Bechstedt, Phys. Rev. B **78**, 235310 (2008).

[45] K. Seino, F. Bechstedt, and P. Kroll, Nanotech. **20**, 135702 (2009).

[46] J. Furthmüller, http://www.freeware.vasp.de/VASP/optics, 2010.

[47] M. Gajdoš, K. Hummer, G. Kresse, J. Furthmüller, and F. Bechstedt, Phys. Rev. B **73**, 045112 (2006).

[48] G. Y. Guo, K. C. Chu, D.-S. Wang, and C.-G. Duan, Phys. Rev. B **69**, 205416 (2004).

[49] Y.-N. Xu and W. Y. Ching, Phys. Rev. B **44**, 11048 (1991).

[50] M. Marsman, J. Paier, A. Stroppa, and G. Kresse, J. Phys.: Condens. Matter **20**, 064201 (2008).

[51] J. Furthmüller, G. Cappellini, H.-Ch. Weissker, and F. Bechstedt, Phys. Rev. B **66**, 045110 (2002).

[52] S. E. Thompson, Guangyu Sun, Youn Sung Choi, and Toshikazu Nishida, IEEE Trans. Electron Devices **53**, 1010 (2006).

[53] J. Kim, F. Kirchoff, J. W. Wilkins, and F. S. Khan, Phys. Rev. Lett. **84**, 503 (2000).

[54] P. K. Giri, Semicond. Sci. Technol. **20**, 638 (2005).

[55] J. Kim, J. W. Wilkins, F. S. Khan, and A. Canning, Phys. Rev. B **55**, 16186 (1997).

[56] M. Kohyama and S. Takeda, Phys. Rev. B **46**, 12305 (1992).

[57] C. J. Ortiz, P. Pichler, T. Fuhner, F. Cristiano, B. Colombeau, N. E. B. Cowern, and A. Claverie, J. Appl. Phys. **96**, 4866 (2004).

[58] N. E. B. Cowern, G. Mannino, P. A. Stolk, F. Roozeboom, H. G. A. Huizing, J. G. M. van Berkum, F. Cristiano, A. Claverie, and M. Jaraiz, Phys. Rev. Lett. **82**, 4460 (1999).

[59] K. Derbyshire, Solid State Technology, **50**, 38 (2007).

[60] K.-J. Chui, K.-W. Ang, N. Balasubramanian, M.-F. Li, G. S. Samudra, and Y.-C. Yeo, IEEE Trans. Electron Devices **54**, 249 (2007).

[61] D. J. Paul, Semicond. Sci. Technol. **19**, R75 (2004).

[62] R. Harper, Materials Science and Engineering B **134**, 154 (2006).

[63] A. Thean and J. P. Leburton, Appl. Phys. Lett. **79**, 1030, (2001).

[64] R. J. Bondi, S. Lee, and G. S. Hwang, Phys. Rev. B **79**, 104106 (2009). "Copyright (2009) by the American Physical Society."

[65] R. J. Bondi, S. Lee, and G. S. Hwang, Phys. Rev. B **80**, 125202 (2009). "Copyright (2009) by the American Physical Society."

[66] G. Kresse and J. Hafner, Phys. Rev. B **47**, 558 (1993); **49**, 14251 (1994); G. Kresse and J. Furthmüller, Computational Materials Science 6, **15** (1996); Phys. Rev. B **54**, 11169 (1996).

[67] G. M. Lopez and V. Fiorentini, Phys. Rev. B **69**, 155206 (2004).

[68] D. A. Richie, J. Kim, S. A. Barr, K. R. A. Hazzard, R. Hennig, and J. W. Wilkins, Phys. Rev. Lett. **92**, 045501 (2004).

[69] W.-K. Leung, R. J. Needs, G. Rajagopal, S. Itoh, and S. Ihara, Phys. Rev. Lett. **83**, 2351 (1999).

[70] L. Colombo, Physica B **273-274**, 458 (1999).

[71] M. Gharaibeh, S. K. Estreicher, P. A. Fedders, Physica B **273-274**, 532 (1999).

[72] R. J. Bondi, S. Lee, and G. S. Hwang, Appl. Phys. Lett. **94**, 264101 (2009). "Copyright (2009) by the American Institute of Physics."

[73] D. A. Abdulmalik and P. G. Coleman, Phys. Rev. Lett. **100**, 095503 (2008).

[74] A. La Magna, S. Coffa, and L. Colombo, Phys. Rev. Lett. **82**, 1720 (1999).

[75] E. Dornberger, D. Temmler, and W. Von Ammon, J. Electrochem. Soc. **149**, G226 (2002).

[76] D. V. Makhov and L. J. Lewis, Phys. Rev. Lett. **92**, 255504 (2004).

[77] S. K. Estreicher, Phys. Stat. Sol. B **217**, 513 (2000).

[78] J. L. Hastings, S. K. Estreicher, and P. A. Fedders, Phys. Rev. B **56**, 10215 (1997).

[79] T. E. M. Staab, A. Sieck, M. Haugk, M. J. Puska, Th. Frauenheim, and H. S. Leipner, Phys. Rev. B **65**, 115210 (2002).

[80] J. S. Williams, M. J. Conway, B. C. Williams, and J. Wong-Leung, Appl. Phys. Lett. **78**, 2867 (2001).

[81] G. S. Hwang and W. A. Goddard III, Phys. Rev. B **65**, 233205 (2002).

[82] D. J. Chadi and K. J. Chang, Phys. Rev. B **38**, 1523 (1988).

[83] M. G. Ganchenkova, S. Nicolaysen, V. A. Borodin, E. Halvorsen, and R. M. Nieminen, Mat. Sci. and Eng. B **134**, 244 (2006).

[84] A. Bongiorno and L. Colombo, Phys. Rev. B **57**, 8767 (1998).

[85] A. Zywietz, J. Furthmüller, and F. Bechstedt, Phys. Status Solidi B **210**, 13 (1998).

[86] R. J. Bondi, S. Lee, and G. S. Hwang, Phys. Rev. B **81**, 245206 (2010). "Copyright (2010) by the American Physical Society."

[87] P. Y. Yu and M. Cardona, *Fundamentals of Semiconductors* (Springer-Verlag; New York; 2001).

[88] R. Kuschnereit, H. Fath, A. A. Kolomenskii, and M. Szabadi, and P. Hess, Appl. Phys. A **61**, 269 (1995).

[89] D. E. Carlson and C. R. Wronski, Appl. Phys. Lett. **28**, 671 (1976).

[90] D. L. Staebler and C. R. Wronski, Appl. Phys. Lett. **31**, 292 (1977).

[91] C. R. Wronski, B. von Roedern, and A. Kolodziej, Vacuum **82**, 1145 (2008).

[92] V. Beyer, J. von Borany, and M. Klimenkov, J. Appl. Phys. **101**, 094507 (2007).

[93] G. Gawlik and J. Jagielski, Nucl. Instr. and Meth. B **266**, 1307 (2008).

[94] G. A. Kachurin, S. G. Cherkova, D. V. Marin, R. A. Yankov, and M. Deustchmann, Nanotech. **19**, 355305 (2008).

[95] R. J. Bondi, S. Lee, and G. S. Hwang, Phys. Rev. B **81**, 195207 (2010). "Copyright (2010) by the American Physical Society."

[96] K. Tanaka, E. Maruyama, T. Shimada, and H. Okamoto, *Amorphous Silicon* (John Wiley & Sons Ltd.; Chichester, England; 1999).

[97] I. N. Levine, *Physical Chemistry* (McGraw-Hill, Inc.; St. Louis, Missouri; 1995).

[98] J. Sarnthein, A. Pasquarello, and R. Car, Phys. Rev. B **52**, 12690 (1995).

[99] F. Mauri, A. Pasquarello, B. G. Pfrommer, Y.-G. Yoon, and S. G. Louie, Phys. Rev. B **62**, R4786 (2000).

[100] M. Szabadi, P. Hess, A. J. Kellock, H. Coufal, and J. E. E. Baglin, Phys. Rev. B **58**, 8941 (1998).

[101] A. Brunet-Bruneau, D. Souche, S. Fisson, V. Nguyen Van, G. Vuye, F. Abeles, and J. Rivory, J. Vac. Sci. Technol. A **16**, 2281 (1998).

[102] K. Jarolimek, R. A. de Groot, G. A de Wijs, and M. Zeman, Phys. Rev. B **79**, 155206 (2009).

[103] W. F. Hosford, *Mechanical Behavior of Materials* (Cambridge Univ. Press; New York; 2005).

[104] X. Jiang, B. Goranchev, K. Schmidt, P. Grünberg, and K. Reichelt, J. Appl. Phys. **67**, 6772 (1990).

[105] Bulk modulus was computed from tabulated experimental values of Y and ν from Ref. 100 using $B = Y/(3(1-2\nu))$.

[106] K. Tanaka, Solid State Comm. **60**, 295 (1986).

[107] V. Kulikovsky, V. Vorlicek, P. Bohac, M. Stranyanek, R. Ctvrtlik, and A. Kurdyumov, Thin. Sol. Films **516**, 5368 (2008).

[108] T. Rouxel, J. Am. Ceram. Soc. **90**, 3019 (2007).

[109] *Handbook of Nanotechnology*, edited by B. Bhushan (Spring-Verlag; New York; 2004).

[110] H. Ni, X. Li, and H. Gao, Appl. Phys. Lett. **88**, 043108 (2006).

[111] X. Li, B. Bhushan, K. Takashima, C.-W. Baek, and Y.-K. Kim, Ultramicroscopy **97**, 481 (2003).

[112] V. I. Ivashchenko, P. E. A. Turchi, and V. I. Shevchenko, Phys. Rev. B **75**, 085209 (2007).

[113] P. Kroll, J. Non-Cryst. Sol. **345&346**, 720 (2004).

[114] R. W. Hoffman, Jr., T. E. Mitchell, and R. W. Hoffman, Thin Solid Films **154**, 149 (1987).

[115] *Properties of Amorphous Silicon and its Alloys*, edited by T. Searle (INSPEC; London; 1998).

[116] R. B. Sosman, *The Properties of Silica* (Chemical Catalog Co.; New York; 1927).

[117] T. Otobe, K. Yabana, and J.-I. Iwata, J. Phys.: Condens. Matter **21**, 064224 (2009).

[118] G. F. Feng, M. Katiyar, J. R. Abelson, and N. Maley, Phys. Rev. B **45**, 9103 (1992).

[119] D. A. G. Bruggeman, Ann. Phys. **416**, 636 (1935).

[120] A. Ranzter, H. Arwin, J. Birch, B. Hjörvarsson, J. W. P. Bakker, and K. Järrendahl, Thin Sol. Films **394**, 256 (2001).

[121] K. Hübner, J. Non-Cryst. Sol. **35&36**, 1011 (1980).

[122] A. Hjortsberg and C. G. Granqvist, Appl. Optics **19**, 1694 (1980).

[123] *Handbook of Optical Constants of Solids*, edited by E. D. Palik, (Academic Press; San Diego, CA; 1997).

[124] T. Koslowski, W. Kob, and K. Vollmayr, Phys. Rev. B **56**, 9469 (1997).

[125] *Nanostructured Materials for Solar Energy Conversion*, edited by T. Soga (Elsevier; San Diego, CA; 2006).

[126] A. G. Aberle, Thin Solid Films **517**, 4706 (2009).

[127] S. P. Philipps, G. Peharz, R. Hoheisel, T. Hornung, N. M. Al-Abbadi, F. Dimroth, and A. W. Bett, Solar Energy Mat. and Solar Cells **94**, 869 (2010).

[128] L. K. Wagner and J .C. Grossman, Phys. Rev. Lett. **101**, 265501 (2008).

[129] T. Stelzner, M. Pietsch, G. Andrä, F. Falk, E. Ose, and S. Christiansen, Nanotech. **19**, 295203 (2008).

[130] A. Mattoni, L. Ferraro, and L. Colombo, Phys. Rev. B **79**, 245302 (2009).

[131] S. Knief and W. von Niessen, Phys. Rev. B **59**, 12940 (1999).

[132] H. J. Stein, F. L. Vook, and J. A. Borders, Appl. Phys. Lett. **14**, 328 (1969).

[133] *Porous Silicon*, edited by Z. C. Feng and R. Tsu (World Scientific Publishing Co. Pte. Ltd.; River Edge, NJ; 1994).

[134] D. Kovalev, G. Polisski, M. Ben-Chorin, J. Diener, and F. Koch, J. Appl. Phys. **80**, 5978 (1996).

[135] S. S. Iyer and Y.-H. Xie, Science **260**, 40 (1993).

[136] Ch. Populaire, B. Remaki, V. Lysenko, D. Barbier, H. Artmann, and T. Pannek, Appl. Phys. Lett. **83**, 1370 (2003).

[137] Y. Pan, F. Inam, M. Zhang, and D. A. Drabold, Phys. Rev. Lett. **100**, 206403 (2008).

[138] G. Davies, S. Hayama, L. Murin, R. Krause-Rehberg, V. Bondarenko, A. Sengupta, C. Davia, A. Karpenko, Phys. Rev. B **73**, 165202 (2006).

[139] R. J. Bondi, S. Lee, and G. S. Hwang, Phys. Rev. B **82**, 115214 (2010). "Copyright (2010) by the American Physical Society."

[140]. K. Laaziri, S. Kycia, S. Roorda, M. Chicoine, J. L. Robertson, J. Wang, and S. C. Moss, Phys. Rev. Lett. **82**, 3460 (1999).

[141] K. Laaziri, S. Kycia, S. Roorda, M. Chicoine, J. L. Robertson, J. Wang, and S. C. Moss, Phys. Rev. B **60**, 13520 (1999).

[142] Comparison of $\alpha(\omega)$ spectra for *c*-Si (480 atoms) in Fig. 7.2 and *c*-Si (980 atoms) in Fig. 7.3 reveals a notable difference in the feet where incipient absorption occurs between approximately 2.0 and 2.5 eV. It was found impractical to exactly match optical references across variable supercell sizes using this method, so an effort was made to present the results, whenever possible, in the context of a single basis supercell size.

[143] The algorithm used to identify bond network connectivity searched each Si atom for neighbors within a fixed range, 2.1 Å $\leq r_{ij} <$ 3.3 Å, where r_{ij} is the separation distance between two Si atoms. This range effectively sets a minimum and maximum for all bond lengths, so structure classification as fourfold-coordinated is somewhat subjective.

[144] S. T. Sundari and G. Raghavan, Appl. Phys. Lett. **86**, 241906 (2005).

[145] J. C. Idrobo, A. Halabica, R. H. Magruder III, R. F. Haglund, Jr., S. J. Pennycook, and S. T. Pantelides, Phys. Rev. B **79**, 125322 (2009).

[146] The initial goal was to construct porous Si (*p*-Si) structures with the method detailed in Section 7.3 because of their well-known, but poorly understood, ability to both absorb [133] and emit light [133,135], but the distinctly different morphologies of the resulting structures led to their identification as variable-density *a*-Si samples. A large reduction in density can certainly be interpreted as an increase in porosity, but the morphologies of reported [133,135,136] *p*-Si structures are typically categorized as either (1) irregular arrays of quantum wells (pores) or wires on a *c*-Si surface or (2) sponge-like matrices of embedded Si crystallites in an interconnected network with voids, *a*-Si, and/or amorphous silicon oxide pockets comprising the remaining volume.

[147] M. Banerjee, S. K. Datta, and H. Saha, Nanotechnology **16**, 1542 (2005).

[148] P. J. Foster, J. K. Doylend, P. Mascher, A. P. Knights, and P. G. Coleman, Proc. of SPIE **5577**, 683 (2004).

[149] H. A. Weakliem and D. Redfield, J. Appl. Phys. 50, 1491 (1979).

[150] © The Electrochemical Society, Inc. All rights reserved. Except as provided under U.S. copyright law, this work may not be reproduced, resold, distributed, or modified without the express permission of The Electrochemical Society (ECS). The archival version of this work is pending publication in R. J. Bondi, S. Lee, and G. S. Hwang, "First-Principles Prediction of Optical Absorption Enhancement for Si Native Defect Clusters under Biaxial Strain," Electrochem. Solid-State Lett., accepted (2010).

[151] P. Palacios, I. Aquilera, K. Sánchez, J. C. Conesa, and P. Wahnón, Phys. Rev. Lett. 101, 046403 (2008).

[152] R. Q. Zhang, Y. Lifshitz, D. D. D. Ma, Y. L. Zhao, Th. Frauenheim, S. T. Lee, and S. Y. Tong, J. Chem. Phys. **123**, 144703 (2005).

[153] B. Aradi, L. E. Ramos, P. Deák, Th. Köhler, F. Bechstedt, R. Q. Zhang, and Th. Frauenheim, Phys. Rev. B **76**, 035305 (2007).

[154] P. W. Leu, A. Svizhenko, and K. Cho, Phys. Rev. B **77**, 235305 (2008).

[155] K.-H. Hong, J. Kim, S.-H. Lee, and J. K. Shin, Nano Lett. **8**, 1335 (2008).

[156] J. Li and A. J. Freeman, Phys. Rev. B **74**, 075333 (2006).

[157] H. Scheel, S. Reich, and C. Thomsen, Phys. Status Solidi B **242**, 2474 (2005).

[158] A. Hmiel and Y. Xue, Phys. Rev. B **80**, 241410(R) (2009).

[159] S. Bhattacharya, D. Banerjee, K. W. Adu, S. Samui, and So. Bhattacharyya, Appl. Phys. Lett. **85**, 2008 (2004).

[160] Y. F. Zhang, Y. H. Tang, N. Wang, C. S. Lee, I. Bello, and S. T. Lee, J. Crystal Growth **197**, 136 (1999).

[161] D. Yao, G. Zhang, and B. Li, Nano Lett. **8**, 4557 (2008).

[162] A. K. Singh, V. Kumar, R. Note, and Y. Kawazoe, Nano Lett. **6**, 920 (2006).

[163] C.-Y. Moon, W.-J. Lee, and K. J. Chang, Nano Lett. **8**, 3086 (2008).

[164] T. Maegawa, T. Yamauchi, T. Hara, H. Tsuchiya, and M. Ogawa, IEEE Trans. Electron Devices **56**, 553 (2009).

[165] Y. F. Zhang, L. S. Liao, W. H. Chan, S. T. Lee, R. Sammynaiken, and T. K. Sham, Phys. Rev. B **61**, 8298 (2000).

[166] D. Dai, Y. Shi, and S. He, Appl. Optics **46**, 1126 (2007).

[167] E. C. Garnett and P. Yang, J. Am. Chem. Soc. **130**, 9224 (2008).

[168] K. Kang, H.-S. Lee, D.-W. Han, G.-S. Kim, D. Lee, G. Lee, Y.-M. Kang, and M.-H. Jo, Appl. Phys. Lett. **96**, 053110 (2010).

[169] S. Chen, J. G. Bomer, W. G. van der Wiel, E. T. Carlen, and A. van den Berg, ACS Nano **3**, 3485 (2009).

[170] L. J. Chen, J. Mat. Chem. **17**, 4639 (2007).

[171] M. D. Kelzenberg, D. B. Turner-Evans, B. M. Kayes, M. A. Filler, M .C. Putnam, N. S. Lewis, and H. A. Atwater, Nano Lett. **8**, 710 (2008).

[172] D. P. Yu, Z. G. Bai, Y. Ding, Q. L. Hang, H. Z. Zhang, J. J. Wang, Y. H. Zou, W. Qian, G. C. Xiong, H. T. Zhou, and S. Q. Feng, Appl. Phys. Lett. **72**, 3458 (1998).

[173] D. D. D. Ma, C. S. Lee, F. C. K. Au, S. Y. Tong, and S. T. Lee, Science **299**, 1874 (2003).

[174] N. Wang, Y. H. Tang, Y. F. Zhang, C. S. Lee, and S. T. Lee, Phys. Rev. B **58**, R16024 (1998).

[175] B. K. Teo, C. P. Li, X. H. Sun, N. B. Wong, and S. T. Lee, Inorg. Chem. **42**, 6723 (2003).

[176] Y. Tu and J. Tersoff, Phys. Rev. Lett. **84**, 4393 (2000).

[177] L. E. Ramos, J. Furthmüller, and F. Bechstedt, Phys. Rev. B **70**, 033311 (2004).

[178] L. E. Ramos, J. Furthmüller, and F. Bechstedt, Appl. Phys. Lett. **87**, 143113 (2005).

[179] G. Fagas and J. C. Greer, Nano Lett. **9**, 1856 (2009).

[180] H. I. Liu, D. K. Biegelsen, F. A. Ponce, N. M. Johnson, R. F. W. Pease, Appl. Phys. Lett. **64**, 1383 (1994).

[181] H. Hofmeister, F. Huisken, and B. Kohn, Eur. Phys. J. D **9**, 137 (1999).

[182] R. J. Bondi, S. Lee, and G. S. Hwang, "First-Principles Study of the Structural, Electronic, and Optical Properties of Oxide-Sheathed Silicon Nanowires," submitted (2010).

[183] A. M. Morales and C. M. Lieber, Science **279**, 208 (1998).

[184] F. Bruneval, S. Botti, and L. Reining, Phys. Rev. Lett. **94**, 219701 (2005).

[185] P. Carrier, L. J. Lewis, and M. W. C. Dharma-wardana, Phys. Rev. B **65**, 165339 (2002).

[186] F. H. Pollak and H. Shen, J. Elec. Materials **19**, 399 (1990).

[187] B. O. Seraphin and N. Bottka, Phys. Rev. **145**, 628 (1966).

[188] M. Cardona, *Modulation Spectroscopy* (Academic; New York; 1969).

[189] S. Zh. Karazhanov, P. Kroll, A. Holt, A. Bentzen, and A. Ulyashin, J. Appl. Phys. **106**, 053717 (2009).

[190] P. K. Giri, S. Tripurasundari, G. Raghavan, B. K. Panigrahi, P. Magudapathy, K. G. M. Nair, and A. K. Tyagi, J. Appl. Phys. **90**, 659 (2001).